MIXED IONIC AND ELECTRONIC CONDUCTING ELECTRODE

STUDIES FOR AN

ALKALI METAL THERMAL TO ELECTRIC CONVERTER

A Dissertation

by

YUYAN GUO

Submitted to the Office of Graduate Studies of
Texas A&M University
in partial fulfillment of the requirements for the degree of

DOCTOR OF PHILOSOPHY

December 2006

Major Subject: Chemistry

MIXED IONIC AND ELECTRONIC CONDUCTING ELECTRODE

STUDIES FOR AN

ALKALI METAL THERMAL TO ELECTRIC CONVERTER

A Dissertation

by

YUYAN GUO

Submitted to the Office of Graduate Studies of
Texas A&M University
in partial fulfillment of the requirements for the degree of

DOCTOR OF PHILOSOPHY

Approved by:

Co-Chairs of Committee,	Timothy R. Hughbanks
	Michael Schuller
Committee Members,	Manuel P. Soriaga
	David W. Goodman
Head of Department,	Emile A. Schweikert

December 2006

Major Subject: Chemistry

ABSTRACT

Mixed Ionic and Electronic Conducting Electrode Studies for an Alkali Metal Thermal

to Electric Converter. (December 2006)

Yuyan Guo, B.S., University of Science & Technology, Beijing;

M.S., University of Science & Technology, Beijing

Co-Chairs of Advisory Committee: Dr. Timothy R. Hughbanks
Dr. Michael Schuller

This research focuses on preparation, kinetics, and performance studies of mixed ionic and electronic conducting electrodes (MIEE) applied in an alkali metal thermal to electric converter (AMTEC). Two types of MIEE, metal/sodium titanate and metal/β''-alumina were investigated, using Ni, Cu, Co and W as the metal components. Pure metal electrodes (PME) were also studied, including Ta, Ni, Nb, Ir, W and MoRe electrodes.

The stability of MIEE/β''-alumina solid electrolyte (BASE) interface was studied in terms of the chemical potential of Na-Al-Ti-O system at 1100K (typical AMTEC operating temperature). Ni metal was compatible with sodium titanate and BASE and displayed the best initial performance among all tested PMEs. Ni/sodium titanate electrodes with 4/1 mass ratios of metal/ceramic performed best among all tested electrodes. Scanning Electron Microscope (SEM) observations showed that grain agglomeration, which is the main mechanism for electrode degradation, occurred in all tested electrodes. Ceramic components were able to effectively limit the growth of metal grains and resulted in a long lifetime for MIEEs. Ni particles in the MIEE formed

a network microstructure that was close to the theoretical morphology of the ideal electrode. A model based on percolation theory was constructed to interpret and predict the performance of MIEEs.

The electrode kinetics was studied and a theoretical expression for the interface impedance was derived for both PME and MIEE, using electrochemical impedance spectroscopy (EIS). The conductivity of the $Na_2Ti_3O_7$ and $Na_2Ti_6O_{13}$ mixture was measured. The average activation energy for the bulk conductivity was 0.87ev. Finally, theoretical analysis clarified that the transfer coefficient α value change would cause at most a few percent change in the electrode performance parameter B.

DEDICATION

To my parents

Jianzhong Guo and Shuge Wang

And my sister

Yushu Guo

ACKNOWLEDGMENTS

I would like to thank my research advisor Dr. Michael Schuller for providing me the opportunities and environment for performing good research and in particular for his guidance and support throughout the period of my studies.

I would also like to thank Dr. Hughbanks for his advice on research attitude and scientific integrity, as well as the time and effort he devoted to me. I greatly appreciate Dr. Guillemette for his patience and guidance on the electron microprobe usage.

I would like to acknowledge my colleagues and friends, Scott Coughlin, Tejas Shah, Chunsheng Wang, Xiaole Chen, Jack Baricuatro, Li Zhu, Jingyi Shen and Liang Zhao, for their help, kindness and encouragement.

Finally, I would like to thank my parents and sister, for their unwavering love, support and encouragement throughout my life. It is to them that I owe many of my accomplishments.

TABLE OF CONTENTS

LIST OF FIGURES

FIGURE   Page

LIST OF TABLES

CHAPTER I

INTRODUCTION

1.1 Motivation

As researchers continue to push technological limits to probe the far reaches of our solar system, significant challenges emerge. One such challenge is associated with the way in which these spacecraft are powered. The most common source of power for these probes, which derived from solar illumination, becomes an inefficient energy source as the distance from the sun increases. Radioisotope thermoelectric generators (RTG) that have been put to use in deep space exploration vehicles such Pioneer (1972), Voyager (1977) and Galileo (1977), are considered high in mass and low in conversion efficiency.[1,2] Because of these shortcomings, NASA's Space Nuclear Initiative (SNI) has been making efforts to develop more advanced power systems technologies for future missions that may involve travel to the farthest planets of our solar system and beyond. These technologies that are pursued in space power point to higher reliability, higher density, higher efficiency, lower cost and lower volume. The Alkali Metal Thermal to Electric Converter (AMTEC) is one of these technologies and has the potential to meet all these goals and objectives.[3,4]

AMTEC was first developed at the Ford Scientific Laboratory in Dearborn, Michigan in 1968 and was further supported by NASA work at the Jet Propulsion Laboratory (JPL) in the early 1980s. Since that time, several companies and laboratories throughout

This dissertation follows the style and format of *Journal of the Electrochemical Society*.

the world have studied and further developed AMTEC's power generation process.[5-8] Currently, conversion efficiencies have been demonstrated as high as 22% in the laboratory with open circuit voltages in single electrochemical cells up to 1.6V and current densities up to 2.0A/cm^2. With a few improvements, AMTEC is expected to yield power efficiencies as high as 30 percent and a power density of approximately 80 watts per kilogram in the near future, which would significantly reduce overall system mass. What makes AMTEC even more appealing is that it is a static energy conversion device and fuel source insensitive in that it can utilize heat from nearly any source, including fossil fuel, the sun, radioisotopes, or a nuclear reactor.[4,9-11] With all these advantages combined, AMTEC appears to be extremely promising for use as an electrical power system on further deep space mission and terrestrial application.

1.2 Alkali Metal Thermal to Electric Converter

AMTEC, originally designed to be a space power generator to fulfill the requirements of diverse space missions, is a high-temperature regenerative concentration cell that employs an alkali metal working fluid (such as sodium or potassium) to directly convert heat to electricity. It can provide efficiencies close to the theoretical Carnot efficiency and is capable of high power density and low mass.[9-12]

1.2.1 AMTEC Operating Principles

AMTEC operation is based on the principle of sodium concentration cells, in which the driving force is the sodium pressure difference between the anode and cathode. The device uses an alkali metal conducting ceramic, polycrystalline β″-alumina, as the

electrolyte. With the formula of $Na_2(Mg, Li)O \bullet 5Al_2O_3$, β''-alumina has mobile Na^+ ions in its structure, which results in it being an excellent sodium ion conductor, but a poor electronic conductor.(further details of β''-alumina can be found in next section.) The principles of AMTEC operation are shown in Figure 1.1.
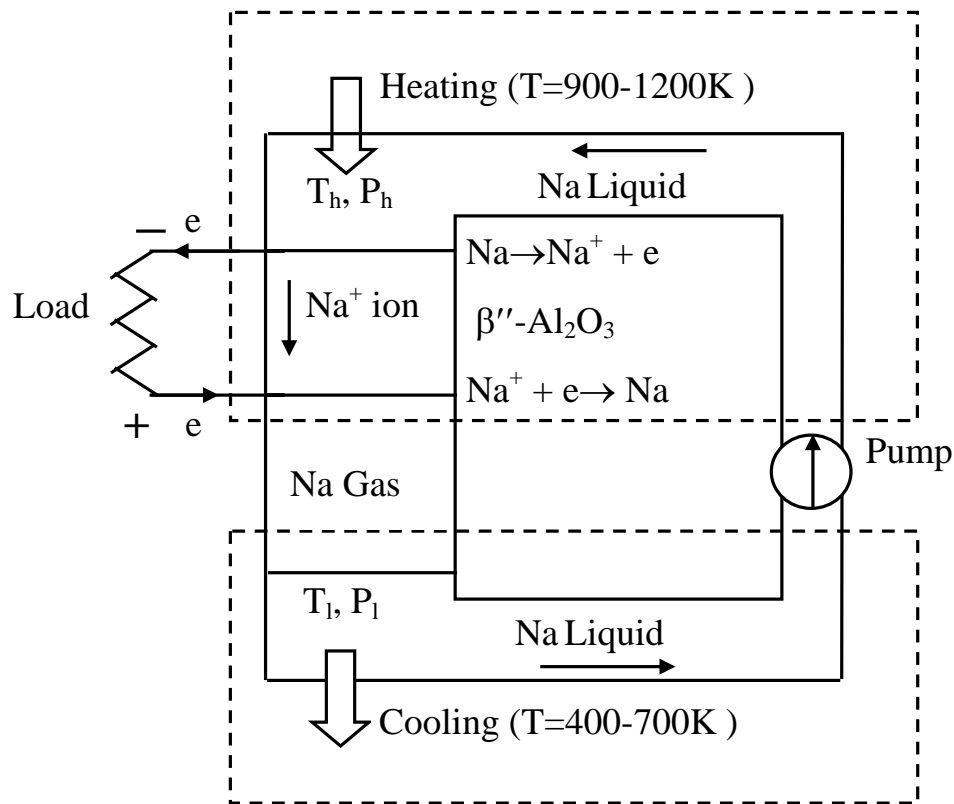
Figure 1.1. Schematic diagram of AMTEC.

In this device, sodium is contained in a sealed loop, which is divided into high and low temperature regions. β''-alumina used as the partition between the high and low pressure areas is a solid electrolyte and coated on both sides with porous electrodes.

High pressure sodium is oxidized at the anode, becoming a sodium ion and releasing an electron in the high temperature region (900-1200K), shown in reaction (1.1). The released electron flows to the cathode through the external load, producing electrical work. The sodium ion passes through the β″-alumina solid electrolyte (BASE) and recombines with the electron from the external load to form neutral sodium on the low pressure side of BASE. This neutral sodium then flows from the cathode to the condenser in the low temperature region (400-700K) and is pumped back to the high temperature region. The electrode reactions and overall cell reaction are shown in reaction (1.1), (1.2) and (1.3).[4,9-12]

Anode reaction:	$Na(P_{high}) \rightarrow Na^+ + e$	(1.1)
Cathode reaction:	$Na^+ + e \rightarrow Na(P_{low})$	(1.2)
Cell reaction:	$Na(P_{high}) \rightarrow Na(P_{low}) + Work$	(1.3)
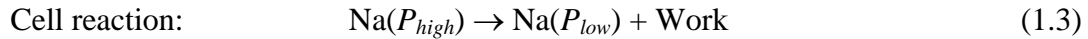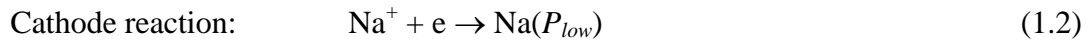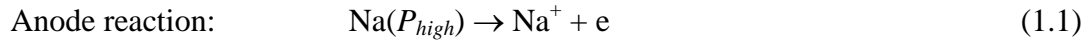
The open circuit potential E_{oc} can be expressed as:

$$E_{oc} = \frac{RT_h}{F} \ln \frac{P_{high}}{P_{low}} \tag{1.4}$$

where R is the gas constant, F is the Faraday constant, T_h is the temperature of AMTEC hot side, and P_{high} and P_{low} are the vapor pressure of sodium at the anode and cathode, respectively.

1.2.2 AMTEC Equipment

An AMTEC device generally contains several BASE tubes connected in series to generate the desired voltage to meet the specified task requirement. A typical AMTEC device, as shown in Figure 1.2, consists of an evaporator, condenser, liquid-return artery

(wick), BASE tubes (7 tubes in this example), porous electrodes, current collectors, α-alumina insulators, and metal braze rings.

The evaporator is located at the bottom of the device while the condenser is on the top. The BASE tubes, electrically connected in series, are brazed to a stainless steel support plate and insulated electrically from the plate by high quality, high purity α-alumina. The thermal energy is input via the cell hot plate at the bottom of the unit and transported to the BASE tubes, which are covered by thin porous electrode on the inner and outer surface as anode and cathode films respectively. High pressure sodium vapor is oxidized within the BASE tube causing sodium ions to pass through the BASE to the outer surface. Sodium ions combine with the electrons to form neutral sodium on the cathode and flow to the condenser, located on the top of the device. The metal felt wick is located in the central tube and serves as a means to pump the sodium working fluid from the condenser back to the evaporator.

Several solid metallic rings around the evaporator enhance the heat conduction path between the BASE tubes support plate and the cell evaporator, increasing both the evaporator temperature as well as the sodium vapor pressure at the anode. The conical evaporator provides a larger surface area for the evaporating liquid sodium to return from the condenser. Finally, encompassing the cell is an axial radiation shield serving to diminish parasitic heat losses to the heat sink.[6,13,14]

Figure 1.2. Picture of AMTEC cell with 7 BASE tubes.

1.3 β″-alumina Solid Electrolyte (BASE)

BASE is a low electronic conductivity yet high ionic conductivity material. This material is the heart of the AMTEC. In β″-alumina, sodium ions are highly mobile and thus readily produce current when an electric field is applied. In this section, we will introduce the crystal structure, basic physical and chemical properties, and degradation of β″-alumina in the AMTEC.

β-alumina family refers to a series of sodium aluminates with closely related structures and chemical properties, with the chemical formula of $Na_2O \bullet x(Al_2O_3)$ (x=5-11). In this family, the most important members are β″-alumina and β-alumina, with β″-

alumina possessing the ability to convert to β-alumina at high temperature.[15-23]   The

structures of these two materials are shown in Figure 1.3.
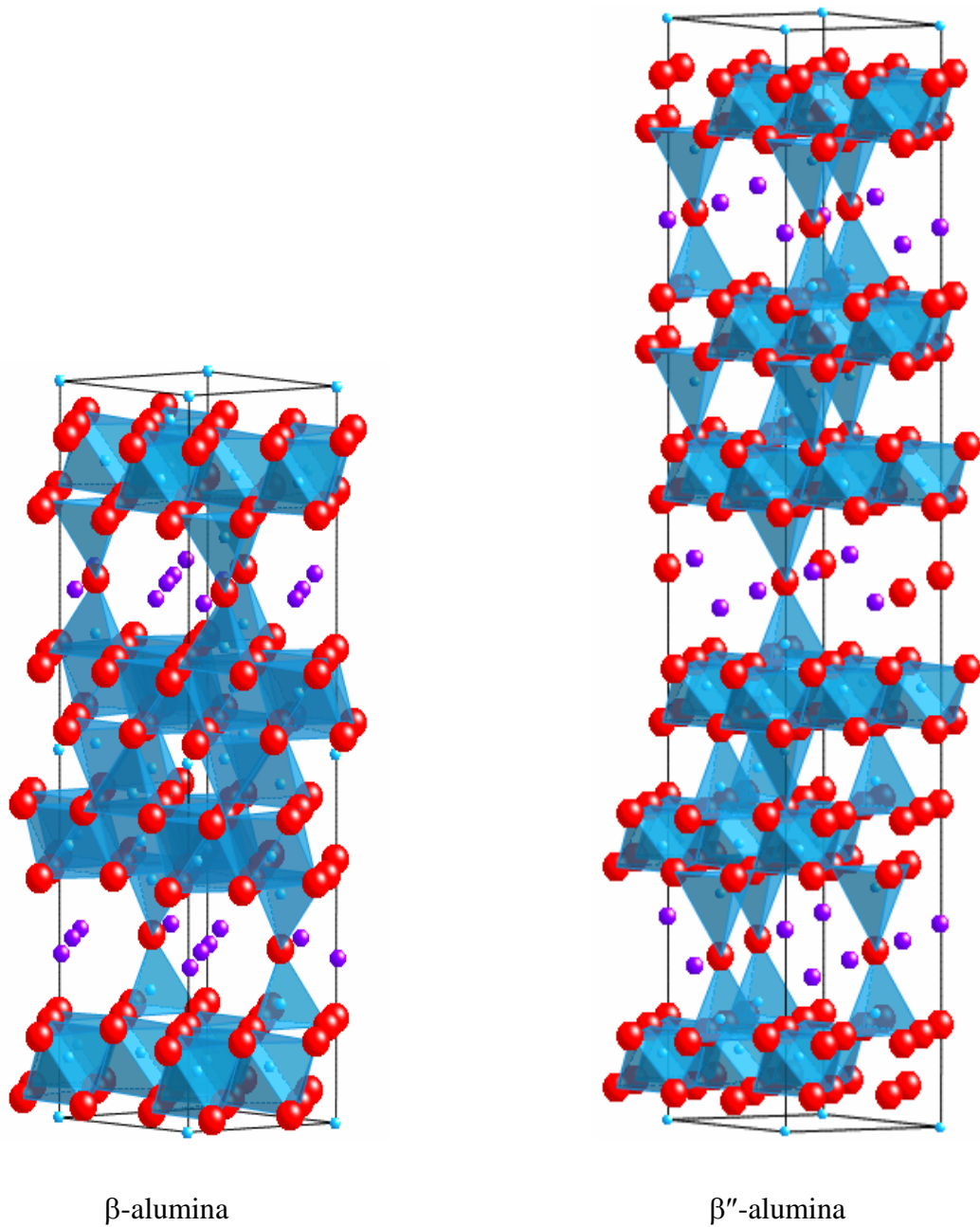
β-alumina   β″-alumina

Figure 1.3. Ideal crystal structure of β-alumina (left) and β″-alumina(right).

1.3.1 Crystal Structure

β''-alumina has a rhombohedral symmetry and with ideal composition of $Na_2O \bullet 5Al_2O_3$, the lattice constants are a=5.59Å, c=33.85Å. It is often soda deficient and is normally stabilized by the addition of MgO and/or Li_2O, normally 7.5% Na_2O and 0.1-0.5% MgO or Li_2O. A typical composition of β''-alumina is $Na_{1.67}Mg_{0.67}Al_{10.33}O_{17}$.

The basic crystal structure of β''-alumina is composed of three Al–O blocks which are separated by two sodium planes, as reported by Yamaguchi in 1968.[24] Each Al–O block consists of four close-packed oxygen layers with Al^{3+} ions occupying the octahedral sites as well as the tetrahedral sites. Al^{3+} and O^{2-} ions are packed in the same fashion as in $MgAl_2O_4$ spinel, with the only difference being the replacement of Mg on tetrahedral sites with Al.

The spinel-type blocks are separated by two kinds of sodium planes. One has Na^+ and O^{2-} ions while the other contains only Na^+ ions, although both are loosely packed. In these planes, there are three kinds of sites for Na^+ ions, called BR(Beevers-Ross), aBR(anti-Beevers-Ross) and mO(mid-oxygen) sites, shown in Figure1.4. Na^+ ions are preferentially located at the BR site at low temperature, while at high temperature, Na^+ ions are statistically distributed over the three sites.[18] Thus Na^+ can be very easily transported along the plane, leading to the high ionic conductivity shown by β''-alumina. However, the conductivity is limited to this plane and movement along the c axis is exceedingly difficult, therefore, this material is highly anisotropic.
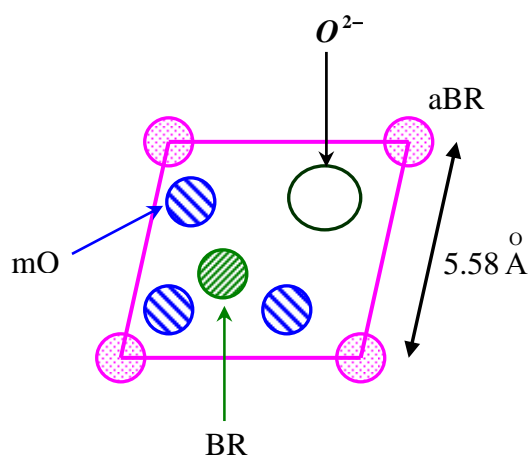
Figure 1.4. Site model of conduction plane of β″-alumina.

β-alumina is in a hexagonal form, and the lattice constants are a=5.59Å, c=22.53Å

for the ideal composition of $Na_2O \bullet 11Al_2O_3$, but it always contains excess soda, and this

nonstoichiometric composition is generally represented by $Na_{1+x}Al_{11}O_{17+x/2}$ with x being

typically 0.2. β-alumina is the more commonly used ionic conducting material and is

already applied in several fields including high-energy batteries.[25]

1.3.2 Physical and Chemical Properties

β-alumina has been investigated widely and its properties are well known. Some of

the physical properties of β-alumina are given in Table 1.1. This table can be used as a

reference to consider β″-alumina's properties, since they are very similar and β″-

alumina's data are not readily available. Some researchers, however, have found that

β″-alumina has lower ionic resistivity than β-alumina at moderate to elevated

temperature. The possible reason for this difference could be the greater number of Na^+

in β″-alumina and the charge of the compensating defects. The high defect charge in β-

alumina could trap Na$^+$ ions in their vicinity and reduce the number of interstitial Na$^+$ ions available for an interstitialcy mechanism diffusion.[17]

β-alumina is stable at elevated temperatures, even in the presence of molten sodium, and has thermodynamic stability essentially the same as Al_2O_3+ Na_2O. Na$^+$ ions in β-alumina can be ion exchanged with other cations, such as Ag$^+$, Cu$^+$, K$^+$, Ti$^+$, Li$^+$. At room temperature, they can be exchanged by water and H_3O^+, resulting in the presence of H_2O and H_3O^+ in the conduction planes, which lead to an increase in resistivity. Therefore, in our research, BASE tubes are stored in a dry atmosphere.

Table 1.1. Some physical properties of β-alumina.

Property	Value
Melting Point	~2253K
Density	3.26g/cm^3
Coeff. Of expansion, a-axis @ 773~873 K	7.7×10^{-6}/K
Coeff. Of expansion, c-axis @ 773~873 K	5.7×10^{-6}/K
Calculated coeff. Of self-diffusion at 298K	4.0×10^{-7}Cm^2/sec
Activation energy of the self-diffusion	15.9kJ/mole (473-673K)
Na$^+$ conductivity @298K	0.033ohm^{-1}cm^{-1}
Na$^+$ conductivity @373K	0.0765ohm^{-1}cm^{-1}
Na$^+$ conductivity @1000K	0.7ohm^{-1}cm^{-1}

1.3.3 Degradation

Due to it has a high melting temperature, good Na^+ ion conductivity and low reactivity, polycrystalline β''-alumina is used in AMTEC as the solid electrolyte and becomes the key to AMTEC operation. Unfortunately, BASE degrades over time during the AMTEC operation, which reduces AMTEC efficiency. This degradation of BASE can be thought of as two main mechanisms, thermal breakdown and chemical contamination.[26-28]

Thermal breakdown involves several processes at AMTEC working temperature. The first of these is sodium loss. Sodium in the BASE conductive plane could be lost during AMTEC operation, which results in a decrease in the BASE's ionic conductivity. With sodium loss, the β'' phase converts to the β' phase and finally to α-alumina, which is not an ionic conductor.

The second process is the formation of molten dendrites. Due to the high temperature and flow of the charge, molten sodium dendrites could be formed within the BASE structure. As these dendrites increase in size and propagate through the structure, they can ultimately cause an electrical short between the cathode and the anode causing electrons to flow directly between these two surfaces and thus reducing the amount of charge flowing through the external, load-bearing circuit.

The third process is crack formation. A crack is a void or discontinuity in a material that has a propensity to grow or increase in size, which could cause the material to finally rupture and fail. Sodium ion migration leads to intergranular weakening and fracture. If the crack propagates through the thickness of the BASE tube, a short or

opening is created between high pressure and low pressure sodium regions of the cell, which will result in leakage of Na vapor and reduced power output.

Finally, the fourth of these processes is microstructure change. β''-alumina is highly anisotropic due to conductivity limited to the Na^+ planes. In AMTEC, polycrystalline β''-alumina is used to get good conductivity in all orientations. However, high temperature combined with sufficiently long periods of time cause grain growth, and the coalescence of grains may cause microscopic voids in the material thereby greatly increasing resistance to ion transport.

In AMTEC devices, chemical contamination can occur when elements such as chromium and manganese from stainless steel react with BASE and form $Cr_2O_3 \bullet Al_2O_3$ and $MnAl_2O_4$. These materials may also substitute for Na^+ in the conduction layer of the BASE crystal. Contaminants in the BASE like $NaAlO_2$ also have a deleterious effect on ionic conductivity, mechanical strength and chemical stability.

1.4 Key Issues in AMTEC Performance Operation

For an AMTEC device to be feasible for either space or terrestrial applications, it requires a high power density and a long lifetime of 7-15 years. For this reason, research efforts have been focused on improving AMTEC efficiency and lifetime.

The efficiency of AMTEC under load is the specific output power of the electrode divided by the total heat input required per unit area of electrode, which given as

$$\eta = \frac{V * j}{jV + \frac{j}{F}[\Delta H_{vap} + C_p(T_{high} - T_{low})] + Q} \tag{1.5}$$

Here, V and j are the output voltage and current density, F is Faraday constant, C_p is the specific heat of liquid sodium, ΔH_{vap} is the molar vaporization enthalpy of liquid sodium, and Q is the parasitic heat losses.[4]

Based on this equation, there are two ways to raise the efficiency. One is improving output voltage or current and the other is reducing the parasitic heat losses. Achieving the former requires reducing electrochemical losses, while achieving the latter requires reducing thermal losses. Moreover, there are some losses owing to degradation of components such as the electrodes and the electrolyte over time.

Thermal losses in an AMTEC cell consist primarily of radiative loss (Q_r) and conductive loss (Q_c), shown in equation (1.6).

$$Q = Q_c + Q_r \tag{1.6}$$

Conductive loss is the heat loss due to conduction from the hot region through the output current leads and supporting structure for the BASE, which could result in a condenser temperature higher than its optimum. Radiative loss is the heat loss due to radiation from hot surfaces through the vapor space to the condenser. Q_c is determined by the dimensions and thermal conductivities of the electrical leads and structural members of the device, while Q_r is determined by knowledge of the emissivities of the hot surfaces and condenser surfaces and the geometric configuration of the device. Therefore, recent research on thermal losses is concentrated on constructing a thermal model, describing and simulating thermal characteristics of components of cells, and designing and optimizing systems.[29-31] We will not focus on this aspect in this research.

Electrochemical losses are the losses related to electrochemical reactions and transport processes. The core of an AMTEC cell is the electrode and BASE assembly. Sodium oxidation and reduction, sodium vapor transport through the electrode material, current collection and electron flow to and from the electrodes, all occur on the electrode/BASE assembly and all contribute to the electrochemical losses and finally determine current-voltage characteristics, i.e. electrical energy output.

Internal resistance of the cell includes pressure losses due to sodium flow through the device, contact and sheet resistance, and potential-dependent resistance, which is designated as the apparent charge-transfer resistance, R_{act} (interfacial kinetics losses and flow of Na vapor through the electrode from the interface and then away from the electrode surface). Therefore, it is very important to understand and improve these electrochemical processes in order to minimize these losses and improve the efficiency of AMTEC. The theory of kinetics and transport in the AMTEC electrode/BASE assembly must be further developed to achieve these goals.

Most of the electrochemical losses can be minimized, although not eliminated, by choosing the electrode material, morphology, and current collection network and improving connecting technology. This research will focus on reducing electrochemical losses by the choice of electrode materials and understanding electrode kinetics.

Another key issue for AMTEC is the degradation characteristics of the cells, which determine the lifetime of an AMTEC power converter. This degradation includes electrode performance degradation, capillary pumping system degradation and BASE degradation, as described in the previous section. Previous AMTEC research has shown

that, over the time scales studied (up to 8000h), the electrode is the component most likely to influence device performance and limit operating lifetime.[32]

AMTEC electrode degradation modes include growth of electrode grains, reduction of electrode porosity, segregation of electrode components, evaporation of electrode material, formation of new compounds, and separation between electrode and current collector.

At AMTEC operating temperatures, grains of electrode materials will grow and coalesce, which will dramatically reduce electrode performance. Grain coalescence reduces the total reaction area and electrode porosity, and changes the pore size and shape, which determines the efficiency of sodium transport and influences the potential drop in the electrode. Additionally, electrode composition could be changed. Some components could evaporate and leave the electrode or react with the environment to form new compounds, which could be volatile or have low conductivity. Due to different diffusion coefficients, electrode components can concentrate and create a non-uniform structure. Finally, due to different thermal expansion coefficients, the electrode and current collector can separate, which will greatly reduce the output current by increasing the series resistance.[33-38]

1.5 AMTEC Electrode Studies

The above discussion shows that the electrode is a key issue in AMTEC development, because it is the component most likely to influence AMTEC performance and limit operating lifetime. Comparing anode and cathode, it is found that cathode is

more demanding, because sodium vapor activity is high at the anode and it is more reversible. Therefore, the electrode development and degradation studies have focused on the cathode.

An AMTEC electrode must meet the following requirements in order to achieve the desired performance.[39]

1. The electrodes must be stable for long periods of time at AMTEC operating temperate (700-1000°C for 15 years), which require the electrodes to have a high melting temperature above AMTEC operating temperatures, a thermal expansion coefficient near that of BASE, and very low vapor pressure at AMTEC temperatures.

2. The electrode must be chemically and thermally compatible with other components in the cell, including sodium and the BASE. It must not form new phases with other components of the cell, which would adversely affect the performance of the cell.

3. The electrode must provide reaction sites for sodium reaction and oxidation to occur. Large reaction areas are necessary for producing high current at useful voltages.

4. The electrode must provide paths for electrons from the sodium oxidation sites to the current collector, and from the current collector to the sodium reduction sites, which requires that the electrode must have good electronic conductivity.

5. The electrode must provide a means of sodium transport between the reaction sites and vapor space. It requires that the electrode is capable of high rates of ionic or diffusive transport of sodium.

Refractory metals and their alloys could meet these requirements, including Mo, W, Ir, Ni, Ti, WRh_2, and WRh_3.[40-44] Sputtered Mo electrodes have been studied widely as applied to AMTEC, and have shown high power densities and the best initial performance of all studied metal electrodes. However, molybdenum forms volatile Na-M-O compounds during the AMTEC operation, which dramatically reduce Mo electrode lifetimes.[44,45] Similar behavior is also found in the W electrode system.[38]

Ceramic materials are another electrode candidate group, which are stable at AMTEC operating temperatures and have thermal expansion coefficients comparable to that of BASE. Some nitrides, oxides and carbides of transition metals (IV, V and VI groups) have been investigated, such as TiN, TiC, NbN, NbC.[46-49] Also, some ceramics such as MoN, ZrN were considered as electrode materials, but MoN was found to have positive Gibb's free energy at AMTEC temperatures, and ZrN oxidizes at AMTEC operating temperature. Currently, TiN has shown good performance for a long time and is used as a standard AMTEC electrode.

For both metal and ceramic electrode materials, however, charge transfer reactions occur only at electrochemically active sites, i.e. a point where the vapor space, the electronic conductor, and the ionic conductor are in close contact, also called the triple-phase boundary (TPB). Typically, for metal electrodes, the ratio of active site area to the overall electrode area is about 10^{-4}, which significantly limits the current production.

There are two possible approaches to increase the reaction site density. The first method is to reduce the electrode particle size, for example, by using nano-particles. Unfortunately, these small particles are more likely to grow or coalesce (sintering behavior) during the AMTEC operation in addition to increasing the cost of AMTEC. The second method is to develop mixed ionic-conducting and electronic-conducting electrodes (MIEE). This mixed electrode offers the potential to increase reaction site density per unit electrode surface area, since it can extend the active area three-dimensionally into the electrode thickness, due to internal sodium ion transport. Additionally, MIEE may maintain the porosity of the electrode by forming a framework of ceramic to help control the sintering behavior of the metal and effectively adjust the thermal expansion coefficient of the electrode to help reduce thermal stresses, which could improve the lifetime of electrode. Although electrical resistance and sodium conduction are both properties of the electrode, the physical morphology of the electrode plays an equally important part. Characteristics of the electrode, such as the porosity, thickness, grain size, and quality of contact at the electrode-electrolyte interface, can all affect the conduction of both electrons and sodium to and from the reaction sites. Therefore, developing an MIEE is an attractive alternative to improve the efficiency of AMTEC.

The first step in the development of an MIEE is to find an appropriate sodium ion conductor. Obviously, β''-alumina is the best candidate and at present, the Mo/β''-alumina electrode is the only MIEE that has been investigated experimentally.

Unfortunately, this MIEE displayed inconsistent performance in the lab, the reasons for which still being unclear.[50]

There are other sodium conductors, such as $Na_2Ti_3O_7$, Na_3PO_4, Na_2MoO_4, NASICON ($Na_{1+x}Zr_2(PO_4)_{3-x}(SiO_4)_x$ 0<x<3), and $Na_{0.9}Mg_{0.45}Ti_{1.55}O_4$. Among these sodium conductors, some, such as Na_3PO_4, have melting points lower than AMTEC operating temperatures, some have high vapor pressure at AMTEC temperatures, such as Na_2MoO_4, and some have only one dimension sodium ion conductivity, such as $Na_{0.9}Mg_{0.45}Ti_{1.55}O_4$. Sodium titanate ($Na_2Ti_3O_7$ or $Na_2Ti_6O_{13}$) appears to be a good candidate, because of its high melting point, compatibility with BASE and low cost.[51] Its properties will be described in next section. Since metal/sodium titanate MIEEs have not been previously reported as electrode materials, this research focuses on preparation and performance studies of these mixed electrodes for AMTEC operation.

1.6 Sodium Titanate Materials

Sodium titanates refer to a composition series of ternary oxides of sodium with titanium dioxide, $Na_2O \bullet nTiO_2$, (n=3~8), which crystallize in a monoclinic structure. $Na_2Ti_3O_7$ is a member of this family, whose crystal structure was first reported in 1961 with unit-cell dimensions of a=8.571Å, b=3.804Å, c=9.135Å and β=101.57°.[52] The basic framework of $Na_2Ti_3O_7$ is built up by three TiO_6 octahedra-sharing edges at one level, as shown in Figure 1.5. These units are joined to similar blocks above and below by additional edge sharing, which forms zigzag strings extending in the direction of the b axis. The strings are combined by sharing the corners of the octahedra to form staggered

sheets, which stack in the a-direction. These form a layered structure with the composition $(Ti_3O_7)^{2-}$. Sodium ions hold these layers together and occupy the interlayer regions at the levels $y=1/4$ and $3/4$.[51] The crystal structure allows sodium mobility in the interlayers. Therefore, sodium titanates have been used in ion exchange processes, as ceramic capacitors, dielectric resonators in microwave oscillators band pass, reinforcing agents of plastics, adiabatic materials and an oxygen electrode for potentiometric gas sensors. [53-56]

The crystal structure suggests that sodium titanates should be a sodium ion conductor, since the sodium ion can move along the layers easily. However, only few data are available in the literature about sodium titanate's electrical properties up to now, and these data are measured by different researchers and show inconsistence.[57-59] Therefore, it is necessary to measure the conductivity of sodium titanate.

Sodium titanate has a high melting point of 1401K, which is higher than the AMTEC operation temperature and since it is a ceramic, its thermal expansion coefficient should be close to that of BASE, although the exact value is not available. Therefore, sodium titanate could certainly be considered as ionic conductor candidate for an MIEE of AMTEC.

Before making this statement however, the question of whether or not $Na_2Ti_3O_7$ is chemically compatible with other components in the cell, including sodium vapor, the metal component in the electrode, and the BASE must be answered. Sodium titanate is a stable chemical, and likely does not react with individual components of the cell, but when all the components are present; it could cause a system-level affect or catalyze

some reactions that may not occur when simply examining the individual components. In this research, we will calculate the reaction Gibbs free energy for all possible reactions in Na-Al-Ti-O system and plot the chemical potential diagram to analyze the stable chemical form or phases present in this system, as well as reactions possibly occurring between electrode and electrolyte.
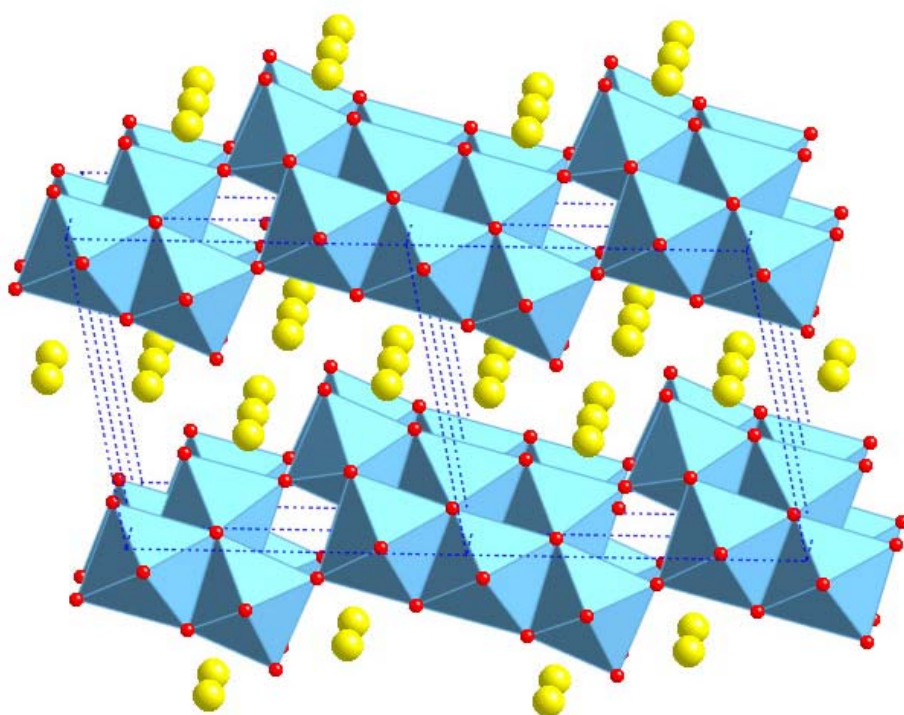
Figure 1.5. Crystal structure of $Na_2Ti_3O_7$.

1.7 Objective

To improve AMTEC's performance, a key issue is the development of a highly efficient electrode, especially the cathode. In this research, the primary objective is to develop metal/ceramic mixed ionic and electronic conducting electrodes, measure their performances as a function of time, optimize their composition and analyze electrode kinetics.

In the first part of this dissertation, the MIEE preparation is discussed. First we select metal candidates based on their physical and chemical properties, and theoretically analyze their stability and compatibility with other components in a MIEE. Then the selected metal candidates are tested as AMTEC electrode and measure their performance. Based on the performance and morphology of electrodes, the metal component is determined. We use selected metals mixed with sodium titanate or β''-alumina ceramic to prepare a series of MIEEs with different composition, and then the relationship between the performance and composition are examined experimentally. Finally, a theoretical model is developed to explain the experimental results and predict the optimal composition for MIEEs.

In the second part of this dissertation, the kinetic mechanisms are identified for pure metal electrodes and MIEEs. First, the ionic conductivity of sodium titanate used in this research is measured in AMTEC conditions. Then, applying the electrochemical theories into electrode systems and combining with experimental results, the kinetic mechanisms of the pure metal electrode and MIEE are proposed and discussed. Finally,

the expression of the interface impedance is theoretically derived based on the proposed kinetics for both pure metal electrode and MIEE.

The last part of this dissertation is the performance examination of different kinds of MIEEs. In this part, two kinds of MIEEs are studied, metal/β''-alumina and metal/sodium titanate MIEEs, and for each kind of MIEE, a series of electrodes with different compositions are prepared and tested. The functions of different metal components in the MIEE are discussed and the performances of metal/β''-alumina and metal/sodium titanate MIEEs are compared. Finally the performance of all tested MIEE are described and analyzed.

In summary, AMTEC electrode study is still in a fundamental stage. In this research, we propose the MIEE for AMTEC operation and compare to the pure metal electrode. By studying several reasonable MIEEs, we try to find the electrode with the best performance and understand the electrochemical kinetic mechanisms.

CHAPTER II

EXPERIMENTAL

2.1 Experimental Apparatus

In order to accurately evaluate the performance of AMTEC electrodes, it is important to isolate the electrode from other components. The Sodium Exposure Test Cell (SETC) is specifically designed to simulate AMTEC electrode working conditions and examine electrode performance, without having to run a complete AMTEC cell.[60]

The SETC consists of a stainless steel tube chamber with a length of 49cm and a 7.5cm diameter and a sodium containment, or sodium pool, as shown in the Figure 2.1. α-alumina rods are used to support test samples and are held in the manifold with Epoxy-Patch insulating epoxy, which forms a vacuum tight seal. The chamber is evacuated and then heated to AMTEC operating temperatures, while the temperature of sodium containment or pool is kept at AMTEC condenser temperatures.

The SETC is a non-power-producing cell, unlike AMTEC. Its anode and cathode are in the same environment, which is similar to that of the cathode of AMTEC. Electron flow is driven not by the difference of the sodium chemical potential, but by the external power, applied as a voltage difference between the electrodes. The SETC provides a sodium vapor pressure of the same order of magnitude as that found on the cathode side of AMTEC cells. All processes occurring on the anode, cathode and BASE in a SETC are the same as those in the AMTEC cell. The experimental results have proved that performance of the electrode and the electrolyte in AMTEC cells can be tested in an

SETC, and performance parameters, which correlate with those taken from AMTEC operation, can be calculated from data taken in an SETC.[60] Therefore, all the experimental results for electrode performance in this research are measured by the SETC in our lab.

The chamber is lined with niobium or titanium metal to prevent volatiles from the stainless steel such as chromium and manganese from contaminating the test samples. The manifold also includes a pump out port and a sodium fill port. The pump-out port connects to the turbo molecular vacuum pump that is backed by a roughing pump.

Before operation, the SETC needs to be baked out in order to remove the water and inorganic contaminants in it, beginning with ~220ºC, then to ~440, ~660, ~880, and finally ~1100ºC and holding each temperature for 4 hours. After the assembly is outgassed and the temperature is reduced to ~400ºC, approximate 20g of liquid sodium is introduced into the sodium pool. Finally, the end of SETC having samples is heated to the operating temperatures of 600-900ºC, while the sodium pool is kept at a temperature of ~300ºC.

There are 4 test samples in the chamber, which are placed in the hot end. Each sample consists of a cylindrical β"-alumina solid electrolyte (BASE) tube with 4 electrode bands, each approximately 0.25cm wide, deposited on the outer surface of the BASE and separated by 0.25cm bands of bare BASE. The electrodes are covered by Ni or Cu metal mesh, which acts as the current collector. Ni or Cu leads are used to tie these current collectors onto the BASE tube and are threaded through α-alumina rods to the outside of the manifold, where they are connected to the EIS equipment.
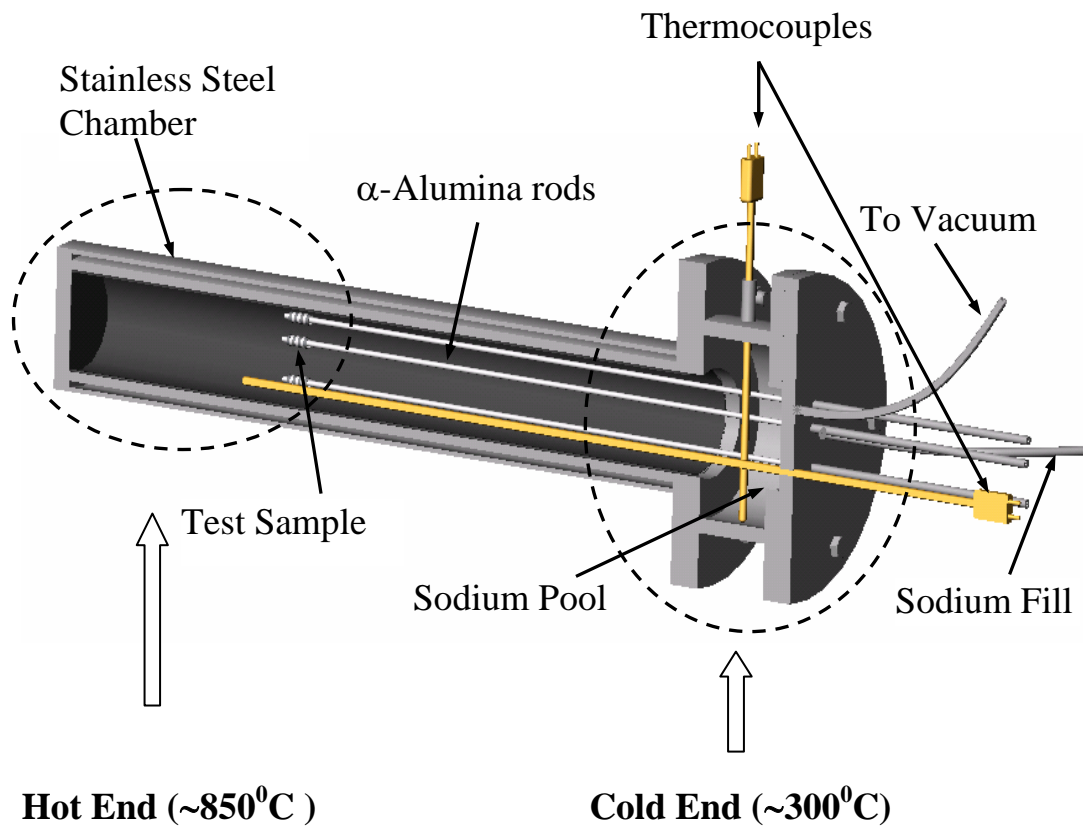
Figure 2.1. Schematic drawing of the sodium exposure test cell.

2.2 Techniques

2.2.1 Electrochemical Impedance Spectroscopy

Electrochemical Impedance Spectroscopy (EIS) has become a mature technique that has been seen a tremendous increase in popularity in recent years. This method probes the system response to the application of a small amplitude ac signal, which usually is a voltage between 5 to 50 mV over a range of frequencies of 10^5 Hz to 10^{-3} Hz. The response is the complex impedance (Z) that is defined as the ratio of voltage($V(\omega)$) to current ($I(\omega)$) and varies as the frequency(ω) of the applied voltage changes. The EIS instrument records the exact impedance including the phase angle ($\phi(\omega)$), real (Z_{re}) and imaginary (Z_{im}) components of the impedance at every frequency applied and displays them graphically using two types of plots, the Nyquist plot (also known as complex plane or Argand plots) and the Bode plot. The Nyquist plot is a graph of the imaginary versus the real components of the impedance, plotted for various frequencies. That is, each point on the Nyquist plot is the impedance at one frequency. The Bode plots are log|Z| (magnitude) and phase angle $\phi(\omega)$ verse log(ω).[61-65] Figures 2.2(c) and (d) show typical Nyquist and Bode plots.

EIS theory is based on analogies between the electrochemical process and networks of electrical elements, such as resistors, capacitors and inductors, which are thought to behave like the electrochemical cell.   Therefore, an electrochemical system's performance can be represented by an equivalent circuit of electrical elements that pass current with the same amplitude and phase angle as the real cell does under a given excitation. For the very basic electrochemical process, which only includes one step,

that is, a charge transfer reaction on the interface between electrode and electrolyte, an equivalent circuit, called the Randles' circuit, is used to represent it. Figures. 2.2(a) and (b) show the process and the circuit. The parallel elements are introduced because the total current through the interface is the sum of distinct contributions from double-layer charging, i_c and the faradic process, i_f, which is the only charge transfer reaction here. The double-layer capacitance is nearly a pure capacitance, hence it is represented in the equivalent circuit by the element C_{dl}. A resistor R_{ct} is used to represent the charge transfer process. Of course, all of the current must pass through the solution resistance; therefore R_s is inserted as a series element to represent this effect in the equivalent circuit.

$$O + \text{ne} \leftrightarrow R$$

O ------- Oxidant R ------- Reductant
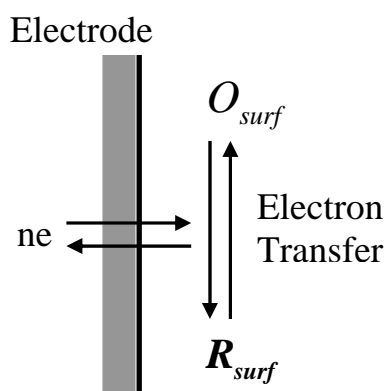
(a) Charge transfer reaction

Figure 2.2. (a) Charge transfer electrochemical process. (b) Randles' equivalent circuit. (c) responded electrochemical impedance spectrum, Nyquist plot and (d)Bode plots.
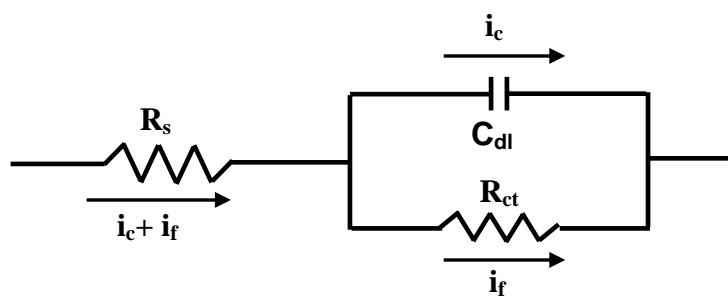
(b) Randles' equivalent circuit
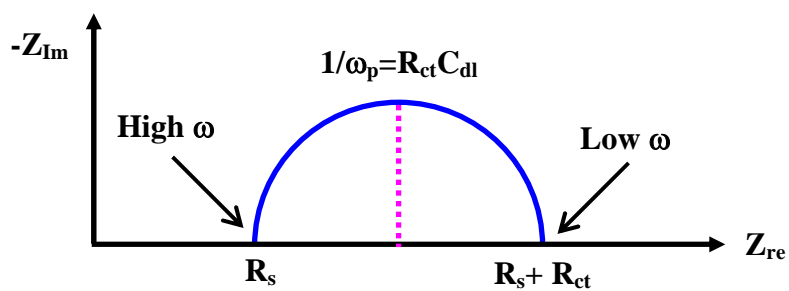
(c) Nyquist plot
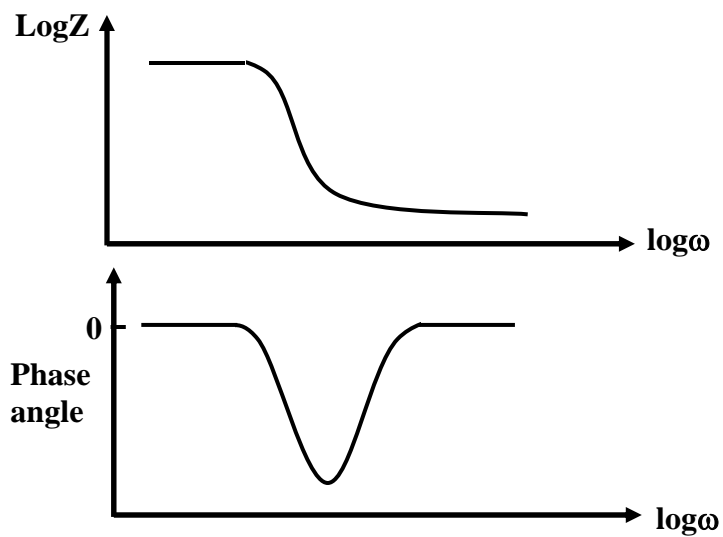
(d) Bode plots

Figure 2.2. (Continued)

The impedance of this system is given as

$$Z(j\omega) = R_s + \frac{1}{1/R_{ct} + j\omega C_{dl}} = R_s + \frac{R_{ct}}{1+\omega^2 R_{ct}^2 C_{dl}^2} - \frac{j\omega R_{ct}^2 C_{dl}}{1+\omega^2 R_{ct}^2 C_{dl}^2} \tag{2.1}$$

$$Z_{re} = R_s + \frac{R_{ct}}{1+\omega^2 R_{ct}^2 C_{dl}^2} \tag{2.2}$$

$$Z_{im} = -\frac{\omega R_{ct}^2 C_{dl}}{1+\omega^2 R_{ct}^2 C_{dl}^2} \tag{2.3}$$

There are two limits of the impedance, when $\omega=0$, $Z_{re}=R_s+R_{ct}$, and $Z_{im}=0$; when $\omega=\infty$, $Z_{re}=R_s$, and $Z_{im}=0$. Analyzing Z_{re} and Z_{im}, equation 2.4 is found.

$$\left(Z_{re} - R_s - \frac{R_{ct}}{2}\right)^2 + Z_{im}^2 = \left(\frac{R_{ct}}{2}\right)^2 \tag{2.4}$$

Because Z_{im} only has negative values, Equation 2.4 represents a semicircle centered at $R_s + \frac{R_{ct}}{2}$ on the real axis and having a diameter of R_{ct}, shown in Figure 2.2(c). The intercept at high frequency (on the left) on the real axis gives the value of R_s, and the intercept at the low frequency (on the right) is the sum of resistance of R_s and R_{ct}. Additionally, the point at the semicircle maximum, i.e, the higest Z_{im}, corresponds to the frequency $\omega=1/R_{ct}C_{dl}$. The Bode plots are shown in figure2.2 (d). The graph of log|Z| versus logω contains two breakpoints, and the phase angle graph shows the phase angle is 0° at both low frequencies and high frequencies and has a maximum when frequency is equal to

$$\omega = \frac{1}{R_{ct}C_{dl}} \sqrt{\frac{R_s + R_{ct}}{R_s}} \tag{2.5}$$

It should be noted that the frequency corresponding to maximum of the phase angle is different from that of maximum of the imaginary part of impedance. By analyzing Nyquist and Bode plots, the values of elements in the equivalent circuit can be obtained. These elements can represent all kinds of electrochemical processes occurring in the electrochemical system.

For a real electrochemical system, an overall electrode reaction process that causes the conversion of the oxidized species, O, to a reduced form R, is composed of a series of steps, shown in Figure 2.3. In general, the current (or electrode reaction rate) is governed by the rates of processes such as

1. Mass transfer (e.g. species O from the bulk solution to the electrode surface).

2. Electron transfer at the electrode surface.

3. Chemical reactions preceding or following the electrode transfer. These might be homogeneous processes or heterogeneous ones on the electrode surface.

4. Other surface reactions, such as adsorption, desorption, or crystallization (electrodeposition).

The EIS results can be complicated for an AMTEC electrode, but by using equivalent circuits, it is possible to separate and quantify the individual resistances for each electrochemical step, if they have sufficiently different time constants. Further, we can gain information as to what kind of steps really occurred in the SETC, which is the most important advantage of EIS over other laboratory techniques. Additionally, we can determine system kinetics and calculate kinetic parameters, such as activation energy of

the electrode reaction, the transfer coefficient α, the diffusion coefficient, and other basic kinetic parameters for an electrochemical reaction.

Another advantage of EIS is that the excitation waveforms used have a very small magnitude and cause only minimal perturbation to the electrochemical test system, thereby obtaining the response of the system following the perturbation near steady state. This approach is different from other electrochemical techniques, such as potential sweeps, potential steps, or current steps, which drive the electrode to a condition far from equilibrium, and for which the response is usually a transient signal.[66]
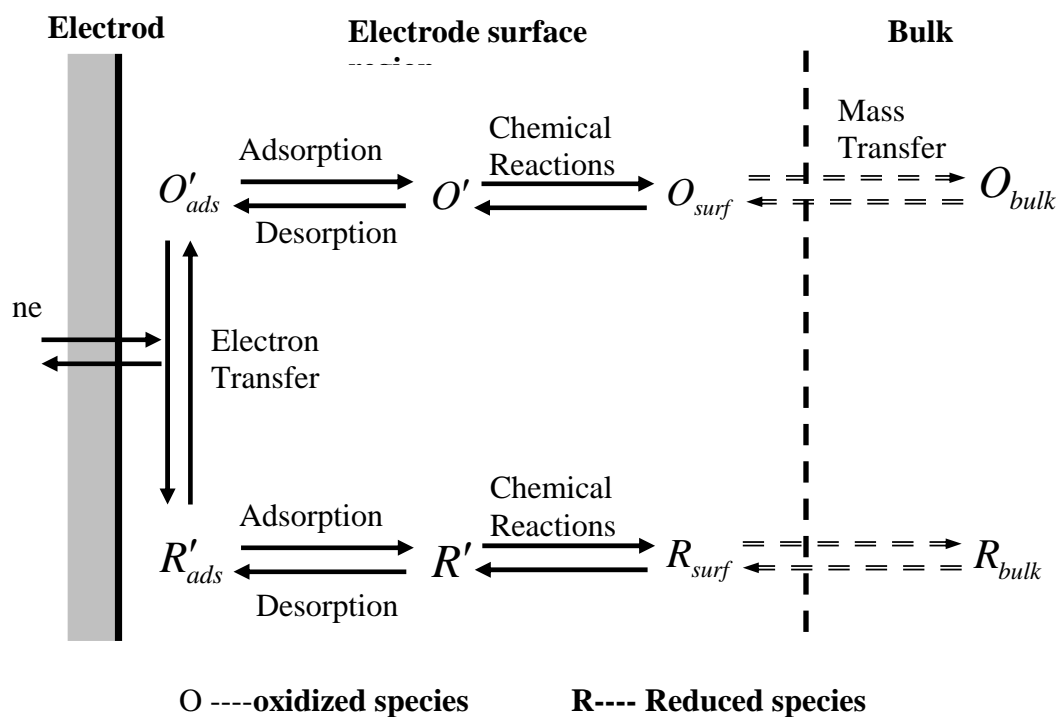
Figure 2.3. Pathway of a general electrochemical process.

Other advantages of this technique are rapid acquisition of data, accuracy, reproducibility, effectiveness in low conductivity media and that it is non-destructive. Therefore, EIS is a very effective tool for characterizing a real electrochemical system and was used throughout this study.

Figure 2.4 shows the EIS instrumentation used in our lab. It includes a Solartron 1287 Electrochemical Interface (ECI), which is a high accuracy and wide bandwidth potentiostat/galvanostat capable of handling sample polarization and measurements, and a Solartron 1250 Frequency Response Analyzer (FRA), which is used to generate and measure the ac signals. The computer and software are for controlling the ECI and FRA and recording and displaying measurement results. The impedance results were analyzed using Z-plot and complex nonlinear least-squares (CNLS) software.

Figure 2.4. Equipment of electrochemical impedance spectrum. 1. electrochemical interface (ECI) 2. frequency response analyzer (FRA) 3. computer and software.

2.2.2 Scanning Electron Microscope

The Scanning Electron Microscope (SEM) is capable of producing high resolution topographic electron images, where its high resolution and depth of field give it a great advantage over optical microscopy. The instrument includes an electron gun, a series of magnetic lenses, a set of scanning coils, detectors, amplifiers, and monitors. The electron gun is on the top of the vacuum column, and it emits a beam of high energy electrons. This beam travels downward through a series of magnetic lenses designed to focus the electrons into a fine probe incident on the surface of the specimens. Scanning coils move the focused beam back and forth across the specimen. As the electron beam hits each spot on the sample, secondary electrons and backscattered electrons are emitted from its surface. The detectors count these electrons and send the signals to an amplifier and to the monitors. The final image is built up from the number of electrons emitted from each spot on the sample.[67]

The SEM can create secondary electron (SE) images, backscattered electron (BSE) images and characteristic x-ray maps. SE images are sensitive to surface topography, because the number of secondary electrons emitted is dependent on the surface topography. Thus SE images are used primarily for displaying topographic data, which can show a well-defined, three-dimensional appearance. The BSE images are used primarily for providing composition information, because the BSE yield varies monotonically with the atomic number. Characteristic x-ray maps can identify elements present in the sample and their distribution.

In this research, we use this technique to analyze morphology characteristics of electrode film, including the particle size, particle distribution, electrode thickness, porosity and composition change.

2.2.3 Sputtering

Sputtering is a physical vapor deposition technique, discovered in the 1850's. With the advent of modern vacuum technology, it has become one of the most widely used techniques for depositing thin films with high quality. Sputtering works by bombarding a target material with high-energy particles such that atoms or molecules are ejected and condense on a substrate as a thin film.[68-71]

As shown in Figure 2.5, sputtering is performed in a vacuum chamber, in which sputtered material, usually called the target, working gas and substrate are located. The vacuum chamber is first evacuated to a base pressure of 10^{-6} to 10^{-10} torr, depending upon the process, and then backfilled by the working gas to a pressure of between 10^{-3} and 10^{-1} torr. A negative potential, typically between 0.5 and 5 kV, is applied to the target, and the substrate is grounded, so target and substrate work as a cathode and anode. The working gas, typically Ar, is ionized, forming a glow discharge plasma. Positive Ar ions in the plasma are accelerated and drawn towards the target and strike it with a kinetic energy of several hundred eV. This powerful impact will dislodge atoms of the target into the vapor phase. The dislodged target atoms will have substantial kinetic energies and transport to the substrate through a region of reduced pressure. When they arrive at the substrate, they condense, nucleate and grow to form a thin film. Generally, the sputtered layers adhere well to the substrate.

Sputtering approaches include diode sputtering, radio frequency (RF) sputtering, magnetron sputtering and reactive sputtering. Magnetron sputtering is the current workhorse of the sputter deposition field, used in perhaps 95% of all sputtering applications. Our device is a magnetron sputtering.

The most important parameters controlling the growth and properties of the films by sputter deposition processes are: 1) target voltage and current, 2) working gas partial pressure and flow rate, and 3) substrate temperature and substrate bias. Therefore, by adjusting these parameters, it is possible to use sputtering to deposit films with extremely high quality.

There are a few limitations on sputtering as a deposition technique. For example, organic solids are frequently unable to withstand ion bombardment and some materials are incompatible with good vacuum because of their volatility. In general, sputtering is a versatile process applicable to thin film deposition of electrically conducting and insulating materials, elemental materials, alloys, and compounds.

We used a Hummer 8 magnetron sputtering (Anatech, Ltd) to deposit Mo, MoRe, Ta, Nb, WRe and Ir electrodes on BASE tubes and disks in this research.
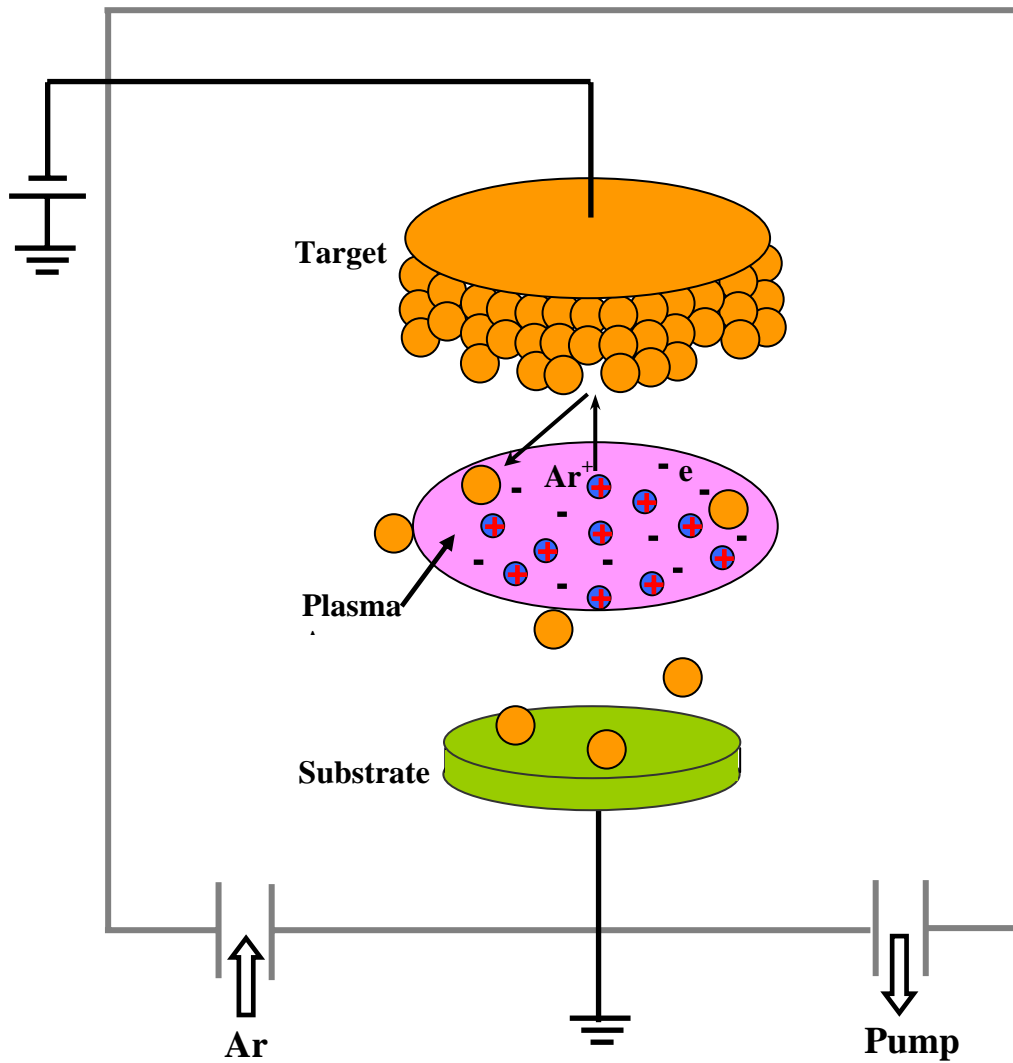
Figure 2.5. Schematic drawing of the sputtering process.

2.2.4 Flame Spraying

Flame spraying is the most basic form of thermal spraying. It generally uses an oxyacetylene flame to melt and propel a coating material in the form of powder or wire at high velocity onto a substrate where solidification occurs rapidly, forming either a protective coating or a bulk shape. Flame spraying results in fine, chemically homogeneous coatings, where there is no change in composition with thickness. But due to low flame temperatures and medium particle velocity, the coating could be low density and have low adhesion.[69-70]

Because considerable heat is imparted to the substrate and the solidification occurs rapidly, thermal degradation of substrate properties and the coating could occur. Both the substrate and coating contract upon cooling, which can generate high residual stresses if a significant difference in coefficients of thermal expansion exists and these stresses can lead to coating delamination. Additionally, a metal substrate or coating could be oxidized in the deposition process. However, flame spraying is simple in principle and operation, and system and production costs are low, comparing to other thermal spraying, such as plasma spraying.

In this research, we use this technique to deposit most of mixed metal and ceramic electrodes on the BASE surface.

2.2.5 Coulter Counter

A Coulter counter is an apparatus to count and size particles and cells, utilizing the technology known as the Coulter principle (electrical sensing zone method). This technology was originally developed by Wallace H. Coulter as a method to count blood cells, and later it was transferred into industrial applications. Now, it has become the accepted "reference method" throughout the world for particle size analysis and widely used in both industrial particle characterization and for biological applications, providing the highest resolution available for particle sizing and counting.[72-73]

The Coulter method is based on measurable changes in electrical resistance as nonconductive particles suspended in a conductive solution are swept through a small aperture of known diameter and length. Figure 2.6 is a diagram of the Coulter counter, including a conductive solution, two electrodes and a glass aperture tube. Two electrodes are submerged in the solution and separated by the glass aperture tube. When voltage is applied between them, a "sensing zone" is created around the aperture. Particles being measured are suspended in the conductive solution. If a vacuum is applied to the top of the glass tube, the solution with the suspended particles will flow into the glass tube through the aperture. As each particle passes through the aperture it displaces its own volume of electrolyte, momentarily increasing the resistance of the aperture and a voltage pulse is measured. This pulse's amplitude is directly proportional to the volume of the particle. Scaling these pulse heights in volume units enables a size distribution to be acquired and displayed. In addition, if a metering device is used to

draw a known volume of the particle suspension through the aperture, a count of the number of pulses will yield the concentration of particles in the sample.[74]

The method has been utilized to characterize thousands of different industrial particulate materials: drugs, pigments, fillers, toners, foods, abrasives, explosives, clay, minerals, construction materials, coating materials, metals, filter materials, and many others have all been analyzed by the coulter principle.[75] In fact, the method can be used to measure any particulate material that can be suspended in an electrolyte. Particles can routinely be measured having the size as small as 0.4 µm and as large as 1200 µm in diameter.

We used this technique to measure the particle distribution of our sodium titanate and mixtures of metal and sodium titanate.
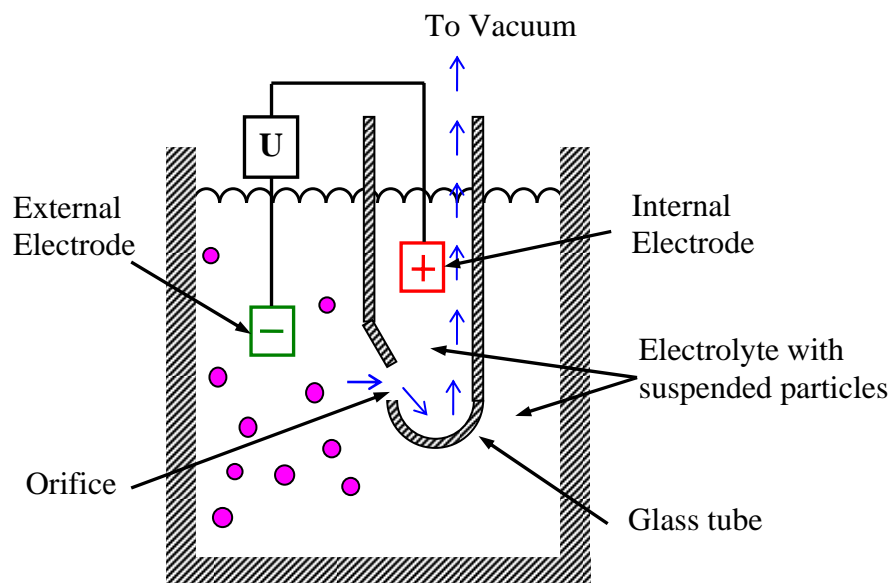
Figure 2.6. Schematic diagram of the Coulter counter.

CHAPTER III

PREPARATION OF MIXED IONIC AND ELECTRONIC ELECTRODES

3.1 Introduction

A key component of achieving high efficiency in an AMTEC device is its cathode. The basic requirements for an AMTEC electrode are having a melting temperature higher than the operating temperature of AMTEC, 1123-1223K, and being stable for a long periods of time at those operating temperatures. The electrode also should be chemically and thermally compatible with other components in the cell, including sodium and BASE. It must not form new phases with other components of the cell which would adversely affect the performance of the cell. Additionally, the electrode should have good electronic conductivity, very low vapor pressure at AMTEC temperatures and capability of high rates of ionic or diffusive transport of sodium.[39]

For mixed ionic and electronic electrodes, the electronic component is generally a metal, which provides a conduction path for electrons, and the ionic component is a ceramic material, which provides the Na^+ transport path. The properties of these two components and their interaction with the BASE determine the performance of the electrode. In this chapter, we first investigated the compatibility of components in the mixed electrode, in which we calculated Gibbs free energy and constructed chemical potential diagrams for different systems. Second, we examined selected pure metal electrodes and their performance, and selected the best metal candidate for a MIEE.

Third, we discussed the preparation of a series of mixed electrodes with different compositions using selected metal with sodium titanate, and measured their performance. Finally, we developed a theoretical model based on percolation theory, which we construct to predict and explain the experimental results and indicate the optimal composition for a MIEE.

3.1.1 Metal Component Selection

In order to meet the requirements of an AMTEC electrode, both physical and chemical properties of prospective metals must be considered, such as coefficient of thermal expansion, vapor pressure, and reactivity.

The coefficient of thermal expansion (CTE) is an important factor for electrode selection. Although the electrode film is very thin, hence not subject to great internal stresses, the CTEs of the electrode and BASE still need to match each other in order for the electrode to remain bonded to the BASE during the AMTEC operation, especially during periods of thermal cycling. Low vapor pressure helps ensure that a sufficient amount of electrode remains after an extended period at high temperature and reduces the chance of contaminating other components in the cell. A low surface-self diffusion coefficient corresponds to slow sintering behavior, helping to maintain a stable physical morphology over the lifetime of the electrode, especially in the reaction area at the three-phase boundary between electrode, electrolyte, and sodium vapor space. Other necessary characteristics of electrode materials include inertness with respect to sodium and BASE and no dissociation at AMTEC operating temperatures.

Table 3.1 lists the properties of all metals with a melting point higher than 1273K, including electrical resistance, thermal expansion coefficient, vapor pressure and surface-self diffusion coefficient, relevant to AMTEC operation.   Na-β"-alumina is included at the bottom of the table for comparison. It is found that iridium and niobium both provide a close match to BASE's thermal expansion, and possess low vapor pressure and surface-self diffusion coefficients, similar to molybdenum's, which has been used as an AMTEC electrode and exhibits adequate sintering behavior. Additionally, iridium also has a low electrical resistance, while niobium provides a higher electrical resistance.   Combining all these properties, iridium offers a good possibility for AMTEC electrode candidates. Niobium may be a good candidate too, though its electrical resistance is not very low. Hafnium, tantalum and zirconium also have similar CTE to BASE, but hafnium possesses a very large electrical resistance. For these reasons, tantalum, iridium and niobium have been examined as electrode materials in this research.

Rhodium, platinum, rhenium, ruthenium and vanadium metals all have low vapor pressure, along with relatively low electrical resistances and surface-self diffusion coefficient, but their CTEs are higher than that of BASE.   These metals might be effective if alloyed with the metal having low CTE, such as tungsten or molybdenum. For the purpose of this research, WRe, WRh, and MoRe alloy electrodes were all tested.

Metals with higher surface-self diffusion or thermal expansion coefficients that don't match the electrolyte are not qualified for AMTEC metal electrodes, but may be suitable in a MIEE electrode with ceramic material. The ceramic component is able to form a

framework to help control the sintering behavior of the metal, and effectively adjust the CTE of the electrode to help reduce thermal stresses. Ni is such a metal, and thus could be a candidate material for the metal component in a MIEE.

In summary, due to low vapor pressure, surface-self diffusion coefficient, similar thermal expansion coefficient to that of BASE and relative low electrical resistance, iridium, niobium and tantalum appear to have potential to conduct good performance in an AMTEC power system. Therefore, the performances of these metals were tested as AMTEC electrode materials in this research. Nickel metal has also been investigated as a MIEE component candidate due to the idea that the two components, metal and ceramic, might restrict each other and possibly result in good performance. Additionally WRe, WRh, and MoRe alloy electrodes appeared promising due to their ability to achieve the desired thermal expansion coefficient and were thus examined as well.

All the preceding discussion of metal electrode selection is only based on their physical properties. According to the AMTEC electrode requirements, the chemical properties of these metals are also needed to examine. The chemical potential diagram will provide this information.

Table 3.1. Physical properties of metals studied in this research, including melting point(T_m), electrical resistivity(R) and coefficient of thermal expansion (CTE) at different temperature, vapor pressure (P_{vap}) at 1273K, and surface-self diffusion coefficient(D_s) at 1273K.

Electrode	T_m(K)[b]	$R(\mu\Omega*cm)$[b]	CTE(10^{-6}/K)[b]	T(K)[a]	P_{vap}(torr)[c]	D_s(cm^2/s)[b,d]
Beryllium(Be)	1560	26	17	973	1.49E-04	
Chromium(Cr)	2133	47	9.4	925	5.72E-06	2.20E-7
Copper(Cu)	1358	8.1	20.3	1250	6.17E-05	1.87E-9
Cobalt(Co)	1767	26.5	14.0	673	8.53E-08	7.98E-13
Hafnium(Hf)	2500	84.4	6.3	673	5.23E-16	
Iridium(Ir)	2720	15.1	7.2	773	3.07E-17	1.00E-9
Iron(Fe)	1809	105.5	14.6	1073	2.11E-06	1.50E-5
Molybdenum(Mo)	2888	31	5.75	1273	4.92E-17	6.90E-10
Nickel(Ni)	1728	45.5	16.3	1173	9.41E-08	5.80E-6
Niobium(Nb)	2740	59.7	7.72	1073	1.57E-19	4.10E-10
Palladium(Pd)	1827	40	13.6	1273	8.80E-07	
Platinum(Pt)	2043	43.1	10.2	1273	1.28E-12	1.40E-7
Rhenium(Re)	3453	4.7	8.5	373	6.63E-22	
Rhodium(Rh)	2239	14.6	9.8	773	1.16E-12	3.00E-9
Ruthenium(Ru)	2583	7.7	9.6	293	2.19E-16	
Tantalum(Ta)	3253	35	6.6	773	1.68E-23	2.70E-8
Thorium(Th)	2028	14	11.2	293	1.50E-15	
Titanium(Ti)	1940	165	9.9	1073	1.05E-09	
Tungsten(W)	3660	33	4.6	1273	2.72E-25	2.30E-13
Vanadium(V)	2175		10.4	1173	4.02E-11	
Zirconium(Zr)	2125	44	5.9	293	4.84E-15	
Na-β''-Al$_2$O$_3$	2253		8.6	1273		

[a] Both electrical resistance and CTE are given at this temperature.

[b] From Ref. 76.

[c] From Ref. 77.

[d.] From Ref 78.

3.1.2 Chemical Potential Diagram

Before using metal and sodium titanate to make the mixed electrode, we must examine if they could co-exist and be stable at AMTEC operating temperatures. At AMTEC temperatures, molecules have high kinetic energy and are able to diffuse rapidly or react with each other. This diffusion and reaction could dramatically degrade electrode performance. The chemical stability of the electrode is quite important for obtaining good performance of high temperature electrochemical cells.

If chemical reactions occur between the electrolyte and electrode in high temperature electrochemical cells under operating conditions, the product phase(s) would be very difficult to identify it in situ. Although microstructure and composition identification could be examined after the operation, the product phase(s) could be stable only at operating temperatures. So the post-test examination might not give us enough information to understand the behavior of the electrode during the operation. Chemical potential diagrams have been proposed as a thermodynamic way of examining the thermodynamic stability of electrode-electrolyte interfaces.

For high temperature electrochemical cells, when the chemical potential relations among the species across interfaces deviates from equilibrium, the difference provides the driving forces for formation of new phases. When there arises a chemical potential gradient, this provides the driving force for chemical diffusion. Thus, chemical potential diagrams can demonstrate the following information:

1. Chemical phases present in the system. The chemical potential diagram consists of stability polygons for compounds, which illustrates the stable phases under experimental conditions.

2. Reactions possibly occurring between electrode and electrolyte as a function of polarization. Usually, polarization of electrochemical cells can be related to a change in chemical potential of a particular species associated with ionic carriers in the electrolyte. Therefore, an appropriate chemical potential diagram can illustrate the effect of polarization on chemical stability of the interface.

3. Reaction products arrangement or reaction steps. When reactions actually occur at interfaces, there arise chemical potential gradients across the interface. If a reaction proceeds slowly enough to be followed by diffusion of elements involved, reaction products can be arranged so as to give gradual changes of chemical potentials, which shows in chemical potential diagram.

Therefore, the use of chemical potential diagrams provides a powerful basis of applying thermodynamic considerations to practical materials problems.

3.2 Experimental

3.2.1 Electrode Preparation

Pure metal electrodes, such as Ta, Nb, Ir, WRh, WRe and MoRe were sputtered in our lab using the Hummer 8 turbo sputtering system (Anatech, Ltd). Ni electrodes were fabricated by evaporation in Southwest Impreglon, Houston.

Sodium titanate powder was purchased from Strem chemicals Inc., with a particle size as large as $37\mu m$. To improve MIEE performance, these powders were milled in ethanol solution by steel balls of different size for a few days, followed by drying and grinding. These milled sodium titanate powders were mixed with pure metal powders at calculated mass ratios by ball-milling for a day, then dried and ground again. The particle size distribution was measured by a Coulter Multisizer in Mechanical Engineering Department, TAMU. The mixed powders were deposited on the β''-alumina tube outside wall by flame spray at Hitemco Inc or Alamo Supply, in Houston, Texes.

3.2.2 Setup and Measurement

The SETC was set up as described in Chapter II. Each sample consists of a cylindrical β''-alumina tube with 4 electrode bands, approximately 0.25cm wide, deposited on the outer surface of BASE and separated by 0.25cm spaces and covered by Ni metal mesh or Cu mesh as the current collector. Ni or Cu leads are used to tie these current collector on to the β''-alumina tube and threaded through α-alumina rods to out of the manifold, shown in Figure 3.1.

Electrochemical impedance measurements were performed using a Solartron 1250 Frequency Analyzer and a Solartron 1287 Electrochemical Interface in the frequency range between 10^5Hz and 0.1Hz. A small amplitude (10mv) sinusoidal wave output was superimposed on the applied dc potential. Impedance was measured every day for each electrode to record their performance over time, but the overall experiment running time can differ based on sample performance and other factors. The electrode temperature was around 850^oC and the pool temperature was 290^oC. The SETCs had fluctuations in temperature control, such that these temperatures varied in the range of 840-860°C and 280-305°C.

The microstructures of electrodes before and after testing in the SETC were observed by a microprobe in the Geology and Geophysics department, TAMU. This electron microprobe is a four-spectrometer Cameca SX50 equipped with a PGT energy dispersive system and a dedicated Sun workstation.
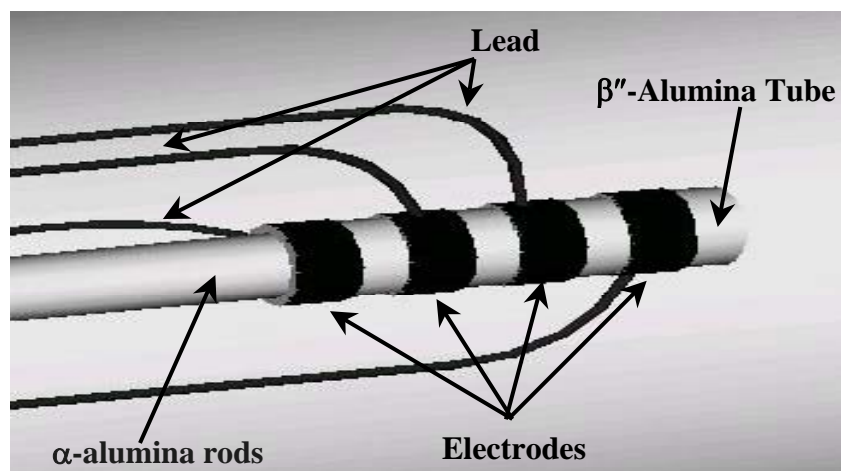
Figure 3.1. Schematic diagram of SETC electrodes.

3.3 Results and Discussion

3.3.1 Calculation of Chemical Potential Diagrams

The chemical potential diagrams are plotted based on the calculation of Gibbs free energy of reactions and equilibrium partial pressure of oxygen. The detailed calculations are displayed in appendix A.

Chemical Potential Diagram for the Na-Al-O System at 1100K. —— For the Na-Al-O system, all possible reactions and calculated equilibrium partial pressure of oxygen for each reaction are listed in Table 3.2. The thermodynamic properties of β- and β''- alumina have been measured by several authors[79-81] and reviewed recently by Barsoum.[82] Although the thermodynamic properties of β-alumina ($Na_2Al_{22}O_{34}$) have been well established, those of β''- alumina ($NaAl_5O_8$) have not been clarified yet. The thermodynamic data of β-and β''-alumina adopted in this calculation are from Barsoum's evaluation and Itoh's measurements[80] respectively.

Figure 3.2(a) shows the chemical potential diagram for the Na-Al-O system at 1100K. This diagram shows that β''-alumina is thermodynamically stable at this temperature but its stability region is very narrow. Therefore β''-alumina is easy to convert to its neighbors $NaAlO_2$ and $Na_2Al_{22}O_{34}$. Additionally, with the temperature increase, the stability region of β''-alumina will become narrower and finally become a line at some temperature, which means β''-alumina is not a stable phase at that temperature and decomposes into $NaAlO_2$ and $Na_2Al_{22}O_{34}$. This is in agreement with the experimental results of Barsoum, who found that at low temperatures, β''-alumina is thermodynamically stable, while at high temperatures (around 1773K), and this phase

decomposes into β- alumina and NaAlO$_2$. Thus, chemical potential diagram provides theoretical evidence for BASE degradation in AMTEC.

The equilibrium oxygen partial pressure over β″-alumina is a function of the sodium partial pressure. The slope of stability range of β″-alumina is –4, which means that a slight change in the sodium partial pressure gives rise to a drastic change in the equilibrium oxygen pressure. In AMTEC, the vapor pressure of sodium ranges from 1 to 10^{-5} atm.[38, 44,83] Figure 3.2(a) indicates that to keep β″-alumina within its stability field, the oxygen partial pressure should be maintained at low levels ($P_{O_2} < 10^{-28}$ atm) depending on the sodium partial pressure.

Chemical Potential Diagram for the Na-Ti-O Systems at 1100K.— For the Na-Ti-O system, well-defined thermodynamic data are not available. There are only a few literature sources concerning this system and they differ from each other. In this research, these thermodynamic data were assessed before calculation, and then the most reasonable ones were adopted, but no experimental measurements were done in our lab. Therefore, the chemical potential diagram of the Na-Ti-O system, shown in Figure 3.2(b), may not be as accurate as the Na-Al-O system. All reactions and their equilibrium partial pressure of oxygen are listed in Table 3.3.

It is found that Na$_2$Ti$_2$O$_5$ is not present in this diagram, although it reacts with sodium or other compounds and is listed in Table 3.3. This means this compound is not stable at this temperature in our system. Although it could be formed at this temperature, it will convert to other sodium titanates, which is in agreement with the results of Eriksson and Pelton.[84] They assessed the Na$_2$O-TiO$_2$ phase diagram, and

found that there is not $Na_2Ti_2O_5$ compound present in it. This agreement indicates that our calculation is valid. Figure 3.2(b) shows that $Na_2Ti_3O_7$, $Na_2Ti_6O_{13}$ and TiO_2 are stable at AMTEC condition, depending on the real oxygen partial pressure.

Table 3.2. Equilibrium partial pressure of oxygen (P_{O_2}) of reactions in the Na-Al-O system at 1100K.

Reaction	Partial Pressure of Oxygen (atm)
$2Al(l)+ 3/2O_2(g)\rightarrow \alpha\text{-}Al_2O_3(s)$	$\log P_{O_2} = -42.04$
$2Al(l)+ 3/2O_2(g)\rightarrow \gamma\text{-}Al_2O_3(s)$	$\log P_{O_2} = -41.59$
$2Na(g) + 1/2O_2(g)\rightarrow Na_2O(s)$	$\log P_{O_2} = -26.49 - 4\lg P_{Na}$
$Na(g) +Al(l) + O_2(g)\rightarrow NaAlO_2(s)$	$\log P_{O_2} = -42.56 - \lg P_{Na}$
$Na(g) +5Al(l) + 4O_2(g)\rightarrow NaAl_5O_8(s)^a$	$\log P_{O_2} = -42.11 - \frac{1}{4}\lg P_{Na}$
$2Na(g) +22Al(l) + 17O_2(g)\rightarrow Na_2Al_{22}O_{34}(s)^b$	$\log P_{O_2} = -42.01 - \frac{2}{17}\lg P_{Na}$
$4Na(g) + NaAl_5O_8(s) + O_2(g)\rightarrow 5NaAlO_2(s)$	$\log P_{O_2} = -44.34 - 4\lg P_{Na}$
$12Na(g) + 5Na_2Al_{22}O_{34}(s) +3O_2(g)\rightarrow 22NaAl_5O_8(s)$	$\log P_{O_2} = -45.18 - 4\lg P_{Na}$
$20Na(g) + Na_2Al_{22}O_{34}(s) + 5O_2(g)\rightarrow 22NaAlO_2(s)$	$\log P_{O_2} = -44.93 - 4\lg P_{Na}$
$2Na(g) + Al_2O_3(s) + 1/2O_2(g)\rightarrow 2NaAlO_2(s)$	$\log P_{O_2} = -45.47 - 4\lg P_{Na}$
$2Na(g) +5Al_2O_3(s) + 1/2O_2(g)\rightarrow 2NaAl_5O_8(s)$	$\log P_{O_2} = -49.98 - 4\lg P_{Na}$
$2Na(g) +11Al_2O_3(s) + 1/2O_2(g)\rightarrow Na_2Al_{22}O_{34}(s)$	$\log P_{O_2} = -55.77 - 4\lg P_{Na}$

[a].From Ref. 80
[b].From Ref. 82

Table 3.3. Equilibrium partial pressure of oxygen (P_{O_2}) of reactions in the Na-Ti-O system at 1100K.

Reaction	Partial Pressure of Oxygen (atm)
$Ti(s)+ O_2(g) \rightarrow TiO_2(s)$	$\log P_{O_2} = -35.36$
$2Na(g) + 1/2O_2(g) \rightarrow Na_2O(s)$	$\log P_{O_2} = -26.49 - 4\lg P_{Na}$
$2Na(g) + Ti(s) + 3/2O_2(g) \rightarrow Na_2TiO_3(s)$	$\log P_{O_2} = -39.11 - \frac{4}{3}\lg P_{Na}$
$2Na(g) + 2Ti(s) + 5/2O_2(g) \rightarrow Na_2Ti_2O_5(s)$	$\log P_{O_2} = -37.90 - \frac{4}{5}\lg P_{Na}$
$2Na(g) + 3Ti(s) + 7/2O_2(g) \rightarrow Na_2Ti_3O_7(s)$	$\log P_{O_2} = -37.44 - \frac{4}{7}\lg P_{Na}$
$2Na(g) + 6Ti(s) + 13/2O_2(g) \rightarrow Na_2Ti_6O_{13}(s)$	$\log P_{O_2} = -36.54 - \frac{4}{13}\lg P_{Na}$
$2Na(g) + Na_2Ti_2O_5(s) + 1/2O_2(g) \rightarrow 2Na_2TiO_3(s)$	$\log P_{O_2} = -45.22 - 4\lg P_{Na}$
$2Na(g) + 2Na_2Ti_3O_7(s) + 1/2O_2(g) \rightarrow 3Na_2Ti_2O_5(s)$	$\log P_{O_2} = -44.36 - 4\lg P_{Na}$
$4Na(g) + Na_2Ti_3O_7(s) + O_2(g) \rightarrow 3Na_2TiO_3(s)$	$\log P_{O_2} = -44.96 - 4\lg P_{Na}$
$2Na(g) + Na_2Ti_6O_{13}(s) + 1/2O_2(g) \rightarrow 2Na_2Ti_3O_7(s)$	$\log P_{O_2} = -48.07 - 4\lg P_{Na}$
$4Na(g) + Na_2Ti_6O_{13}(s) + O_2(g) \rightarrow 3Na_2Ti_2O_5(s)$	$\log P_{O_2} = -46.71 - 4\lg P_{Na}$
$10Na(g) + Na_2Ti_6O_{13}(s) + 5/2O_2(g) \rightarrow 6Na_2TiO_3(s)$	$\log P_{O_2} = -45.78 - 4\lg P_{Na}$
$2Na(g) + TiO_2(s) + 1/2O_2(g) \rightarrow Na_2TiO_3(s)$	$\log P_{O_2} = -46.58 - 4\lg P_{Na}$
$2Na(g) + 2TiO_2(s) + 1/2O_2(g) \rightarrow Na_2Ti_2O_5(s)$	$\log P_{O_2} = -48.06 - 4\lg P_{Na}$
$2Na(g) + 3TiO_2(s) + 1/2O_2(g) \rightarrow Na_2Ti_3O_7(s)$	$\log P_{O_2} = -49.50 - 4\lg P_{Na}$
$2Na(g) + 6TiO_2(s) + 1/2O_2(g) \rightarrow Na_2Ti_6O_{13}(s)$	$\log P_{O_2} = -50.70 - 4\lg P_{Na}$
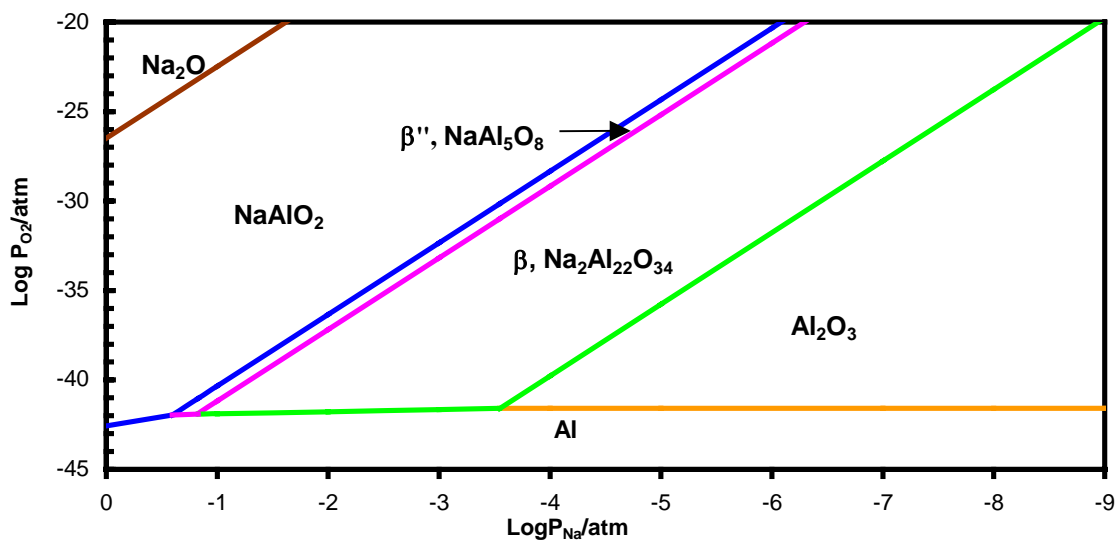
(a) Chemical Potential Diagram for the Na-Al-O system at 1100K.
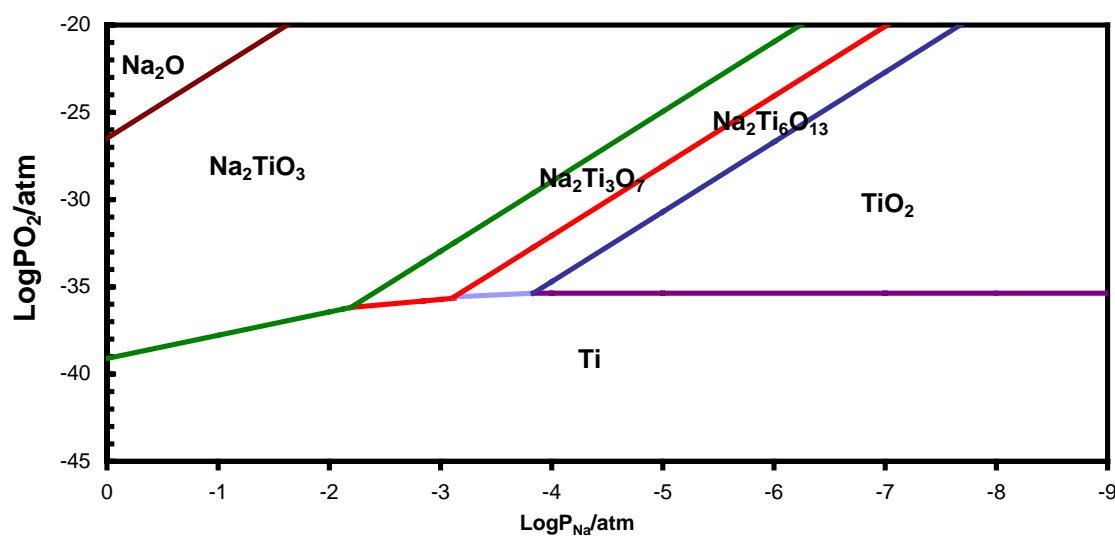
(b) Chemical Potential Diagram for the Na-Ti-O system at 1100K.

Figure 3.2. Chemical potential diagrams for (a) the Na-Al-O system. (b) the Na-Ti-O system at 1100K.

Chemical Potential Diagram for the Na-Ti-Al-O Systems at 1100K. — For the Na-Ti-Al-O system, there may be some quaternary oxides present, such as $NaAl_5Ti_2O_{12}$ and $Na_2Al_2Ti_6O_{16}$, but thermodynamic data are not available for these compounds. If these compounds do exist, they generally could be synthesized by solid oxide reactions at elevated temperature. We assume that these two compounds just start being formed at 1100K, which in fact is too low temperature for ceramic oxide formation. Based on this assumption, we estimated the minimum Gibbs free energy of formation for these two compounds at 1100K, listed in Table 3.4.

When chemical potential diagrams of the Na-Al-O and the Na-Ti-O systems are superimposed in Figure 3.3, some compounds coexist at some regions and they could react each other. These reactions are listed in Table 3.4. Calculation of the Gibbs free energy of reaction for all these reactions (see calculation in Appendix A) shows that all ΔG_{rxn} are greater than 0, which means these reactions are unlikely to occur in our system. Therefore, at each point in Figure 3.3, one compound in the Na-Al-O system and another compound in the Na-Ti-O system are in equilibrium with each other, except in the low sodium pressure region, in which TiO_2 and Al_2O_3 are present. When these two systems overlap, TiO_2 and Al_2O_3 could react with each other and form Al_2TiO_5, $Al_2Ti_7O_{15}$ or $Al_3Ti_5O_2$ compounds. Because this region is far away from our experimental conditions, thus, any change would not affect our experimental results. Additionally, there are no thermodynamic data available for these compounds.

Figure.3.3 illustrates that the stability region of $Na_2Ti_6O_{13}$ is far from that of β''-alumina, suggesting the decomposition of $Na_2Ti_6O_{13}$ is thermodynamically favored

during operation. Furthermore, if the decomposition reaction rate is high enough at experiment temperature, $Na_2Ti_6O_{13}$ will not be present. Figure 3.3 also shows that the stability region of $Na_2Ti_3O_7$ is overlapped with β''-alumina stability region. In the overlap section, $Na_2Ti_3O_7$ is stable with β''-alumina; while in the left section, $Na_2Ti_3O_7$ thermodynamically converses to Na_2TiO_3. However, because the equilibrium line between $Na_2Ti_3O_7$ and Na_2TiO_3 is so close to the line of $NaAlO_2$ and β''-alumina, the driving force of $Na_2Ti_3O_7$ conversion is very small. Therefore, it is believed that $Na_2Ti_3O_7$ is basically stable with β''-alumina at our experimental conditions.

It was reported that the Na_2MoO_4 treated Mo electrodes exhibit high electrode activity, due to the high Na^+ conductivity of Na_2MoO_4. Unfortunately, sodium molybdenum oxides can not thermodynamically be in equilibrium with a Mo/BASE interface, which results in the degradation of the electrochemical activity.[85] Figure 3.3 illustrates that sodium titanate is thermodynamically favored to be stable with BASE, which confirms that $Na_2Ti_3O_7$ sodium titanate is a promising candidate of MIEE for AMTEC.
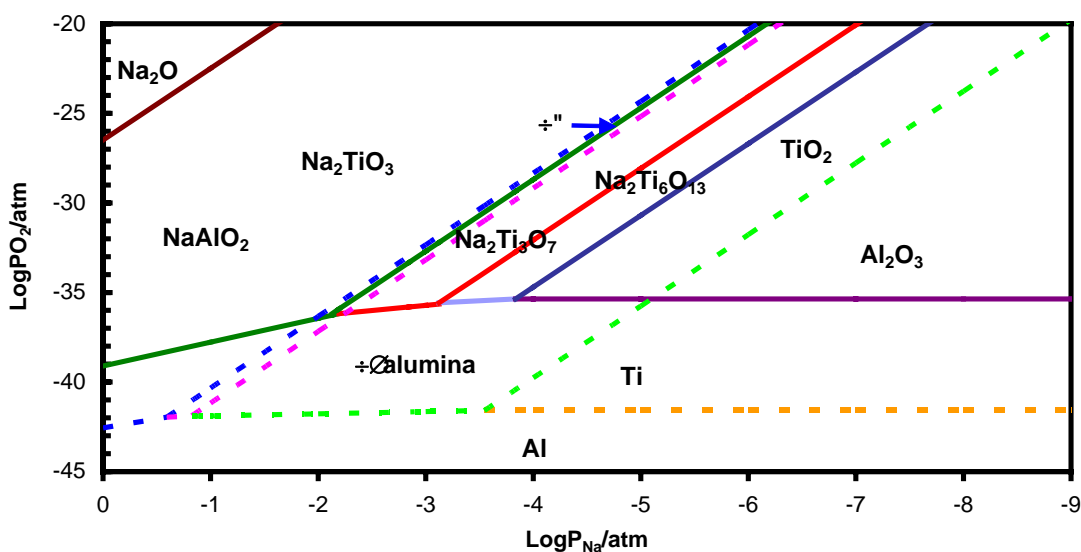
Figure 3.3. Chemical potential diagrams for the Na-Al-Ti-O system at 1100K.

Table 3.4. Minimum Gibbs free energy changes (ΔG_{rxn}) of reactions in the Ni-Ti-Al-O system at 1100K.

Reaction	ΔG_{rxn} (kJ)
$2Na(g)+2Al(s)+6Ti(s)+8O_2(g)\rightarrow Na_2Al_2Ti_6O_{16}(s)$	-6050[a]
$Na(g)+5Al(s)+2Ti(s)+6O_2(g)\rightarrow NaAl_5Ti_2O_{12}(s)$	-4908.18[a]
$5NaAlO_2(s)+2Na_2TiO_3(s)\rightarrow NaAl_5Ti_2O_{12}(s)+8Na(g)+2O_2(g)$	172
$2NaAlO_2(s)+6Na_2TiO_3(s)\rightarrow Na_2Al_2Ti_6O_{16}(s)+12Na(g)+3O_2(g)$	344
$22Na_2Ti_3O_7(s)+Na_2Al_{22}O_{34}(s)\rightarrow 11Na_2Al_2Ti_6O_{16}(s)+24Na(g)+6O_2(g)$	3001
$11Na_2Ti_6O_{13}(s)+Na_2Al_{22}O_{34}(s)\rightarrow 11Na_2Al_2Ti_6O_{16}(s)+2Na(g)+1/2O_2(g)$	2858
$44/3Na_2Ti_3O_7(s)+5Na_2Al_{22}O_{34}(s)\rightarrow 22Na_2Al_2Ti_6O_{16}(s)+52/3Na(g)+13/3O_2(g)$	3184
$22/3Na_2Ti_6O_{13}(s)+5Na_2Al_{22}O_{34}(s)\rightarrow 22NaAl_5Ti_2O_{12}(s)+8/3Na(g)+2/3O_2(g)$	3069

[a] This is the standard Gibbs Free Energy of formation.

Metal Stability at 1100K. ── From Figure 3.2(a) and 3.2(b), it is found that Al and Ti cannot be used as AMTEC electrodes thermodynamically, because these metal stability requires a very low level of oxygen pressure so that they are easily oxidized at AMTEC conditions. We calculated the equilibrium oxygen partial pressure for oxides of metal candidates at our experimental conditions, listed in Table 3.5.

It is found that Ni metal is stable with oxygen partial pressures lower than 10^{-14}atm, and Cu stable at oxygen partial pressures lower than 10^{-9}atm, which means they are stable as pure metals at AMTEC conditions. The same situation is also for metal Ir and Co. Therefore, these four metals can be used as AMTEC electrodes. Zirconium has been discussed above and could be a candidate, since it has a similar CTE with BASE, but the thermodynamic calculation shows that it requires very low equilibrium partial pressures of oxygen. Therefore, thermodynamics favorites it present as an oxide at AMTEC operation conditions.

The equilibrium lines between Nb and its oxides are just in the AMTEC condition, where oxygen partial pressures are close to 10^{-28}atm. Nb and its oxides both could be stable in AMTEC condition, depending on the real oxygen pressure in the system. The similar situations are for Ta and Ta_2O_5 and V and its oxides. Therefore, Nb, Ta and V could be used in AMTEC, though there are concerns about oxide formation.

All these discussions are based on the thermodynamic calculations. In fact, kinetics also determines whether a reaction occurs or not. If the reaction rate is very slow, this reaction can be considered as not occurring, although thermodynamically favored to occur.

Table 3.5. Equilibrium partial pressure of oxygen (P_{O_2}) of metal oxides at 1100K.

Reaction	Partial Pressure of Oxygen (atm)
$Cu(s) + 1/2O_2(g) \rightarrow CuO(s)$	$\log P_{O_2} = -5.51$
$2Cu(s) + 1/2O_2(g) \rightarrow Cu_2O(s)$	$\log P_{O_2} = -8.39$
$3Co(s) + 2O_2(g) \rightarrow Co_3O_4(s)$	$\log P_{O_2} = -11.6$
$Co(s) + 1/2O_2(g) \rightarrow CoO(s)$	$\log P_{O_2} = -14.8$
$Ir(s) + O_2(g) \rightarrow IrO_2(s)$	$\log P_{O_2} = -2.4$
$Ni(s) + 1/2O_2(g) \rightarrow NiO(s)$	$\log P_{O_2} = -13.35$
$Nb(s) + 1/2O_2(g) \rightarrow NbO(s)$	$\log P_{O_2} = -30.4$
$Nb(s) + O_2(g) \rightarrow NbO_2(s)$	$\log P_{O_2} = -28.3$
$2Nb(s) + 5/2O_2(g) \rightarrow Nb_2O_5(s)$	$\log P_{O_2} = -26.97$
$Ta(s) + O_2(g) \rightarrow TaO_2(s)$	$\log P_{O_2} = -11.05$
$2Ta(s) + 5/2O_2(g) \rightarrow Ta_2O_5(s)$	$\log P_{O_2} = -29.7$
$V(s) + 3/2O_2(g) \rightarrow V_2O_3(s)$	$\log P_{O_2} = -29.7$
$V(s) + 2O_2(g) \rightarrow V_2O_4(s)$	$\log P_{O_2} = -25.2$
$Zr(s) + O_2(g) \rightarrow ZrO_2(s)$	$\log P_{O_2} = -42.2$

3.3.2 Pure Metal Electrodes

Ta, Ni, Nb, Ir, W and MoRe metal electrodes were examined in this research and some of their Nyquist plots are shown in Figure 3.4, which are typical impedance spectra for porous metal electrodes.[86] The impedance spectra are very similar for all measured metal electrodes, and are composed of two characteristic semi-circular curves with two real axis intercepts and a short inductive tail at high frequency. From AMTEC electrochemical theory,[87] the difference between the high and low frequency intercepts can be interpreted as the apparent charge transfer resistance, R_{act}, of the electrode, which is a resistance including both charge transfer and sodium transport effects. The high frequency intercept value is interpreted as the series resistance R_s, including lead resistance, contact resistances of the leads to the current collector and the current collector to the metal film, and part of the uncompensated BASE resistance. The tail at high frequency is an inductance, caused by the ringlike nature of the contact wire and electrode film around the BASE tube. Figure 3.4 shows that all tested metals have similar impedance spectra, but the values of R_s and R_{act} are different, which means that these metals performed differently.

For the same metal electrode, the impedance spectra also varied with time, generally showing increasing R_s and R_{act}. Figure 3.5 shows the impedance change with time for a Ta electrode. It is found that R_s and R_{act} both increase with time. For comparison, we plotted graphs of R_s and R_{act} vs. experiment time for all measured electrodes, shown in Figure 3.6 (a) and (b) respectively.
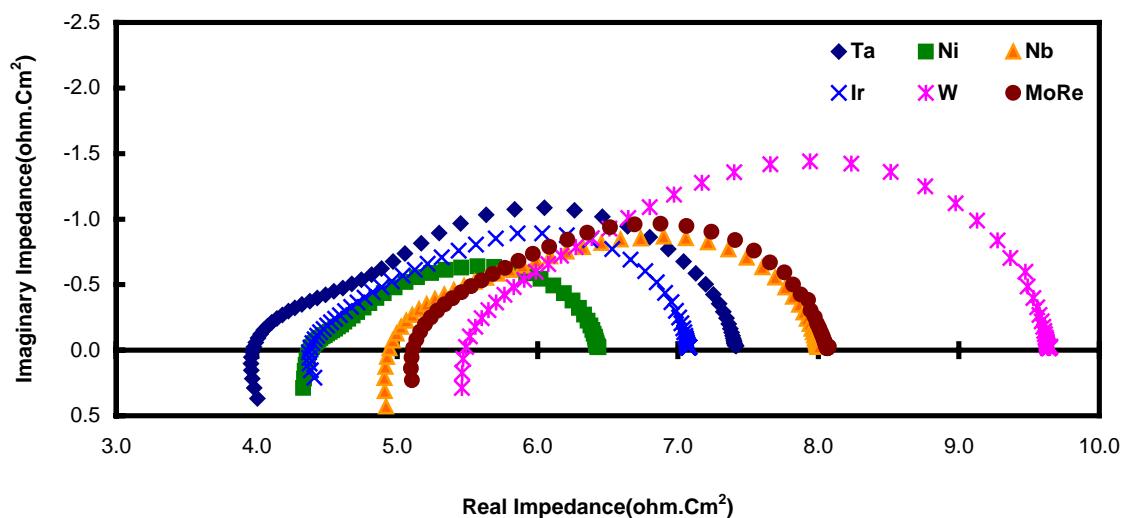
Figure 3.4. Impedance spectra for different tested metal electrodes, at 850°C electrode temperature and 285°C pool temperature.
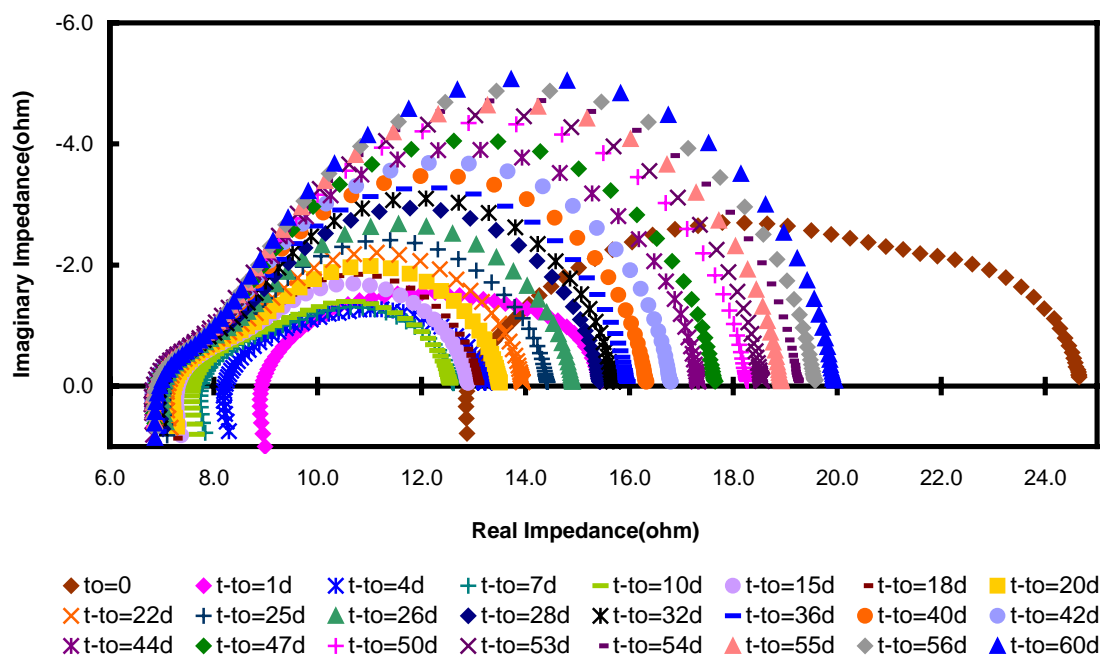
Figure 3.5. Impedance spectra change with experiment time for a Ta electrode.
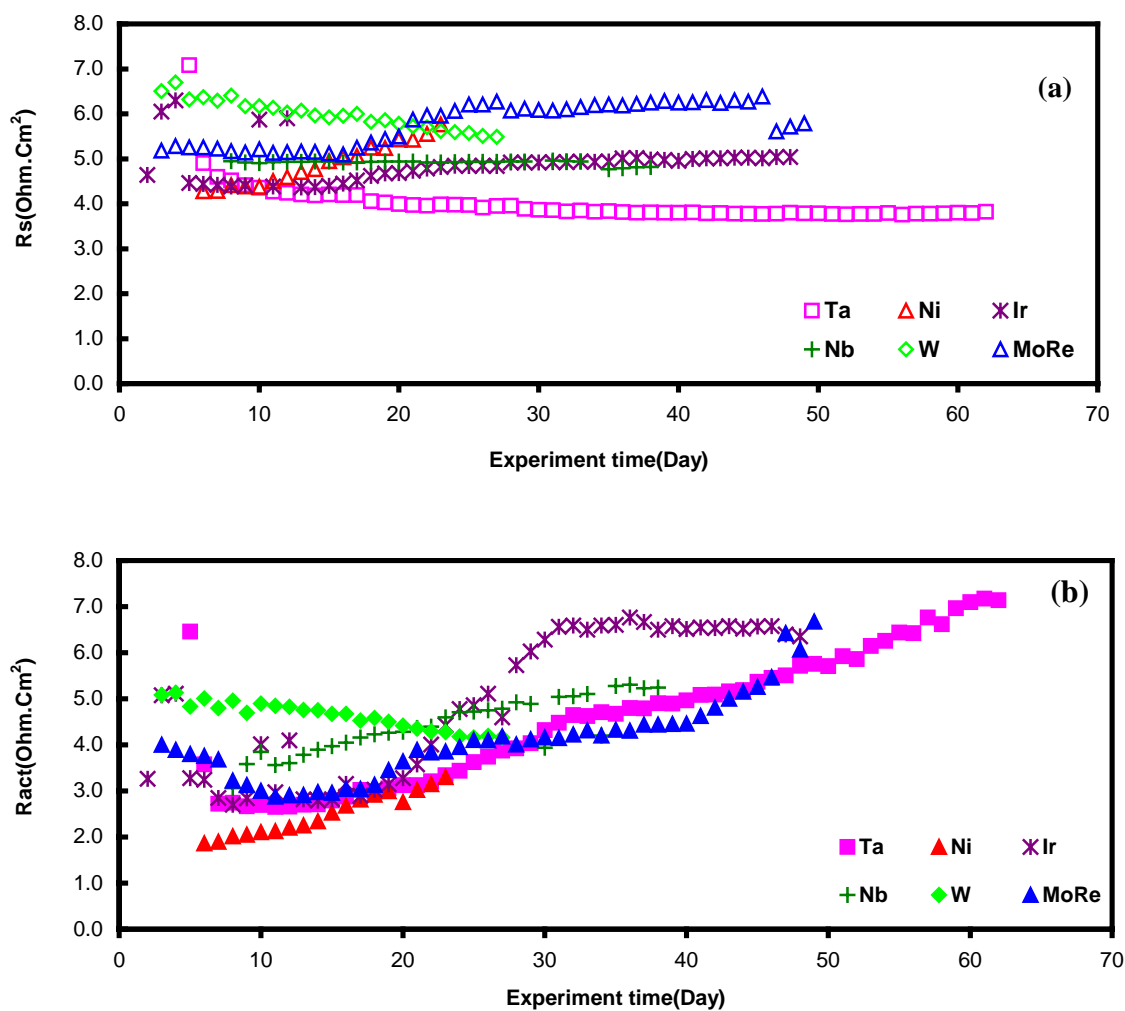
Figure 3.6. a) Series resistance R_s and b) apparent charge transfer resistance R_{act} change with experiment time for tested metal electrodes.

Basically, R_s doesn't vary too much with experiment time for most tested metal electrodes, such as Ta, Nb, Ir and W. It fluctuated slightly with time at the beginning of the experiment, which could be the period of electrode maturity, and then it remained constant. The MoRe electrode has a R_s of about 5.2 ohm·cm^2 at the beginning, and then

after running 16 days, R_s increased with time sharply and finally stabilized at 6.3 ohm·cm^2. This jump of R_s value may be due to the electrode film debonding from the current collector, which increases the contact resistance between the current collector and the electrode film. The Ni electrode is an exception, because its R_s increased almost linearly by 50% in 20 days. Ni metal has a larger thermal expansion coefficient (16.3×10^{-6} K^{-1}), substantially greater than those of BASE(8.6×10^{-6} K^{-1}), as discussed in section 3.1. Such a large difference in thermal expansion coefficient could produce insufficient contact between electrode film and BASE at high temperature. Figure 3.6(b) illustrates R_{act} changes with time. It is found that R_{act} increased with operating time rapidly for most of the metal electrodes, except W. WRe electrodes were also tested, but performed very poorly; R_{act} was as large as a few hundred, and is not listed in Figure 3.4 and 3.6.

Summarizing tested metal electrodes, it was found that Ir, Nb and Ta did not perform as well as expected. Significant agglomeration of grains occurred after 14 days running in SETCs for these three electrodes, as seen in SEM images in Figure 3.7. The extent of grain growth is consistent with the sample's surface-self diffusion coefficients listed in Table 3.1. For example, Ta has the largest surface-self diffusion coefficient of 2.70×10^{-8} cm^2/s at 1273K, and its grains became very large after running, while for the Ir sample with surface-self diffusion coefficients of 1.00×10^{-9} cm^2/s, the grain boundary still can be seen. At high temperature, metal grain coalescence occurred in the electrode film, which resulted in a decrease in the total number of grains and total triple phase reaction area and then led R_{act} to increase. At the same time, the big grains can block Na gas diffusion from the reaction site, which also cause R_{act} increase. These origins of electrode

degradation determine the lifetime of an AMTEC electrode. For W electrodes, R_{act} decreased slightly with time. The reason could be the better contact between W and the BASE, which results in the triple phase reaction area increasing with time. Because W has a very small vapor pressure and self-diffusion coefficient in AMTEC temperature, W particles have very slow grain growth.

The Ni sample was run for only 20 days in this test, but compared to the other tested samples, it exhibited the best performance at the beginning, with the lowest R_s and R_{act}, although these two parameters both increased with time of operation. Since Ni has somewhat larger thermal expansion and diffusion coefficients, grain growth and electrode delamination occurred in this sample, as shown in Figure 3.7, explaining that R_s and R_{act} increased with time. Therefore, Ni itself is not a good candidate for AMTEC, which requires R_{act} and R_s and their degradation with time to be as small as possible. However, a mixed Ni/sodium titanate electrode might retain its initial good performance for a long time.

Sodium titantate may provide a means of controlling the sintering behavior of metals and maintain the porosity of the electrode by forming a ceramic formwork, which would reduce the increase of R_s and R_{act} with time and keep the best performance for a long time. Additionally, based on the metal stability calculation, it is known that Ni is very stable in any AMTEC condition. It should not be oxidized to form volatile Na_xNiO_y compounds with sodium at the AMTEC operating temperature, as occurs in Mo electrodes. Therefore, Ni is selected as component with sodium titanate to make the mixed electrode in this study.
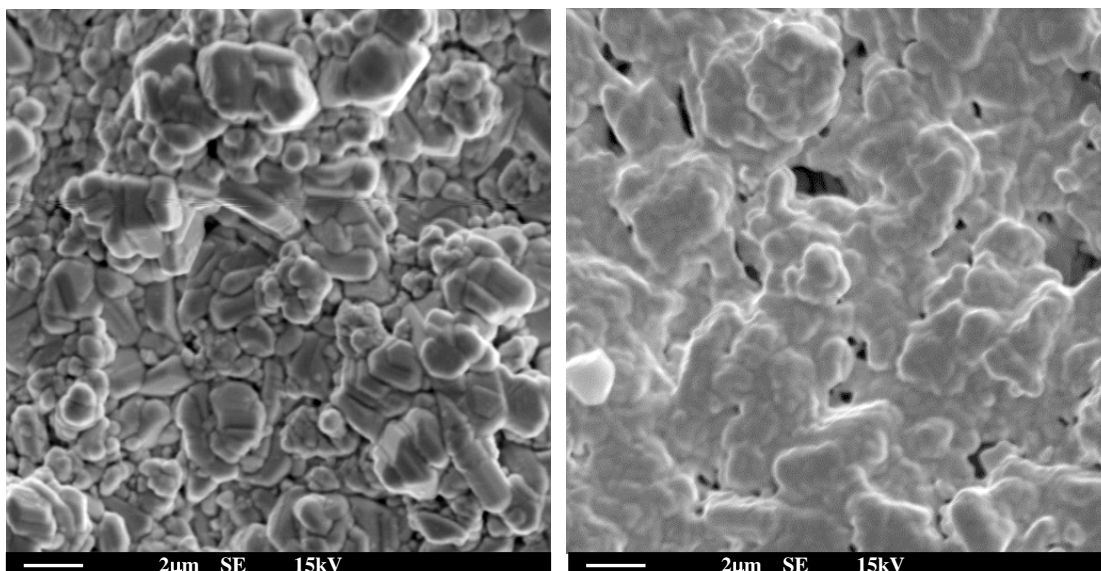
Pre-test Ir sample ×5000 SE image

Post-test Ir sample×5000 SE image
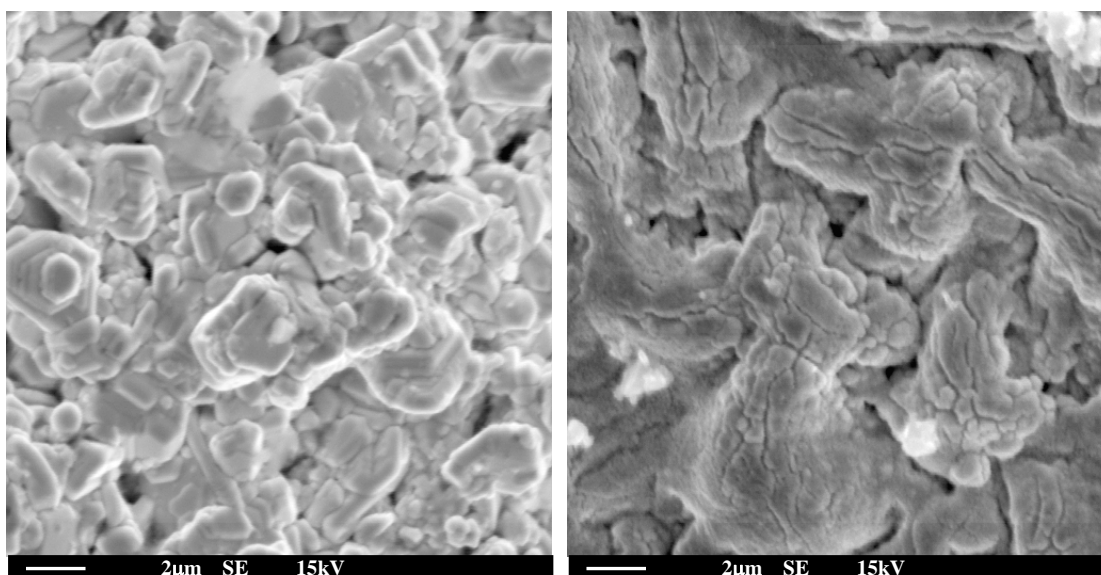
Pre-rest Ta sample ×5000 SE image

Post-test Ta sample ×5000 SE image

Figure 3.7. Scanning electron microscope images for Ir, Ta, Nb and Ni electrodes.
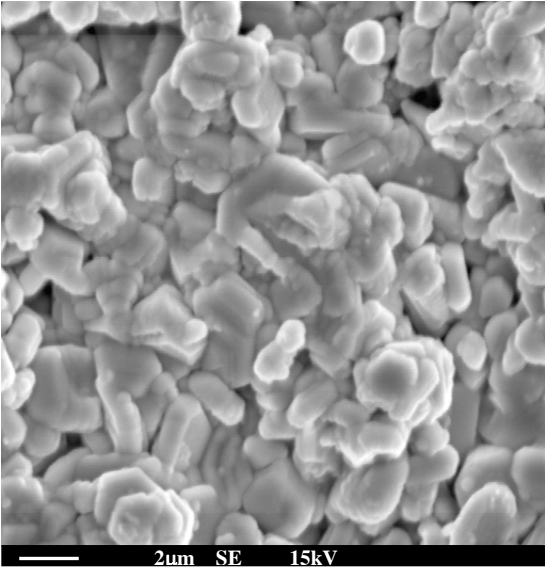
Pre-test Nb sample ×5000SE image
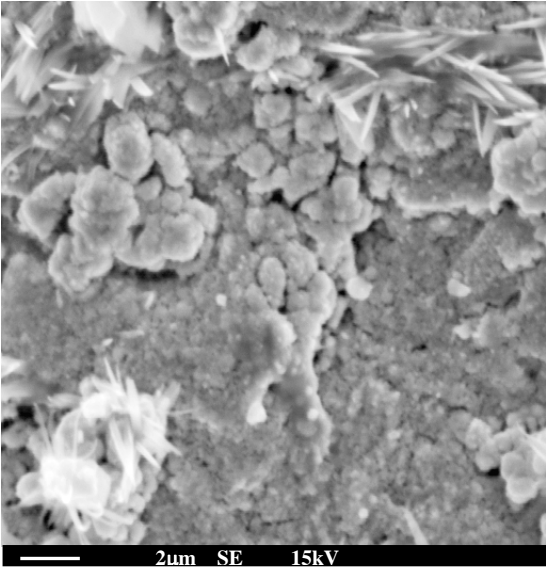
Post-test Nb sample ×5000 SE image
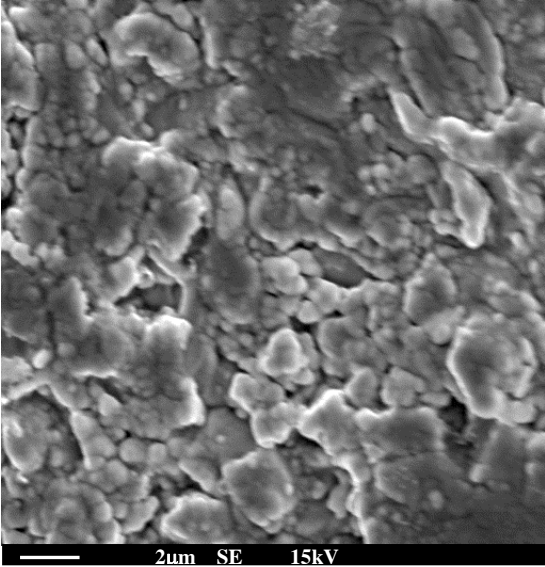
Pre-test Ni sample × 5000 SE image
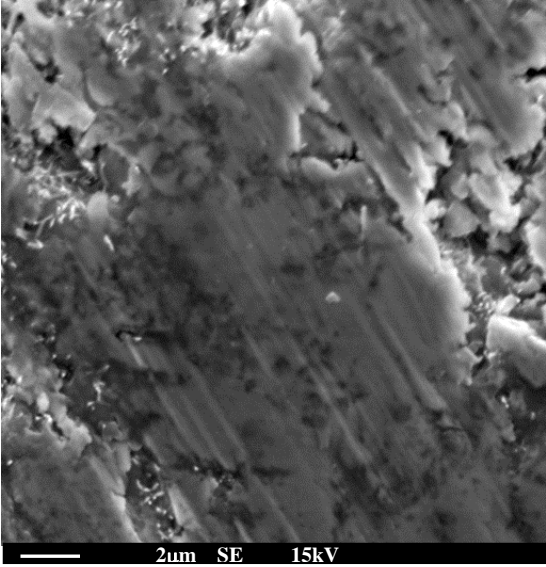
Post test Ni sample ×5000 SE image

Figure 3.7. (Continued)

3.3.3 Mixed Ionic and Electronic Conducting Electrodes

We tested Ni/sodium titanate electrodes with the Ni/sodium mass ratios of 2:1, 3:1, and 4:1, labeled as N21, N31 and N41 electrode respectively. Their impedance spectra are shown in Figure 3.8. N41electrode displayed the smallest impedance and performed best, followed by N21 electrode and the worse one is N21 electrode. Figure 3.9(a) and (b) are the plots of R_s and R_{act} changes with experiment time for these mixed electrodes and pure Ni electrodes for comparison. N31 and N41 electrodes had the very stable performance; their R_s and R_{act} change slightly over 45 days, satisfying our goal of AMTEC electrodes running over 1000 hours without degradation.
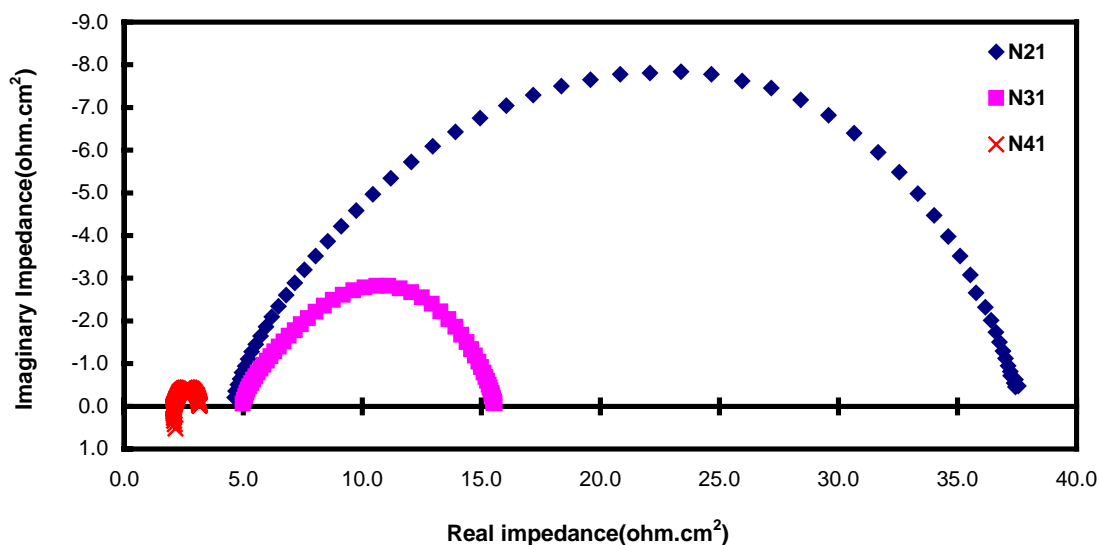
Figure 3.8. Impedance spectra of Ni/sodium titanate electrodes with different Ni/sodium titanate mass ratios.
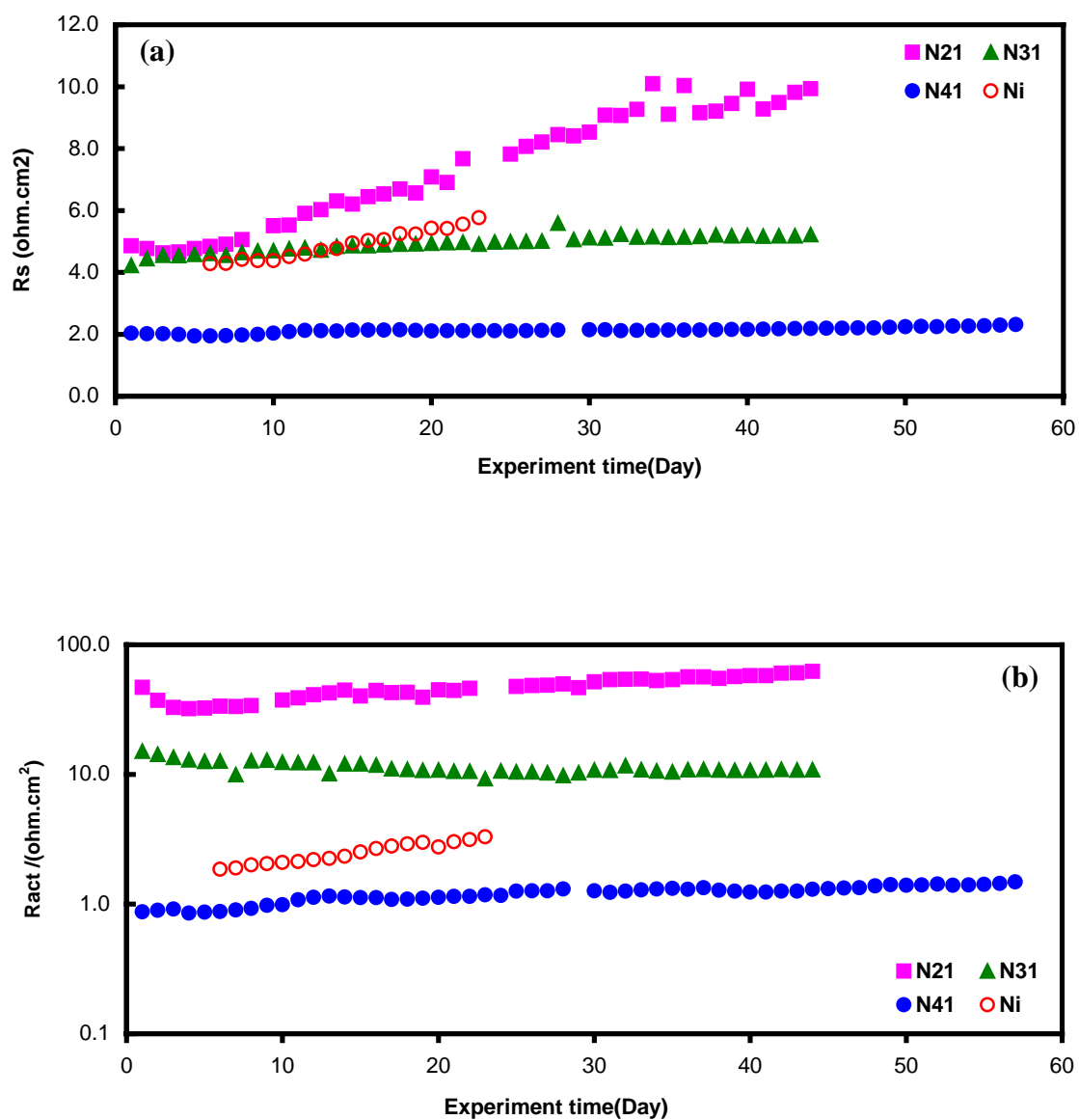
Figure 3.9. a) Series resistance R_s and b) apparent charge transfer resistance R_{act} change with time for Ni/sodium titanate electrodes with the mass ratios of 2/1, 3/1 and 4/1.

For N21 electrodes, R_s and R_{act} increased with experiment time rapidly and they performed even worse than pure Ni electrode, which indicated that the addition of sodium titanate did not make the role as we expected, neither increasing the reaction area nor restricting Ni grain growth. In these electrodes, it seems that the substitution of sodium titanate for some Ni particles reduces the conductivity of the electrode, and occupies some positions on the interface between electrode and BASE so that the triple phase boundary reaction area decreases.

For N31 electrodes, the electrode conductivity is comparable to the pure Ni electrodes, but the R_{act} is still greater than that of a pure Ni electrode. This indicates that the amount of Ni in the mixed electrode should not be less than 75% mass percent, i.e. 75% mass percent Ni is the minimum to guarantee good electrode conductivity, while this amount seems to be insufficient to increase the electrode reaction area.

For N41 electrodes, the R_s and R_{act} both are smaller and more stable than those of pure Ni metals. In these mixed electrodes, it seems that the sodium titanate restricts the growth of Ni grains so that the electrode retains its good behavior for a long time and greatly increases the reaction area to make R_{act} decrease significantly.

The microstructure of this electrode confirmed this explanation, shown in Figure 3.10 and observed after tested over 60 days. In Figure 3.10(a), the white grains are Ni, such as B and C particles, while the gray grains are the sodium titanates, such as A particles. It is found that these two types of particles interwove with each other, which effectively blocks particle agglomeration. For example, the sodium titanate particle A is

at the neck between the Ni particles B and C. It successfully restricted the B grain further connecting with C and becoming larger.
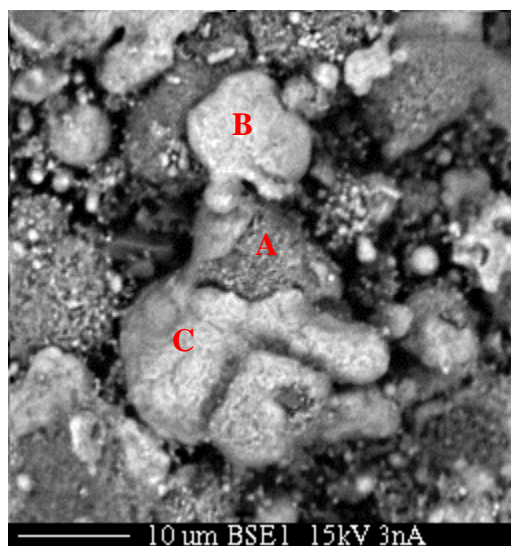
×2000 BSE image
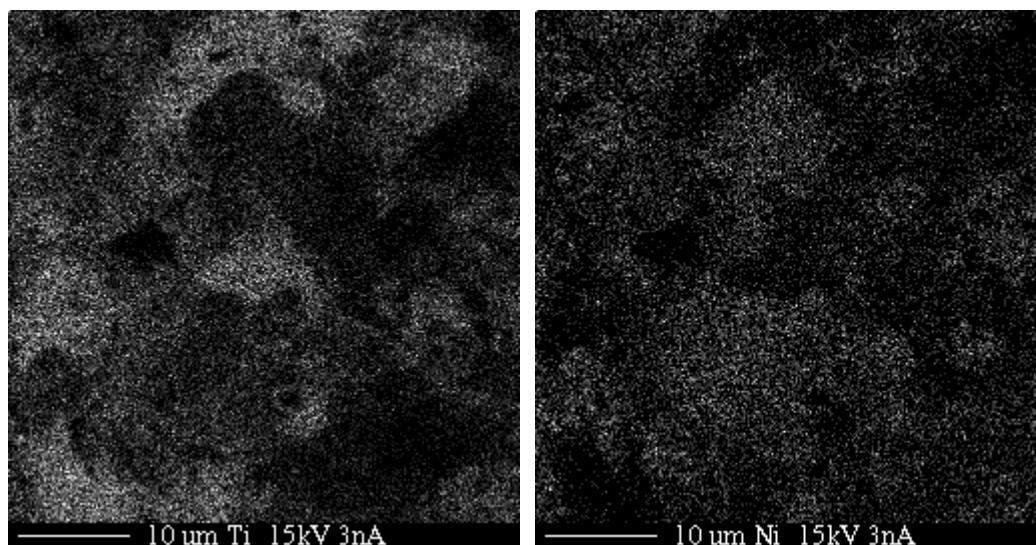
×2000 Ti x-ray map   ×2000 Ni x-ray map

Figure 3.10. Microstructure of Ni/sodium titanate electrode with the mass ratios of 4/1, after testing in a SETC over 60 days.

3.3.4   Theoretical Analysis of the Optimum Composition for MIEEs

For the mixed conducting cathode, the phenomena that take place in the electrochemical process include 1) transport of electrons from the current collector (Ni mesh) to the reaction site through an electronic conductor (Ni); 2) transport of Na^+ ions from the electrolyte to the reaction site through the ionic conductor ($Na_2Ti_3O_7$); 3) electrochemical reactions at an electrochemically active site; 4) the reaction product, sodium vapor, diffuses from the reaction site to the outside surface of electrode through pores present in the electrode.   Therefore, the best MIEE should effectively support those four processes with as small resistance as possible.

In a MIEE there are three cluster types formed by mixed metal and ceramic particles, shown in Figure 3.11.   We will focus on the ionic conductor, though similar conditions apply to the electronic conductors.   Type A clusters are not interrupted through the electrode, present many branches, and connect with each other to form a network, which provides ion paths directly from the electrolyte to the current collector.   Type B clusters are shorter chains connected only to the electrolyte, which bring Na^+ ions only though a fraction of the electrode.   Finally, type C clusters are completely isolated from the electrolyte and current collector; they do not assist in ionic conduction.
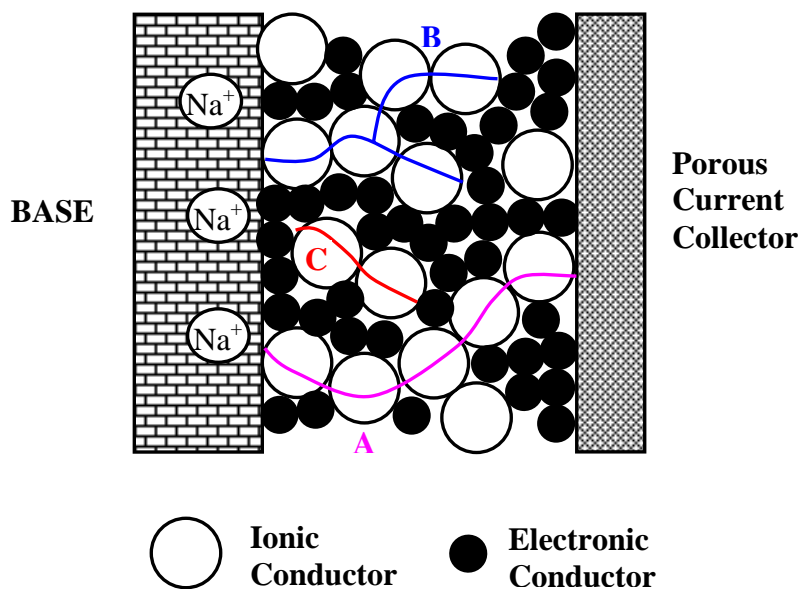
Figure 3.11. Scheme of the mixed ionic and electronic electrode, and different types of clusters formed by the particles.

Two parameters are of great importance for good electrode performances: a large three-phase boundary area, which is the active area for the electrochemical reaction, and high ionic and electronic conductivities. In order to have good conductivity, particles of the same type (electronic conductor or ionic conductor) have to touch each other so that a network is formed through the electrode, such as the type A clusters, which can effectively supply electrical charges to the whole electrode. Moreover, adequate contact between particles of different types ensures that a large active reaction area is formed. Therefore, having both the electron and the ion conduction paths continuous throughout the electrode is necessary for good performance, i.e., a large number of A-clusters must be present in the electrode for both types of conductor. Mathematical modeling shows

that there is a critical value for the volume fraction of electronic or ionic conducting particles, under which the particles form only B- and C-clusters in the electrode. Only above this threshold is a network of A-clusters formed. This critical value of the volume fraction (V_c) is referred as the percolation threshold. Percolation theory shows that above the percolation threshold, some of the physical properties of system will change sharply and will scale according to the universal law $\Phi \propto (V - V_c)^b$, where Φ represents a physical property, such as the electrical or thermal conductivity and the exponent b is insensitive to the microstructure of the composite.[88-89] For a MIEE, there are two percolation thresholds present, one for the electronic conductor and another for the ionic conductor. A sharp increase in the performance has been predicted to occur at the percolation thresholds and there is a window of compositions between the percolation thresholds in which the performance is predicted to be very high. Additionally, the pores in the electrode also need to satisfy percolation theory. But since the size, shape and number of pores are controlled by the fabrication techniques, we don't consider its effect on the optimal performance of the electrode in this model. In fact, for sputtering or flame spray fabrication technique, the deposited film has 30-40% void density, which could higher than the percolation thresholds for the pores.

Some researchers have applied the theory of percolation threshold in studying the properties of composite materials.[90-93] In this research we developed a model to assess the optimum composition of an AMTEC electrode, based on the theories of percolation and binary random packing of spheres.

The model is valid between the percolation thresholds of the ionic and the electronic conductors and is based on the following assumptions: (1) steady state conditions;(2) one-dimensional model as a function of the electrode thickness (x) (3) uniformity of temperature, pressure, reactant and product concentration;(4) each of the two conducting phases within the electrode is considered as continuous and homogeneous, having a resistivity independent of the x coordinate; 5) the particles that form the electrode are spherical, and 6) all particles of the same type have the same diameter.

For the mixed electrode consisting of spherical electronic conductors, i.e. metal particles of radius r_e and spherical ionic conductors, i.e. ceramic particles of radius r_i, the particle coordination numbers are calculated using the following equations proposed by Bouvard et al.[94]

$$Z_{i-e} = n_e \frac{Z_i Z_e}{Z} \tag{3.1}$$

$$Z_i = 3 + \frac{Z-3}{n_i + (1-n_i)\lambda^2} \tag{3.2}$$

$$Z_e = 3 + \frac{(Z-3)\lambda^2}{n_i + (1-n_i)\lambda^2} \tag{3.3}$$

where the indexes i and e represent the ionic and electronic conductors, respectively. Z_{i-e} is the average number of electronic particles in contact with an ionic particle. Z_i and Z_e are the coordination numbers of ionic and electronic particles, respectively, i.e. the average number of contacts of both ionic and electronic particles with an ionic particle (Z_i) or an electronic particle (Z_e). Z is the overall average coordination number, which is

6 for binary random packing of spheres. The parameter λ is the particle size ratio, $\lambda = r_e / r_i$ and n_i is the number fraction of ionic particles, which is related to the volume fraction V_i by equation (3.4). The relationship between n_i and n_e, or V_i and V_e is shown in Equation (3.5).

$$n_i = \frac{V_i \lambda^3}{V_i \lambda^3 + V_e} \qquad\qquad n_e = \frac{V_e}{V_i \lambda^3 + V_e} \qquad\qquad (3.4)$$

and $\quad n_i + n_e = 1 \qquad\qquad V_i + V_e = 1 \qquad\qquad (3.5)$

Additionally, there are two more types of coordination number needed to mention, which are the average coordination number of same type particles, $Z_{i\text{-}i}$ and $Z_{e\text{-}e}$. $Z_{i\text{-}i}$ is the average number of ionic particles in contact with an ionic particle, and $Z_{e\text{-}e}$ is the average number of electronic particles in contact with an electronic particle. These two coordination numbers are directly related to the percolation threshold. Relationships between $Z_{i\text{-}i}$ and the percolation threshold have been found by different researchers and there are discrepancies among them. Kuo et al evaluated all these works and concluded that it is more accurate that the percolation threshold of ionic or electronic particles is obtained under the condition of $Z_{i\text{-}i}$=1.764 or $Z_{e\text{-}e}$=1.764 respectively.[95] The relationship is the following, and it is based on the model of Suzuki and Oshima.[96]

$$Z_{i-i} = \frac{Zn_i}{n_i + (1 - n_i)\lambda^2} \qquad\qquad Z_{e-e} = \frac{Z(1 - n_i)}{n_i / \lambda^2 + (1 - n_i)} \qquad\qquad (3.6)$$

Combining equations (3.4) and (3.6), it is found that the percolation threshold is a function of the particle size ratios. We calculated the theoretical percolation threshold of ionic and electronic conductors corresponding to all possible particle size ratios, and

plotted in Figure 3.12. The area limited by these two threshold lines is the predicted high performance range. When $\lambda=1$, the percolation threshold of volume fraction is $V_{ic}=V_{ec}=0.294$, i.e. if the two kinds of particles have the same size, the electrodes with electronic particle volume fractions of 0.294 to 0.706 should display good performance.
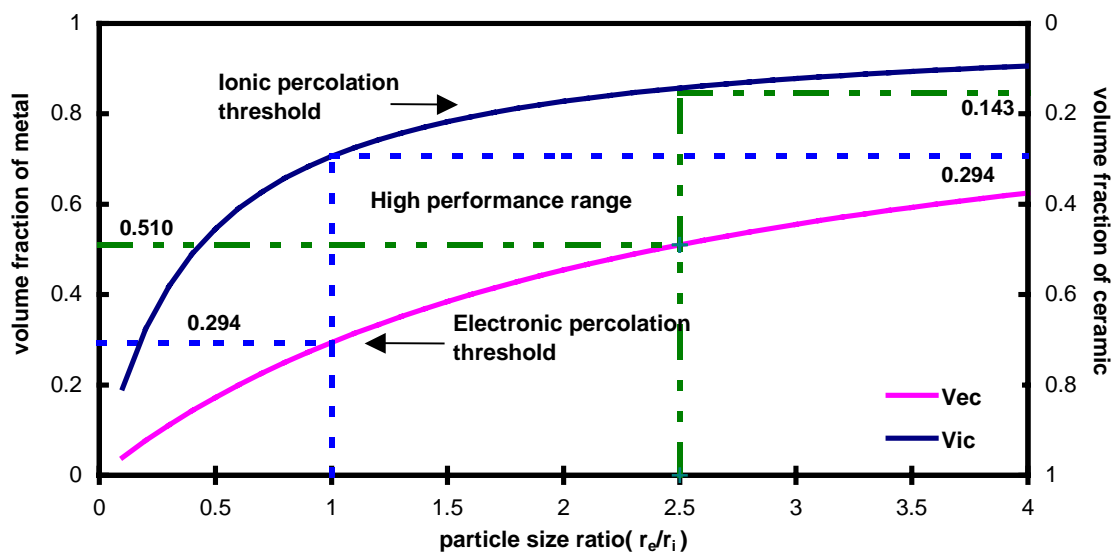
Figure 3.12. The percolation thresholds of the ionic and electronic conductors within the electrode as a function of particle size ratio.

In this research, the purchased sodium titanate has a large particle size, as large as 37 μm. Our previous research results found that such large grain size in an electrode led to very poor performance. Therefore, the powders were ball-milled before being used to make the mixed electrodes. The particle distribution of milled sodium titanate was measured, shown in Figure 3.13. It is seen that the average particle size of milled sodium titanate is about 5μm, but most of the particles are around 2μm. The distribution

of particles smaller than 1.5μm is not accurate due to the limitations of the measurement equipment, so there could be more particles smaller than 2μm. Additionally, the flame spraying deposition process favors depositing the smaller particles on the BASE surface. Thus, it is reasonable to believe that most of sodium titanate practically deposited on the electrodes are 2μm or smaller. The Ni has the particle size of 5~15μm, thus the particle size ratio of Ni to sodium titanate should be larger than 2.5. Based on Figure 3.12, the electrode should have at least 0.510 volume fraction of Ni and 0.143 volume fraction of sodium titanate, in order to produce high performance. In this research, we tested electrodes with the Ni/sodium titanate mass ratios of 2:1, 3:1 and 4:1, which correspond to Ni volume fractions of 0.47, 0.57 and 0.64 respectively. Since the volume fraction of 0.47 is smaller than percolation threshold of 0.510, few A clusters should be present in this electrode, which could cause the poor conductivity and small reaction area. We observed these results in our experiments, in which the conductivity of the N21 electrode is very poor and much lower than pure Ni electrode, discussed in previous section. For N31 and N41 electrodes, both metal and ceramic have the volume fraction greater than their percolation threshold, therefore, these electrodes should perform better and have a large number of A clusters. Figure 3.14 shows the physical morphology of N41 electrode after testing in a SETC over 60 days. It is found that Ni particles connected with each other and formed a network covering the whole area, which are A clusters defined previously. Therefore, this electrode has a high conductivity and large reaction area.
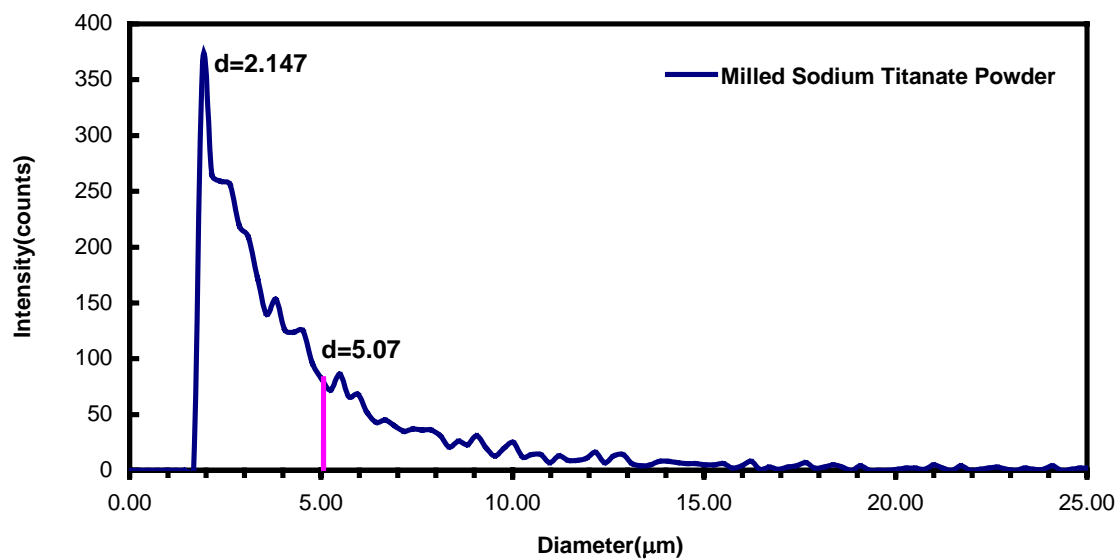
Figure 3.13. The particle size distribution of milled sodium titanate powder.
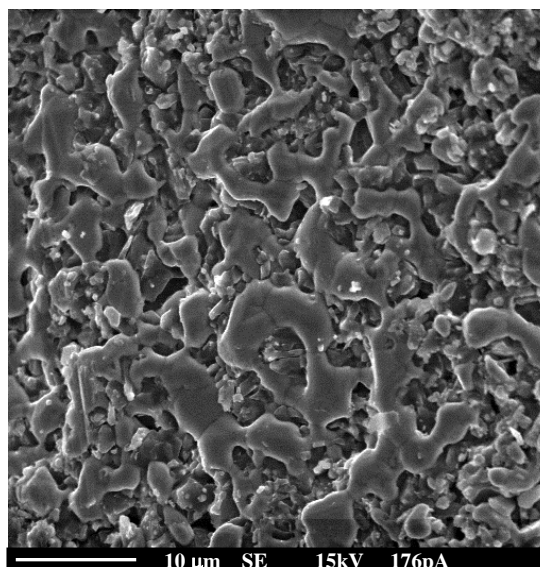
×2000 SE image

Figure 3.14. SEM image of the Ni/sodium titanate electrode with 4/1 mass ratios after testing in the SETC over 60 days.

Since reaction area or active area (A) is a very important parameter that affects the performance of electrodes, we also calculated it in this simulation. For a MIEE, the total reaction areas are the sum of the reaction area at the interface between the electrode and electrolyte, i.e. the traditional triple phase boundary reaction area, where the electrons combine with Na^+ ions from BASE and release Na gas, and the reaction area between electronic and ionic conductors within the electrode. In this simulation, we don't count the former reaction area at the interface, since the latter one is unique for the MIEE.

The reaction area per unit volume is proportional to the number of contact points per unit volume between electronic and ionic conductors, multiplied by the probability that an electronic and an ionic conductor particle belong to type A-clusters:

$$A \propto n_i Z_{i-e} P_i P_e \tag{3.7}$$

The number of particles per unit volume ($n*$) is given by equation (3.8)

$$n^* = \frac{\varepsilon}{\frac{4}{3}\pi r_i^3 [n_i + (1-n_i)\lambda^3]} \tag{3.8}$$

where ε is the packing density, which depends on the particle size and size ratio. The probability that an ionic conductor particle belongs to an A-cluster above the percolation threshold is evaluated by Bouvard as

$$P_i = \left(1 - (2 - Z_{ii}/2)^{2.5}\right)^{0.4} \tag{3.9}$$

Combining equations (3.1), (3.7), (3.8) and (3.9), we obtain equation (3.10)

$$A = Sn^* n_i n_e \frac{Z_i Z_e}{Z} P_i P_e \tag{3.10}$$

where S is the contact area between a Ni particle and a sodium titanate particle. Figure 3.15 shows this contact area schematically. The contact area is determined by the contact angle (θ) and the radius of the smaller particle: $S = \pi r^2 (\sin \theta)^2$, where θ is assumed as a constant in this simulation.
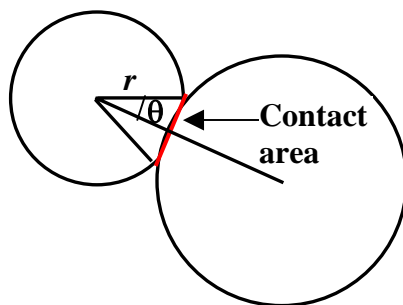
Figure 3.15. Schematic of contact area between ionic and electronic particles.

We calculated reaction areas for MIEEs with all kinds of composition and various particle dimensions, shown in Figure 3.16. A is zero when the volume fraction is less than the percolation thresholds, where the probability P is zero. (Equation (3.9) has been slightly modified so that P=0 at the percolation thresholds.) It is found that the reaction area A has the maximum value with the volume fraction change. For example, if two components have the same particle size, i.e. λ=1, the maximum A is obtained when the electrode has equal volume fractions of electronic and ionic components, i.e., $V_i=V_e$=0.5. If the two components have different particle sizes, i.e., when λ is varied between 1 and 4, we can find that the volume fraction of Ni corresponding to the maximum A shifts to

the right side, the high value side.   When $\lambda=4$, a volume fraction of 0.75 for Ni is required to reach the maximum reaction area.
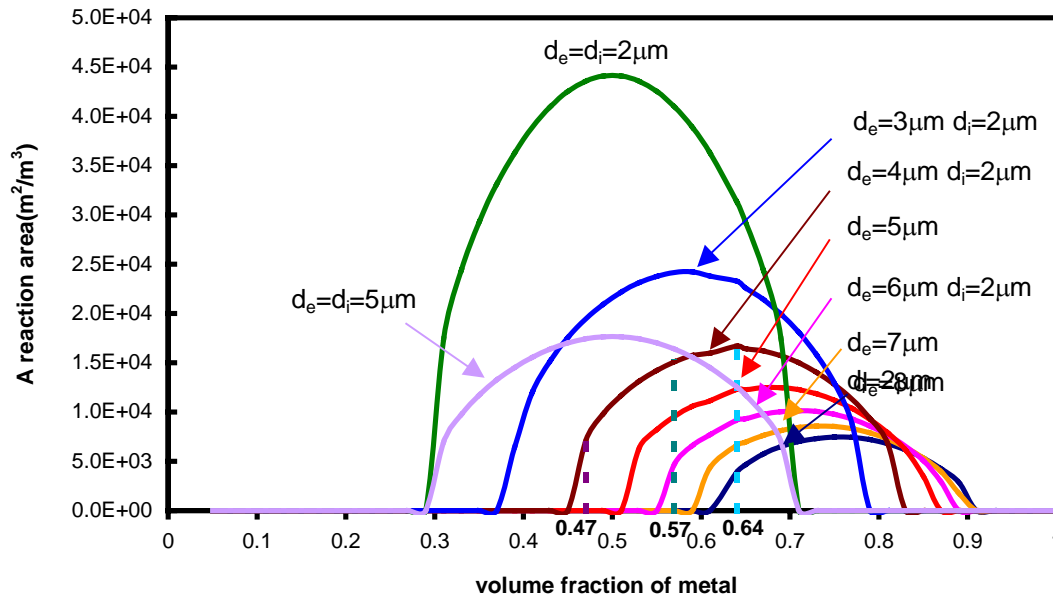
Figure 3.16. Calculated reaction area change with the volume fraction of metal. The packing density ε is set at 0.61 and the contact angle θ is set at 15°.

Figure 3.16 also shows that the value of maximum reaction area decreases with increasing particle size ratio. From $\lambda=1$ to 4, the maximum A value is largest when two components have the same particle size. Additionally, the maximum reaction area also decreases with increasing particle size, when the particle size ratio is fixed.   For example, when $\lambda=1$, the value of maximum A is sharply reduced to less than half if the particle size increases from 2μm to 5μm. It is reasonable, since as the particle size increases, the number of particles in a unit volume decreases, which causes contact area to decrease. Therefore, summarizing above discussion, it is found that in order to obtain

the best performance, the electrode should consist of two components with the same size and volume fractions, and this particle size should be as small as possible.

In this research, we tested electrodes with Ni volume fractions of 0.47, 0.57 and 0.64 respectively. Figure 3.16 shows that reaction area is increasing from V_e=0.47 to 0.64 for all the electrodes with Ni particle sizes from 4-8μm, which is in agreement with our experimental results, shown in Figure 3.9. This explained that N41 electrode performed better than N31 electrode, even both electrode compositions are in the high performance region.

Carefully observing the curves of A vs. V_i for the electrode with Ni particle size from 5 to 8μm, it is found that the volume fraction of 0.47 is below the percolation threshold and A is zero for this electrode. It is different with the experimental results, in which electrochemical reaction did occur and R_{act} is as large as 35ohm.cm^2. Additionally, the experimental results showed that the N41 electrode performed much better than the N31 electrode, but it is not very evident in this theoretical simulation.

Generally speaking, in our electrode, the particles do not have an exactly spherical shape, nor is the diameter exactly defined; on the contrary there is a distribution around a mean value. These factors can influence the percolation thresholds in a real electrode. Figure 3.17 shows the particle size distribution in N41 electrode. It is found that particles have different sizes over a large range, which definitely affects the accuracy of the percolation threshold calculation. Compared to the sodium titanate particle distribution, Figure 3.11, we found a wider distribution of mixed particle sizes between 2μm and 5μm. Since most of sodium titanate particles are around 2μm, it is apparent

that some Ni particles are less than 5μm. Due to the smaller Ni particle present, the particle ratio λ could be less than 2.5. Figure 3.12, shows that 0.47 volume fraction is the percolation threshold corresponding to λ=2.1. Therefore, A-clusters could be formed and provide reaction area in these electrode. Additionally, in our model, we only count the A-cluster's contribution to the electrode performance, excluding the B-clusters. If the electrode thickness is small compared to the particle diameter, the length of B-clusters through the electrode is significant for a wide range of compositions outside the percolation thresholds. Thus even if A-clusters are not present, the B-clusters would contribute to the transport of electrons and ions and the electrochemical reaction through the electrode. Additionally, we mentioned above that A calculated did not include the reaction area at the interface, but in fact, it did exist and contributed to the reaction area.
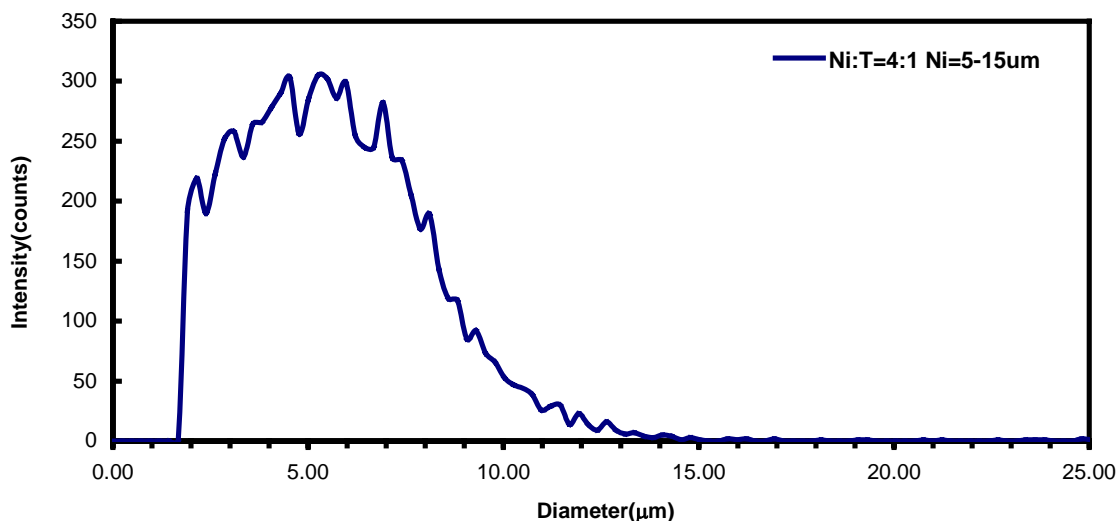
Figure 3.17. The particle distribution of Ni and sodium titanate mixture with the mass ratios of 4:1. The Ni particle purchased is 5-15μm.

The percolation theory requires that the thickness of electrode is much greater than the particle size. The thicker the electrode, the more accurate this model. Under those conditions, if the volume fraction is greater than the percolation threshold, the reaction area and the conductivity will jump sharply up by several orders of magnitude. But our mixed electrode has a thickness of between 10 and 20μm, which just a few times the electrode particle size. Thus, only a few electrode particles are packed in the thickness direction and the randomness of particle packing is very high in such a system, which could cause behavior far different from the theoretical calculation in this model. In summary, all these factors could result in the discrepancy between the experimental results and theoretical simulation.

Although there is some discrepancy present, this model is in agreement with the experimental results for most cases, based on our experimental results. Therefore, it is useful and can be employed to predict the performance of all kind of MIEE.

3.4. Summary and Conclusions

Chemical potential diagrams have been plotted for the Na-Al-O and Na-Ti-O ternary systems and the Na-Al-Ti-O quaternary system, based on the calculation of Gibbs free energy. At AMTEC conditions, the stability region of β''-alumina is very narrow. Whether it is present as β''-alumina or converts to β-alumina and $NaAlO_2$ is dependent on the real oxygen and sodium vapor partial pressures in the system. Sodium titanate $Na_2Ti_3O_7$ is thermodynamically stable at AMTEC operating conditions and also compatible with BASE, thus, it can be used as the ionic component in a mixed

conducting cathode for AMTEC. Al and Ti are not thermodynamically favored for use as AMTEC electrodes, because they are very easily oxidized, since their metal phase stability requires a very low level of oxygen pressure. Ta, Nb and V could be used in AMTEC, depending on the real sytem conditions. Metal Ni, Cu, Ir and Co can be present at any AMTEC condition.

Ta, Ni, Nb, Ir, W and MoRe electrodes have been tested in SETCs. Ir, Nb and Ta did not perform as well as expected. They degraded rapidly due to significant grain agglomeration. Ni was selected as the metal component in a MIEE, since it has the best initial performance among these tested pure metal electrodes, and it also thermodynamically compatible with sodium titanate and BASE, although Ni agglomeration occurred during the test.

Therefore, different compositions of Ni/sodium titanate mixed electrodes were tested in SETCs. It is found that sodium titanate particles effectively reduce Ni particle agglomeration. Among tested Ni/sodium titanate electrodes, the ones with mass ratios of 4/1 performed best. We found that the 75% mass of Ni produced good electrode conductivity. Based on the percolation theory, a model was constructed to interpret the performance of these mixed electrodes and find the optimum composition. The percolation threshold of volume fraction was calculated for both components, which varies with particle size ratio. The composition window corresponding to high performance is defined for a wide range of particle size ratios. The reaction area within the electrode was calculated based on the model. It is found that the reaction area decreases with increasing particle size or particle size ratio. The model also predicted

that the best performance electrode should consist of two components with the same volume fraction and same particle size, and this particle size should be as small as possible.

CHAPTER IV

KINETIC STUDIES OF MIXED IONIC AND ELECTRONIC

ELECTRODES

4.1 Introduction

Based on the experimental results and analysis in Chapter III, it is found that

Ni/sodium titanate mixed electrodes with appropriate composition performed much

better than pure Ni metal electrodes. It is known that the electrode behavior is controlled

by its kinetics, but the kinetics of an AMTEC electrode is still unclear. Therefore, in this

chapter, we proposed possible electrode kinetic mechanisms, and derived the theoretical

expressions for the interface impedance for both pure metal and mixed electrodes.

Based on its stable chemical and physical properties, sodium titanate was selected as

the Na^+ ion conductor in MIEEs. But the most important property, Na^+ ion conductivity,

is still unsure for this compound, although its layered crystal structure suggests it is a

good Na^+ ion conductor. Up to now, few literatures reported the electrical properties of

sodium titanate, and these data are inconsistent.[57-59] Therefore, we also measured the

conductivity of sodium titanate and discussed the results in this chapter.

4.2 Experimental

4.2.1 Measurement of $Na_2Ti_3O_7$ Ionic Conductivity

The purchased sodium titanate powder were milled, dried, and ground, as described

in Chapter III. The ground powders were pressed into pellets (12mm in diameter and

~2mm in thickness) and sintered at 1273K for 18hrs in air. Two sides of the sintered pellets were sputtered with thin Ta layers, which served as electrodes. Ni mesh was used as the current collector. The sample is shown in Figure.4.1. The conductivity was measured from 600K to 1150K at the same conditions as a SETC.
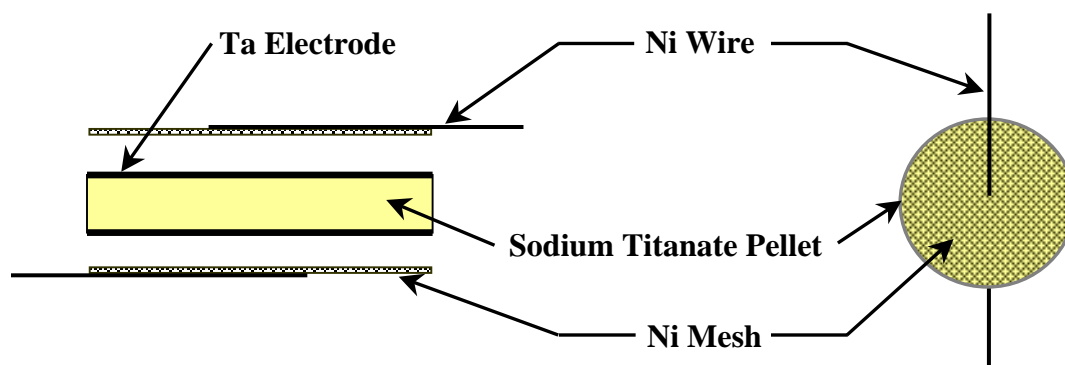
Figure 4.1. Scheme of the experimental cell for sodium titanate conductivity measurements.

4.2.2 Composition Analysis of Sodium Titanate

Composition analyses of the milled powder were carried out by X-ray diffraction (XRD). XRD data were collected at room temperature using a Bruker-AXS D8 Powder diffractometer with Cu $K_{\alpha 1}$ X-rays (λ=1.5405Å), and a 2θ scanning step of $0.04^{o}/4s$ from 5° to 70°. Sodium titanate phases were identified by comparison with the Joint Committee for Powder Diffraction Studies (JCPDS) cards.

The SETC setup procedures and the preparation and performance measurement of pure metal and mixed electrodes were already discussed in Chapter III.

4.3 Results and Discussion

4.3.1. Ionic Conductivity of Sodium Titanate

The sodium titanate pellets shrank during the sintering process; their diameter was reduced 6~8%.   The final density of the sample was approximately 85% of the theoretical densities.

The XRD analyses found that there are mainly two phases in our powder, $Na_2Ti_3O_7$ and $Na_2Ti_6O_{13,}$ shown in Figure 4.2. Since they are both monoclinic structures, a semi-quantitative chemical analysis was performed using the ratios of intensities of the 100 peak of each components. This analysis indicated the ratio of $Na_2Ti_3O_7$ to $Na_2Ti_6O_{13}$ was 1/2 by mass.
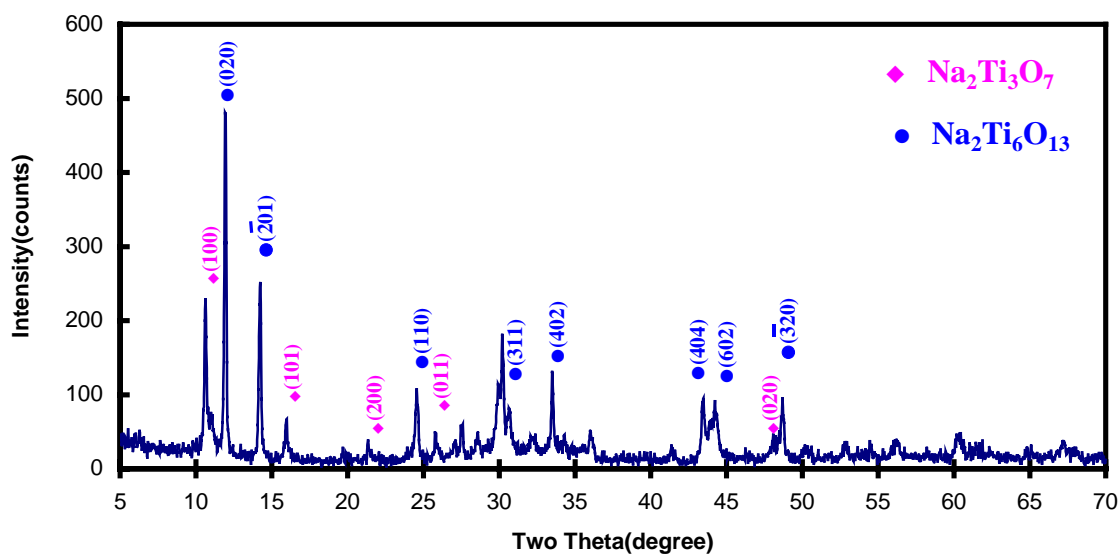
Figure 4.2. X-ray diffraction pattern of raw sodium titanate powder.

The measured impedance spectra are shown in Figure 4.3. Each impedance spectrum consists of a depressed semicircle in the high-frequency range and a line in the low-frequency range. The radius of the semicircle and its intercept at high frequency decreased with temperature increase. These spectra are in agreement with other research reports and one kind of typical spectra for a pure ionic conductor.[86] In principle, a semicircle between the origin and the intercept would be observed if much higher frequencies were used in the experiment. The high-frequency limit should be as high as 0.1GHz because the conventional value of geometric capacitance (C_{geo}) is about 10pF for ceramic materials. The high-frequency limit imposed by the equipment used in this study (100kHz) is not sufficient to observe this phenomenon. This missed semicircle corresponds to the polarization of sodium titanate grain interiors, i.e. the bulk conduction process, and the intercept represents the total ionic resistance of sodium titanate bulk grains, while the semicircle present is usually assigned to the relaxation process in the sodium titanate grain boundaries, i.e., grain boundary conduction. The tail at low frequency is related to the polarization of the electrode/sodium titanate interface.[86] Figure 4.3 (a) is the spectra measured at low temperatures (614 and 672 K). The data are somewhat messy at low frequency due to noise, which decreases as temperature increases. The enlarged plot shows that the spectra did not end at the origin and it is very clear when the spectrum measured at high temperature, shown in Figure 4.3(b) and (c), which was measured at 1068K.
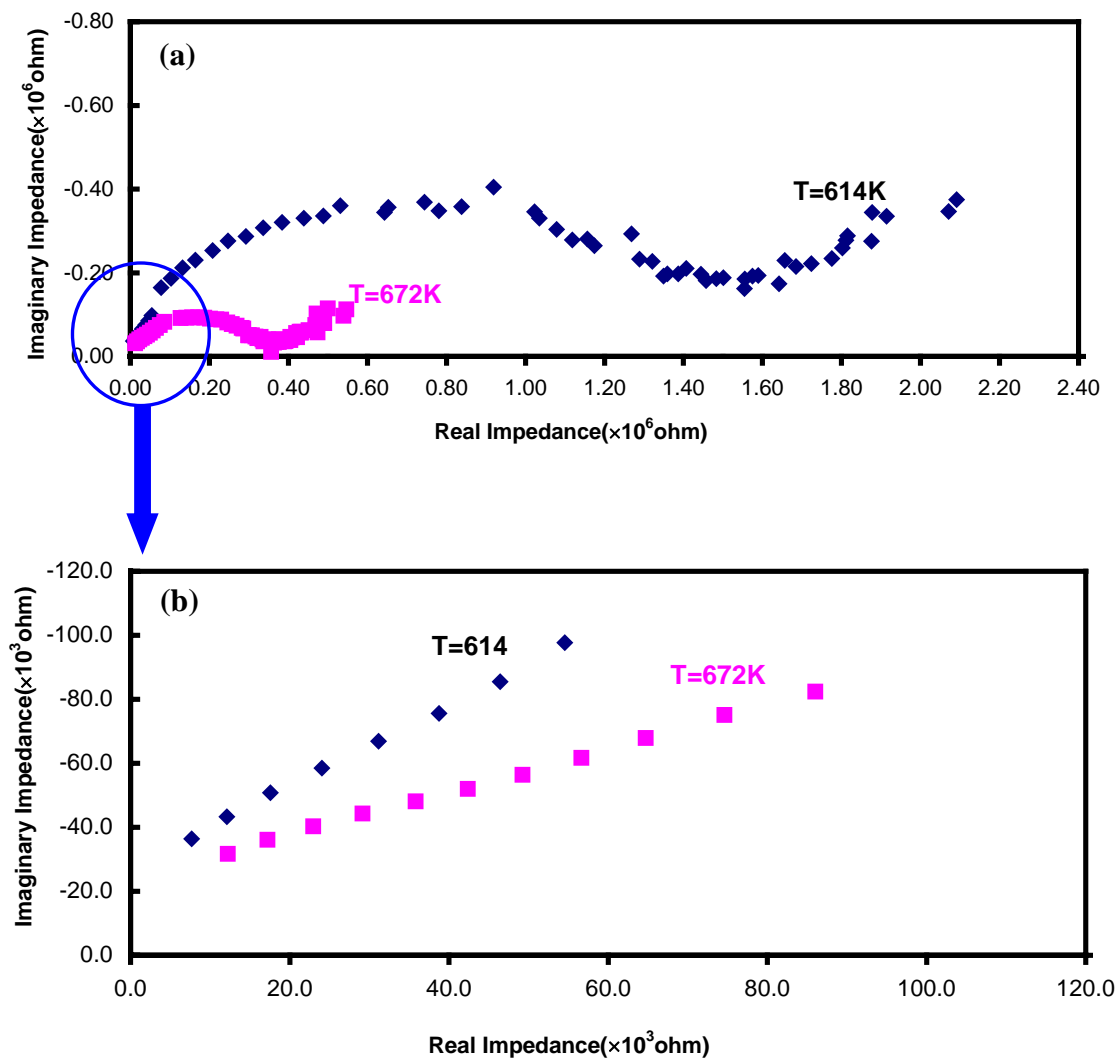
Figure 4.3. Impedance spectra of sodium titanate measured at different temperature (a) full spectra measured at 614 and 672K. (b) high frequency part. (c) full spectrum measured at 1068K. (d) Bode plot measured at 1068K.
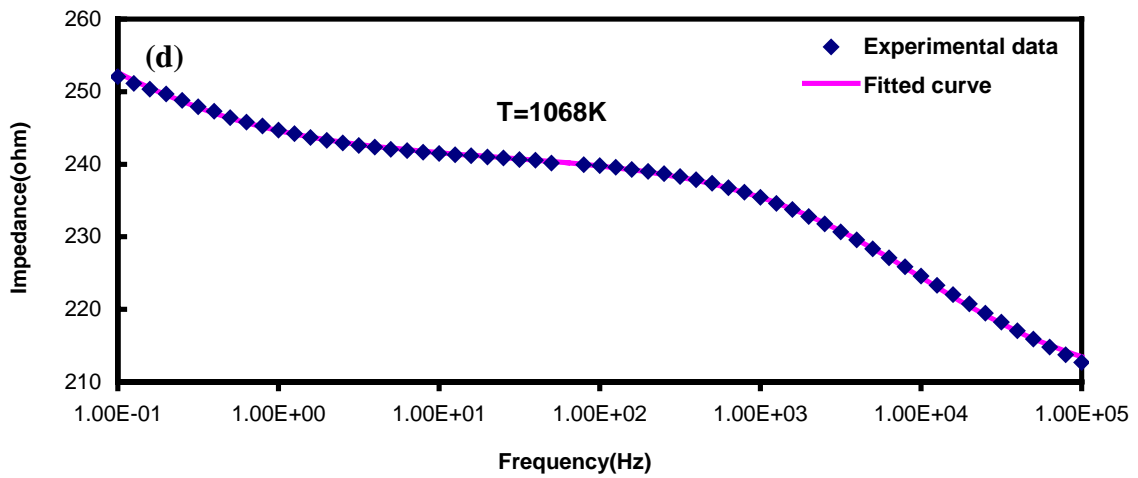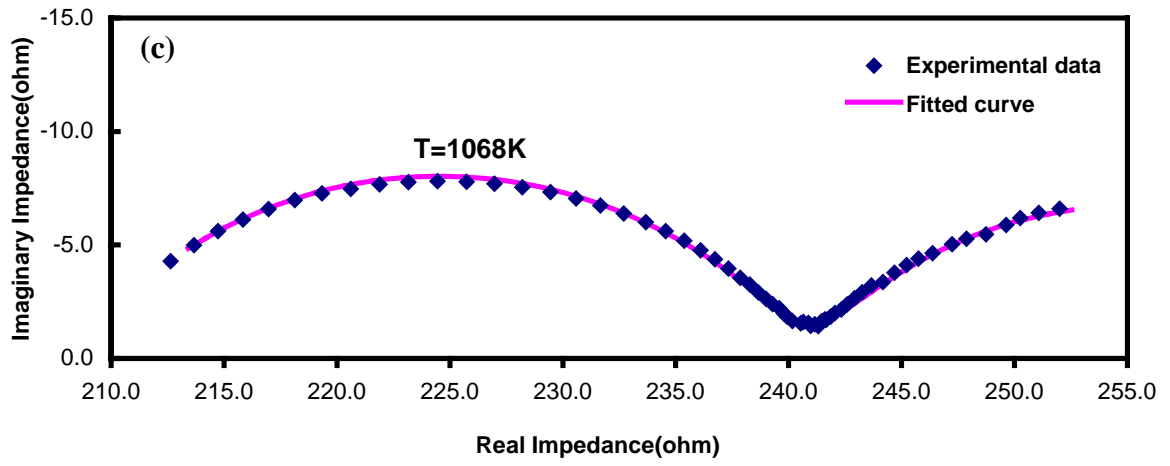
Figure 4.3. (Continued)

The depressed semicircle is indeed the arc of a circle with the center some distance below the x-axis, which is very commonly observed in most ceramic materials and generally fitted by a constant phase element (CPE) in parallel with a resistance. A CPE is a non-intuitive circuit element that was invented to describe non-ideal capacitive behavior. Mathematically, a CPE's impedance is given by

$$Z = 1/[T(j\omega)^p]$$ (4.1)

where T has the numerical value of the admittance $(1/|Z|)$ at $\omega=1$ rad/s. The units of T are $S \cdot s^p$. p is an exponent between 0 to 1 and when it is equal to 1, the CPE turns into a real capacitor. Equation (4.1) determines the phase angle of the CPE impedance has a value of -(90*p) degrees, independent of the frequency. This property gives it the name CPE.[61,86]
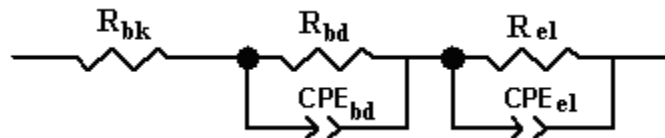
Figure 4.4. Equivalent circuit for the impedance spectrum of sodium titanate ionic conductor.

Based on above analysis, an equivalent circuit model (ECM) was constructed to fit the impedance spectra, shown in Figure 4.4, which consists of a resistance in series with two similar sections. Each of these sections is comprised of a resistance and a CPE in parallel. The section of R_{bd} in parallel with CPE_{bd} corresponds to the polarization of

sodium titanate grain boundary, while the section of R_{el} in parallel with CPE_{el} refers to the electrode polarization process. Since the high frequency semicircle did not show in our measurement, a resistance R_{bk} is used to represent it and its value is equal to the total ionic resistance of sodium titanate bulk grains. The fitted curves for the Nyquist and Bode plots are shown in Figure 4.3 (c) and (d) respectively. The level of agreement between experiment and curve fit is quite satisfactory in terms of shape and distribution of frequencies on the spectrum. Based on this equivalent circuit, all the parameters were extracted, and listed in the Table 4.1. Comparing the bulk resistance R_{bk} to the boundary resistance R_{bd}, we found that the resistance of the grain interior conduction is much larger than that of the grain boundary, which means the sodium ion transport inside the grain is more difficult than along the grain boundary.

Table 4.1. The parameters used in the equivalent circuit

	$R_{bk}(\Omega)$	$R_{bd}(\Omega)$	$R_{el}(\Omega)$	$CPE_{bd}\text{-}T$	$CPE_{bd}\text{-}p$	$CPE_{el}\text{-}T$	$CPE_{el}\text{-}p$
Value	208	33	28	5.40E-05	0.575	0.062	0.56
Error%	0.11	0.98	7	5.18	1.03	2.42	3.2

In order to confirm the validity of these parameters, the impedance of grain boundary CPE ($CPE_{bd}\text{-}T$) was converted to the corresponding capacitance and compared to the literature. Using equation 4.2 provided by the literature,[97,98] we got the "true" grain boundary capacitance of approximate 1nF, which is in the range of grain-boundary capacitances of typical polycrystalline ceramic ionic conductors.[86] Therefore, these

parameters extracted in our experiment are valid. Based on the parameters of R_{bk} and $R_{bd,}$ the conductivity of sodium titanate is calculated.

$$\omega_{max} = (CR)^{-p} \tag{4.2}$$

$$\sigma = \frac{\sigma_o}{T}\exp(-E_a/RT) \tag{4.3}$$

The conductivity is dependent on the temperature, as described by the Arrhenius law, equation (4.3). Therefore, by plotting the logarithm of conductivity versus reciprocal temperature we can get the activation energy, shown in Figure.4.5, where the total conductivity includes both bulk and grain boundary conductivities. The average activation energy for the bulk and total conductivities are 0.87ev and 0.96ev, respectively. Compared to the literature reports about the conductivity of sodium titanate, listed on Table 4.2, our results are higher than most of them, but not unreasonable.
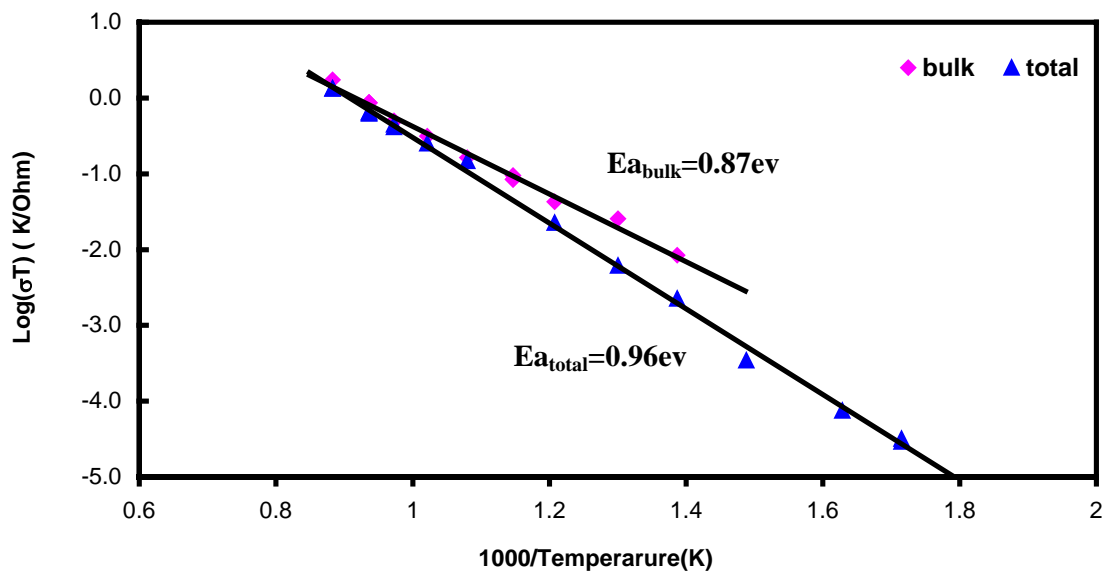
Figure 4.5. Arrhenius plots of bulk and total conductivities for sodium titanate.

Table 4.2. Summary of the sodium titanate conductivity measured in the literature

Composition	Measurement Technique	Measurement Temperature (K)	Activation Energy (eV)	Authors	Date
$Na_2Ti_3O_7$	EIS	500~750	bulk+boundary 0.70	S.Kikkawa et al[57]	1985
$Na_2Ti_3O_7$	d.c. conductivity measurement	400~475 475~650 650~800	0.36 0.70 0.33	S. Pal et.al[58]	1989
$Na_2Ti_3O_7$	EIS	293~493	bulk+boundary 1.3	K.Byrappa et al[59]	1997
$Na_2Ti_3O_7$	EIS	700K~1000K	bulk+boundary 0.79~0.80	A-L.Sauvet et al[102]	2004
$Na_2Ti_3O_7$ $+Na_2Ti_6O_{13}$	EIS	740~970K	bulk+boundary 0.62	J. Ramirez-Salgado et al[99]	2004
$Na_2Ti_3O_7$ $+Na_2Ti_6O_{13}$	EIS	600~1150K	bulk+boundary 0.96	Guo and Schuller	TBD

Comparing to J. Ramirez-Salgado's results,[99] who measured the conductivity of a sodium titanate mixture, the activation energies obtained in this research are higher than theirs. The difference could be caused by the composition of the sample measured. Their sample consisted with the mixture of 3/1 ratios of $Na_2Ti_3O_7$ to $Na_2Ti_6O_{13}$ by mass, while our ratio was only 1/2 of $Na_2Ti_3O_7$ to $Na_2Ti_6O_{13}$ by mass. Our sample has less amount of $Na_2Ti_3O_7$, which results in the higher activation energy, since $Na_2Ti_3O_7$ has higher conductivity than $Na_2Ti_6O_{13}$. Additionally, they only measured the total conductivity, which includes the bulk and boundary contribution together. The conductivity of the grain boundary is affected by some factors, such as the synthesis

method, sintering procedure and boundary size and shape. Therefore, the bulk conductivity is used to represent the material's conductivity, not the boundary conductivity.

The sodium titanates $Na_2Ti_nO_{2n+1}$ (n=3~8), crystallize in a monoclinic structure, in which TiO_6 octahedra share edges to form layered lattices and sodium occupies the interlayer regions. With different values of n, the crystal structure changes. For n=3 or 4, the structure consists of $(Ti_3O_7)^{2-}$ layers held together by sodium ions. With a low sodium metal content (n=6-8), tunnel structures (Figure.4.6.) are observed, which we would expect to exhibit low conductivity and good chemical stability.[100,101] Therefore, a mixture of $Na_2Ti_3O_7$ and $Na_2Ti_6O_{13}$ should have lower conductivity than pure $Na_2Ti_3O_7$. Based on the somewhat inconsistent literature, the activation energy of $Na_2Ti_3O_7$ is between 0.70-0.80 ev. Therefore, our mixture's bulk conductivity activation energy of 0.87ev is consistent with its composition and literature values.

Figure 4.5 also shows that the bulk resistance dominates the high temperature region, since it is approximately equal to the total resistance. This indicates that the grain boundaries have very good conductivity at high temperature. At AMTEC working temperatures (~1120K), only about 10% of the resistance is contributed by the grain boundary. It is reported that relatively small grains or discrete boundaries have a small resistance.[103]

Na₂Ti₃O₇
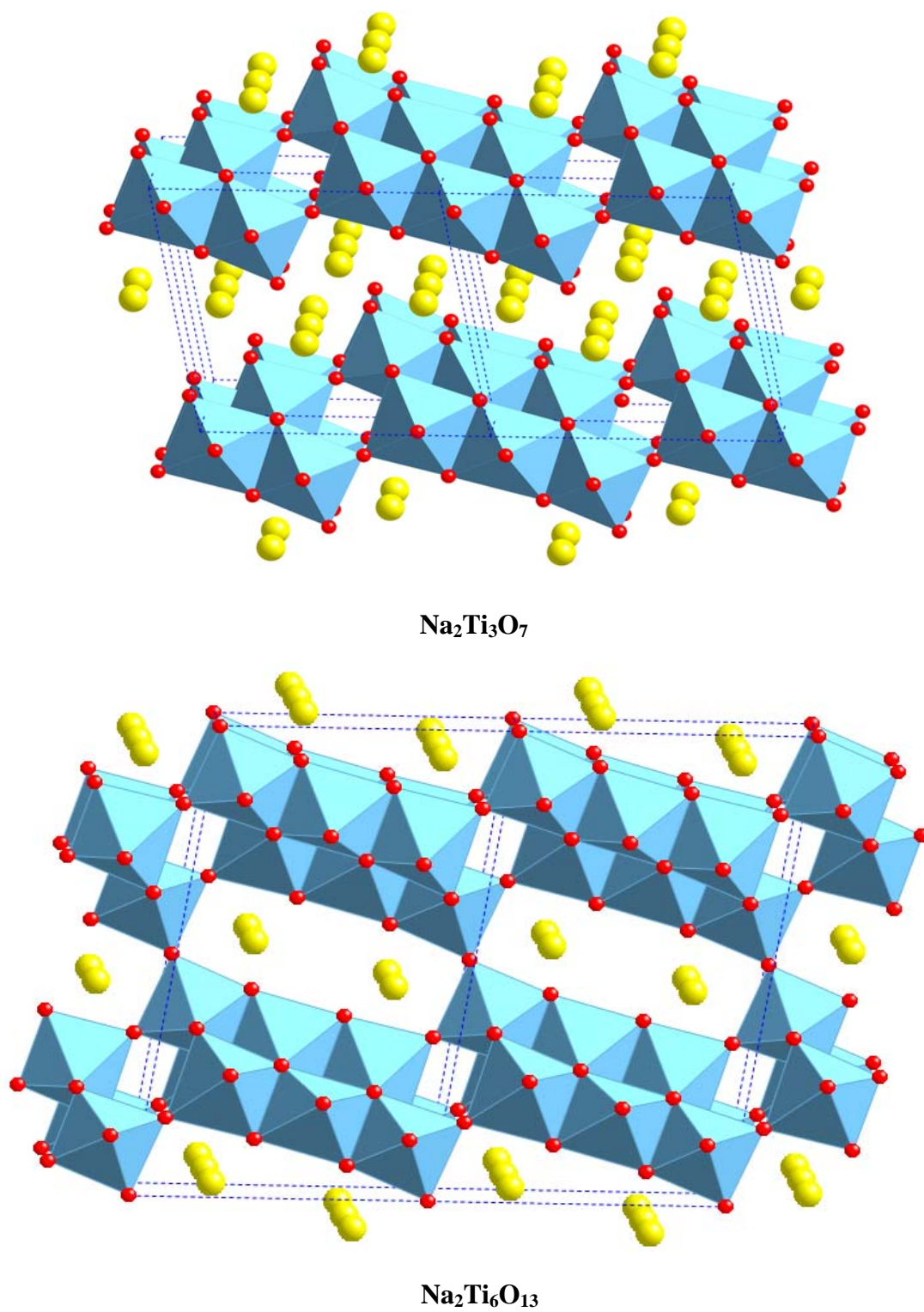
Na₂Ti₆O₁₃

Figure 4.6. Crystal structures of Na₂Ti₃O₇ and Na₂Ti₆O₁₃ sodium titanates.

4.3.2 Pure Metal Electrode Kinetic Mechanism

In this research, we tested some pure metal electrodes, including Ni, Ta, W, Ir, and Nb. Based on the data in Chapter III, it is known that the Ni electrode displayed the best initial performance and was selected as the metal component for a MIEE. Here, we use it as an example to analyze the kinetic mechanisms of pure metal AMTEC electrodes. In fact, Figure 3.2 shows all the metal electrodes have very similar electrochemical spectra, which indicates they have the same kinetic mechanisms.

Figure 4.7 shows the electrochemical spectrum (solid diamonds) of a Ni electrode. Deconvoluting this spectrum, two arcs (solid line) are obtained, which indicates that at least two processes contribute to the electrode polarization. Based on electrochemical theory, the high frequency impedance generally is related to charge transfer, and the low frequency impedance is related to mass transfer. Combining electrochemical theory with complex nonlinear least squares analysis, the equivalent circuit is created, shown in Figure 4.8. It is used to model the impedance spectrum (open triangles), and it produces excellent agreement with the experimental results. Figure 4.7 also shows that the charge transfer resistance is smaller than the diffusion resistance, which means Na diffusion in the electrode is more difficult than the electrode reaction. In fact, the same phenomenon was found for all tested pure metal electrodes. For a pure metal porous electrode, the charge transfer reactions only can occur at the interface of BASE, electrode and vapor space. The Na vapor will diffuse from the interface to the electrode surface through the pores in the electrode. Na is not soluble in the electrode, so cannot be transported

through the metal. The experimental results indicate that although the reaction area at

the interface is limited, the Na gas diffusion rate is slow enough to limit the current.
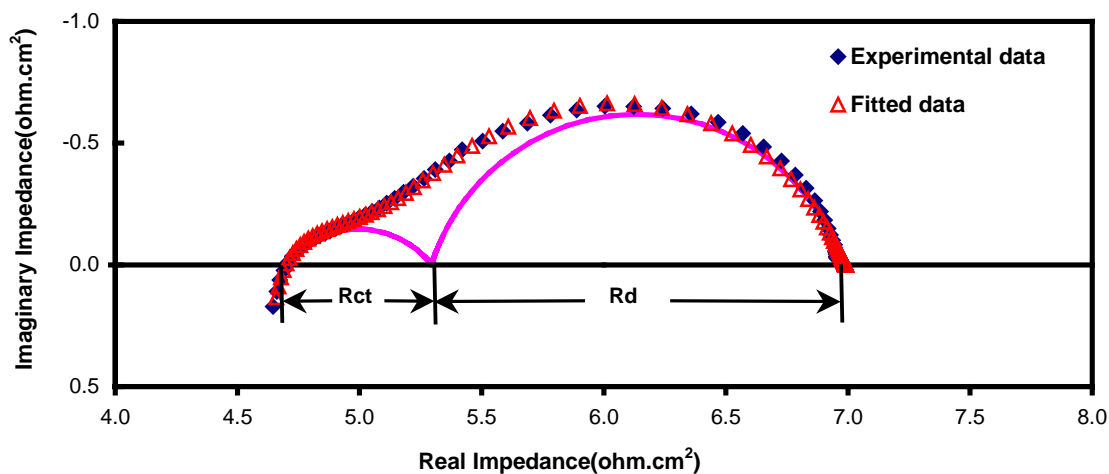
Figure 4.7. Impedance spectra of Ni electrode measured at 850°C. The solid diamonds
($\blacklozenge$) represent the experimental data; the open triangles (Δ) are calculated using the
equivalent circuit in Figure 4.8; the two semicircles are the theoretical impedance
spectra of charge transfer and sodium transport impedance respectively.
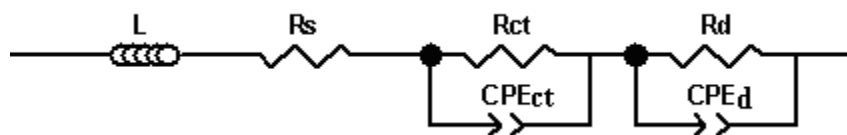
Figure 4.8. Equivalent circuit for interpreting and fitting the electrochemical
spectra of a Ni electrode.

Physical parameters for pure metal electrode processes were extracted from the fitting routine and plotted as a function of time in Figure 4.9. They all increase with experimental time and the reasons were already discussed in Chapter III.
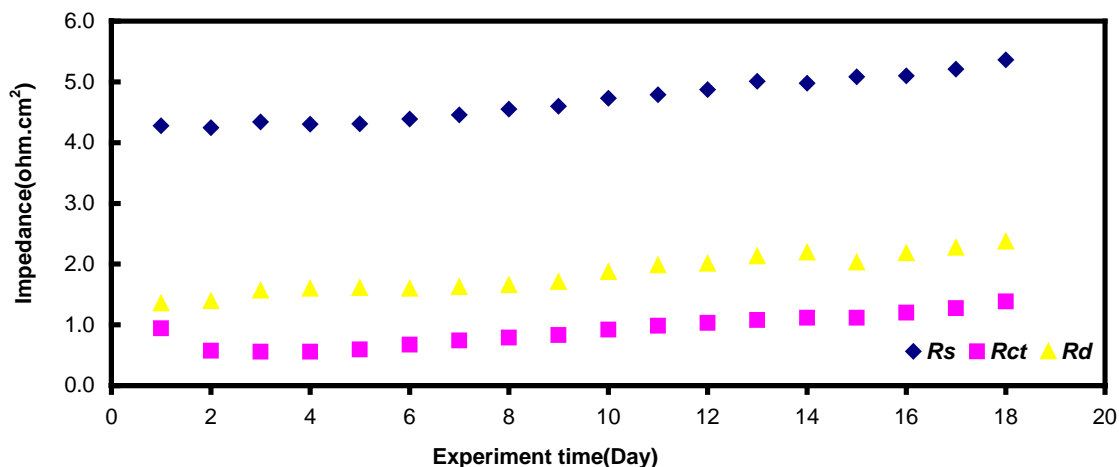
Figure 4.9. The changes of series resistance R_s, charge transfer resistance R_{ct} and diffusion resistance R_d with experiment time for a Ni electrode.

In the equivalent circuit, Figure 4.8, the constant phase elements are used to represent the capacitive behavior of the electrode process. The literature reported that a CPE is generally used in an inhomogeneous system to account for factors, such as surface roughness, varying thickness or composition, or a distribution of reaction rates.[104] It has been shown that the exponent p in the equation (4.1) is equal to $1/(D-1)$,[105] where D is the fractal dimension. For an absolutely flat surface the fractal dimension (D) is 2.0 and $p=1$, which is a capacitor, while for a highly contorted surface ($D=3$), and $p=0.5$, it produces an infinite length Warburg element, which corresponds to

charge carrier diffusion through a thick material, such as a thick porous electrode. Our experimental results show that p is between 0.52 to 0.69, corresponding to a D of 2.92 to 2.45, which indicates that our electrode/electrolyte interface could be really rough and fractal.

It is also possible that the CPE in our system is caused by varying thickness or composition of the electrode film, which has been reported for a coating with varying composition along the coating thickness.[106] Our SEM images show that the thickness of the electrode is not uniform, but this may result from the sample preparation for SEM observation. Therefore, we can not conclude if this factor contributes to the CPE effect in our work.

In order to analyze and interpret the experimental results, it is necessary to derive a theoretical expression for the impedance of electrode process. For pure metal electrodes, the electrode process consists of a charge transfer reaction at the interface triple phase boundary and sodium vapor transport in the porous electrode, shown in Figure 4.10. Sodium vapor transport in the porous electrodes might include the following three steps:

1. Surface diffusion of sodium on the electrode particles.

2. Desorption of sodium from the electrode particles.

3. Vapor phase transport in the pores of the electrode.

We use two reactions to represent electrode process. The first reaction is charge transfer (Na^+ ion reduction at the cathode) and the second reaction represents the Na vapor transport in the electrode, which includes all three steps described above.
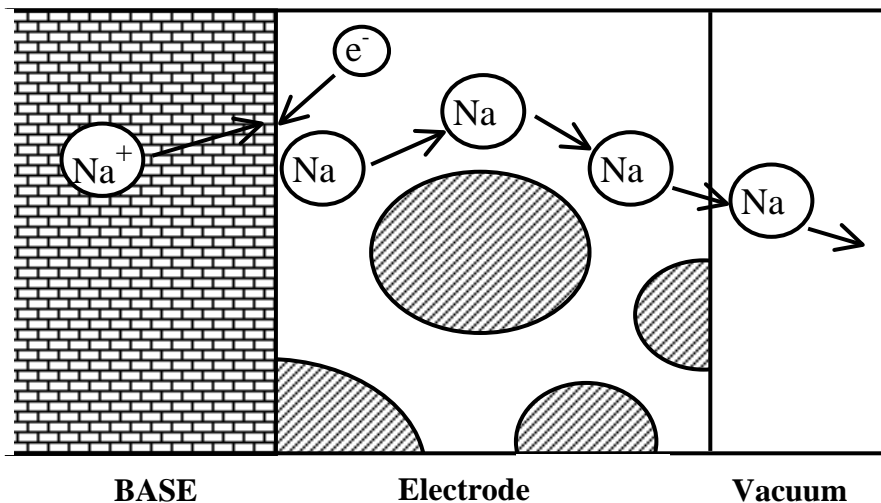
Figure 4.10. Schematic representation of the electrode reaction process.

$$Na^+ + e \; \underset{k_b}{\overset{k_f}{\rightleftharpoons}} \; Na_{ads} \qquad (4.4)$$

$$Na_{ads} \; \underset{k_{-2}}{\overset{k_2}{\rightleftharpoons}} \; Na_{vap} \qquad (4.5)$$

Electrochemical theory[107] defines the current as

$$i = \vec{i} - \bar{i} = nFA[k_f C_{Na^+}(0) - k_b \frac{P_{in}}{RT}] \qquad (4.6)$$

where n is the number of electrons involved in the electrode reaction, which is 1 in reaction (4.4); F is the Faraday constant; A is the interface area; k_f and k_b are the potential-dependent rate constants for the forward and backward reactions:

$$k_f = k_o \exp[-\alpha nf(E - E^o)] \qquad k_b = k_o \exp[(1-\alpha)nf(E - E^o)] \qquad (4.7)$$

where k_o and E^o are the standard electron transfer rate constant and standard potential, respectively. $C_{Na^+}(0)$ is the concentration of Na$^+$ ions at the BASE/electrode interface. We assume that the interface concentration of Na$^+$ ions is equal to the bulk concentration in the BASE during electrode reaction process, since the concentration of mobile Na$^+$ ions in BASE is approximately 9M, and the diffusion rate of Na$^+$ in BASE is very high. P_{in} is the sodium vapor pressure at the interface. α is the charge transfer coefficient, and $f = F/RT$.

In AC impedance, a small AC perturbation signal is applied and the current and concentrations oscillate around steady-state values:

$$i = \bar{i} + \tilde{i} \qquad\qquad P_{in} = \bar{P}_{in} + \tilde{P}_{in} \qquad\qquad\qquad E = \bar{E} + \tilde{E} \qquad\qquad (4.8)$$

where $\quad \tilde{i} = I_0 \exp(j\omega t) \qquad\qquad \tilde{P}_{in} = P_0 \exp(j\omega t) \qquad\qquad \tilde{E} = E_0 \exp(j\omega t)$

Differentiation of equation (4.6) , gives

$$\frac{di}{dt} = nFA[-\alpha nfk_f C_{Na^+}(0) - (1-\alpha)nfk_b \frac{P_{in}}{RT}]\frac{dE}{dt} - nFA\frac{k_b}{RT}\frac{dP_{in}}{dt} \qquad\qquad (4.9)$$

Since $\qquad \dfrac{di}{dt} = \dfrac{d(\bar{i}+\tilde{i})}{dt} = \dfrac{d\tilde{i}}{dt} = j\omega\tilde{i}$, and the similar relationships exist for $\dfrac{dE}{dt}$

and $\dfrac{dP_{in}}{dt}$,

$$\frac{\tilde{i}}{nFA} = [-\alpha nfk_f C_{Na^+}(0) - (1-\alpha)nfk_b \frac{P_{in}}{RT}]\tilde{E} - \frac{k_b}{RT}\tilde{P}_{in} \qquad\qquad (4.10)$$

The interface impedance of pure metal electrode Z is

$$Z = -\frac{\tilde{E}}{\tilde{i}} \qquad\qquad (4.11)$$

from equations (4.10) and (4.11) , we obtain

$$Z = \frac{RT}{n^2 F^2 A \left[\alpha k_f C_{Na^+}(0) + (1-\alpha)k_b P_{in}/RT \right]}$$

$$+ \frac{k_b}{nF \left[\alpha k_f C_{Na^+}(0) + (1-\alpha)k_b P_{in}/RT \right]} \times \frac{\tilde{P}_{in}}{\tilde{i}} \tag{4.12}$$

Let

$$Z_f = \frac{RT}{n^2 F^2 A \left[\alpha k_f C_{Na^+}(0) + (1-\alpha)k_b P_{in}/RT \right]} = R_{ct} \tag{4.13}$$

$$Z_d = \frac{k_b}{nF \left[\alpha k_f C_{Na^+}(0) + (1-\alpha)k_b P_{in}/RT \right]} \times \frac{\tilde{P}_{in}}{\tilde{i}} \tag{4.14}$$

Z_f is the impedance due to the charge transfer reaction. At equilibrium, $\vec{i} = \overline{i} = i_o$, thus Z_f

turns into the charge transfer resistance R_{ct} , i.e. $Z_f = \dfrac{RT}{nFi_o} = R_{ct}$. Z_d is the impedance

related to the Na vapor pressure change with current, thus which is corresponding to the

Na transport in the porous electrode.

$$Z = Z_f + Z_d \tag{4.15}$$

Therefore, the interface impedance comes from the charge transfer and Na diffusion,

which is in excellent agreement with the experimental results.

In order to obtain $\dfrac{\tilde{p}_{in}}{\tilde{i}}$, reaction (4.5) is taken into account. Assuming this process

obeys first–order kinetics, the reaction rate is expressed as

$$v_2 = k_2 \frac{P_{in}}{RT} - k_{-2} \frac{P_{Na}}{RT} \tag{4.16}$$

and the change of sodium pressure at the interface with time is described as

$$\frac{dP_{in}}{RTdt} = \frac{i}{nFA} - k_2 \frac{P_{in}}{RT} + k_{-2} \frac{P_{Na}}{RT}$$

(4.17)

P_{Na} is the pressure of sodium at outside surface of the electrode.

At equilibrium, $i=0$ and $\frac{dP_{in}}{dt} = 0$,

$$P_{in} = \frac{k_{-2}}{k_2} P_{Na} = \frac{P_{Na}}{K_2}$$

(4.18)

where $K_2 = \frac{k_2}{k_{-2}}$, the equilibrium constant for reaction (4.5).

By introducing the alternating component, Eq(4.17) can be modified as

$$\frac{d(\overline{P}_{in} + \tilde{P}_{in})}{RTdt} = \frac{\overline{i} + \tilde{i}}{nFA} - k_2 \frac{\overline{P}_{in} + \tilde{P}_{in}}{RT} + k_{-2} \frac{P_{Na}}{RT}$$

(4.19)

by substitution of Eq. (4.8) and (4.18) into Eq. (4.19)

$$j\omega + k_2 = \frac{RT}{nFA} \frac{\tilde{i}}{\tilde{P}_{in}}$$

(4.20)

Substituting equation (4.20) into (4.14),

$$Z_d = \frac{1}{\frac{n^2 F^2 A}{R^2 T^2} \left[\alpha RTK_1 C_{Na^+}(0) + (1-\alpha)P_{in}\right] j\omega + \frac{n^2 F^2 A}{R^2 T^2} \left[\alpha RTK_1 C_{Na^+}(0) + (1-\alpha)P_{in}\right] k_2}$$

(4.21)

where $K_1 = \frac{k_f}{k_b}$, the equilibrium constant for reaction (4.4).

therefore,

$$Z = Z_f + Z_d = R_{ct} + \frac{1}{j\omega C_d + \frac{1}{R_d}}$$

(4.22)

where

$$C_d = \frac{n^2 F^2 A}{R^2 T^2} \left[\alpha R T K_1 C_{Na^+}(0) + (1-\alpha) P_{in} \right] \qquad (4.23)$$

$$R_d = \frac{R^2 T^2}{n^2 F^2 A k_2 \left[\alpha R T K_1 C_{Na^+}(0) + (1-\alpha) P_{in} \right]} \qquad (4.24)$$

Considering the series resistance R_s, the inductance of the lead L and a double-layer capacitance C_{dl}, the total impedance of the pure metal electrode is

$$Z_t = L + R_s + \frac{1}{j\omega C_{dl} + \dfrac{1}{R_{ct}}} + \frac{1}{j\omega C_d + \dfrac{1}{R_d}} \qquad (4.25)$$

The equivalent circuit corresponding to equation (4.25) is the same as Figure 4.8, which proves the validity of the equivalent circuit used to fit experimental results in this research. The more important thing is the physical meanings of the parameters in the equivalent circuit are understood.

Compare equation (4.13) to (4.24), it is found that

$$\frac{R_d}{R_{ct}} = \frac{k_b}{k_2} \qquad (4.26)$$

The experimental data have shown that R_d is greater than R_{ct} for pure metal electrodes, which means that k_b is greater than k_2. k_b is the potential-dependent rate constant for the backward reaction, while k_2 is the reaction rate constant for Na vapor transport into vacuum. In fact, reaction (4.5) is not a single reaction, and might include sodium vapor surface diffusion, desorption and diffusion in the pores of the electrode. Therefore, it is very complicated and strongly dependent on the properties of electrode itself, such as electrode morphology and Na diffusion coefficient on the electrode. In contrast, R_{ct} is

more related to the properties of the system, such as temperature and Na^+ concentration, based on the equation (4.13). This is in agreement with experimental results. For all tested pure metal electrodes, charge transfer resistances were very similar, since all electrode were measured at same temperature and using same BASE, while the diffusion resistances were highly variable.

Substituting equation (4.18) into (4.23), the following equation is obtained

$$C_d = \frac{n^2 F^2}{R^2 T^2} A \left[\alpha RT K_1 C_{Na^+}(0) + (1-\alpha) P_{Na} / K_2 \right]$$ (4.27)

It shows that the diffusion capacitor is not just related to sodium vapor diffusion, but also to the charge transfer process, since it consists of two items. If K_1, the equilibrium constant of the charge transfer reaction is large, and K_2, the equilibrium constant of sodium transport, is small, the electrode will have a large capacitance. A large K_1 means the charge transfer reaction can produce enough Na vapor, while small K_2 means the adsorbed Na vapor is difficult to transport through the electrode, therefore, the adsorbed Na vapor must accumulate in the electrode, or there is a lag-time of sodium concentration in the pore with respect to the current, which results in capacitive behavior. K_1 is only determined by potential and temperature, independent on the properties of individual electrode, thus a large diffusion capacitance is related to a small equilibrium constant of sodium transport process. Additionally, because $K_2 = \dfrac{P_{Na}}{P_{in}}$ and the sodium pressure P_{Na} at the electrode surface is only dependent on the temperature, the small K_2 means the vapor pressure on the interface is high. Therefore, the diffusion capacitance can be used to estimate the interface pressure of sodium vapor. For

example, a large diffusion capacitance indicates the interface vapor pressure of sodium is high. The significance of this discovery is the vapor pressure at interface, which is not directly measured by any experiment, could be estimated from impedance data.

According to EIS theory, for a RC loop, the point at the semicircle maximum corresponds to the frequency $\omega=1/RC$. Therefore,

$$\omega_d = \frac{1}{R_d C_d} \qquad (4.28)$$

By substituting Eq. (4.23) and (4.24) into (4.28),

$$\omega_d = k_2 \qquad (4.29)$$

ω_d can be extracted from EIS results and thus the value of the rate constant k_2 for sodium transport through the electrode is obtained. In order to find the relationship between k_2 and temperature, we measured the impedance at different temperatures for Ni electrodes and the results are shown in Figure 4.11. The relationship of k_2 with temperature obeys Arrhenius' law, indicating that although Na transport might include several steps, the entire process is controlled by a single activation energy.
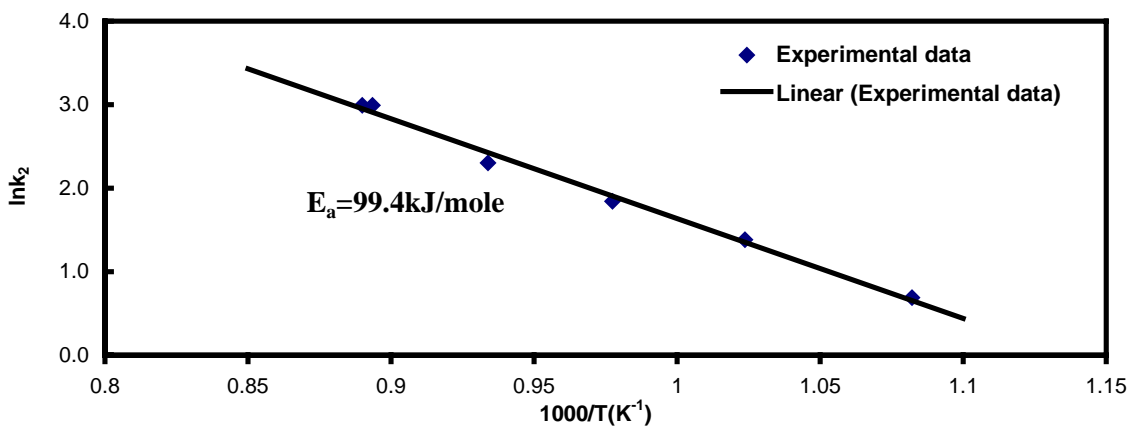
Figure 4.11. Arrhenius plot for sodium transport in the Ni electrode at SETC conditions.

4.3.3 Mixed Electrode Kinetic Mechanisms

Figure 4.12 shows the impedance spectra for different mixed ionic and electronic electrodes. It is found that they are similar in shape and can also be deconvoluted into two semi-circles. This implies the electrode process still consists of two steps, a charge transfer reaction (4.4) and sodium vapor transport reaction (4.5), which also includes sodium surface diffusion, desorption, and vapor transport. The difference with the pure metal electrode is the reaction sites, i.e. triple-phase boundaries, are not only at the electrode/BASE interface, but also within the electrode, since the sodium ions can transport into the electrode by the ionic conductor, and the produced sodium vapor doesn't have to transport through the entire electrode thickness to arrive at the electrode surface. Therefore, reactions (4.4) and (4.5) both occur at the interface and within the electrode.
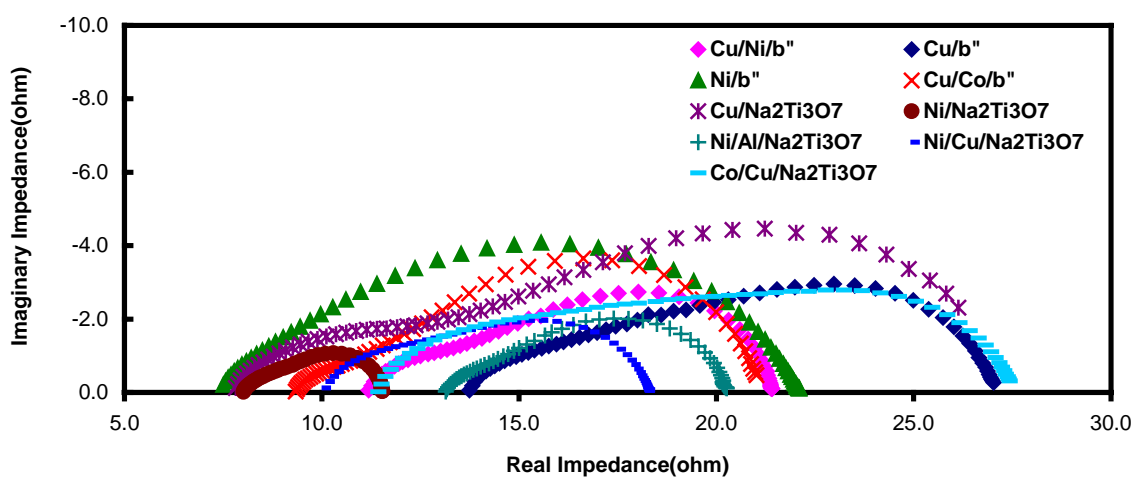
Figure 4.12. Impedance spectra of different MIEEs.

If the reactions occur at the interface, the current i_{in} is already described in Equation (4.6). If the reactions occur within the electrode, the current i_{el} is expressed by the equation (4.30)

$$i_{el} = \vec{i}_{el} - \overline{i}_{el} = nFA_{el}[k_f \sum_{x>0} C_{Na^+}(x) - \frac{k_b}{RT}\sum_{x>0} P_{el}(x)] \tag{4.30}$$

The total current produced by this electrode is

$$i = i_{in} + i_{el} = (\vec{i}_{in} - \overline{i}_{in}) + (\vec{i}_{el} - \overline{i}_{el})$$

$$= nFA_{in}[k_f C_{Na^+}(0) - k_b \frac{P_{in}}{RT}] + nFA_{el}[k_f \sum_{x>0} C_{Na^+}(x) - \frac{k_b}{RT}\sum_{x>0} P_{el}(x)] \tag{4.31}$$

where A_{in} is the total reaction area at the interface. It is assumed that every reaction site within the electrode has the same area, $A_{el,}$ which is the area of the single reaction site within the electrode. $C_{Na^+}(0)$ and P_{in} are still the concentration of Na^+ ions and sodium pressure at the interface, and $C_{Na^+}(0)$ is a constant. $C_{Na^+}(x)$ and $P_{el}(x)$ represent the Na^+ ions concentration and sodium vapor pressure at the reaction sites within the electrode, not at the interface. $C_{Na^+}(x)$ is a function of the location of reaction site and time, but in order to simply the situation, we assume it is a constant and equal to the Na^+ ion concentration in the sodium titanate.

Differentiation of equation (4.31) and combination with $\frac{di}{dt} = j\omega\tilde{i}$, yields

$$\tilde{i} = -[\alpha nf(\vec{i}_{in} + \vec{i}_{el}) + (1-\alpha)nf(\overline{i}_{in} + \overline{i}_{el})]\tilde{E} - \frac{nFk_b}{RT}[A_{in}\tilde{P}_{in} + A_{el}\sum_{x>0}\tilde{P}_{el}(x)] \tag{4.32}$$

The interface impedance of mixed electrode Z still consist of two parts, Z_f and Z_d,

$$Z = Z_f + Z_d \tag{4.33}$$

$$Z_f = \frac{1}{\alpha n f (\vec{i}_{in} + \vec{i}_{el}) + (1-\alpha) n f (\overleftarrow{i}_{in} + \overleftarrow{i}_{el})} \tag{4.34}$$

$$Z_d = \frac{k_b}{\alpha(\vec{i}_{in} + \vec{i}_{el}) + (1-\alpha)(\overleftarrow{i}_{in} + \overleftarrow{i}_{el})} \frac{A_{in}\tilde{P}_{in} + A_{el}\sum_{x>0}\tilde{P}_{el}(x)}{\tilde{i}} \tag{4.35}$$

Z_f is the charge transfer impedance. At equilibrium, $i=0$, $Z_f = \dfrac{RT}{nFi_0} = R_{ct}$. Z_d is the

impedance related to the Na transport in the porous electrode.

For a MIEE, if the reaction sites of reaction (4.5) are at the interface, the reaction rate is the same with equation (4.16); if the reaction sites are within the electrode, the rate is expressed as

$$v_2 = k_2 \frac{P_{el}(x)}{RT} - k_{-2} \frac{P_{Na}}{RT} \tag{4.36}$$

the change of sodium pressure at the interface with time is described as

$$\frac{dP_{in}}{RTdt} = \frac{i_{in}}{nFA_{in}} - k_2 \frac{P_{in}}{RT} + k_{-2} \frac{P_{Na}}{RT} \tag{4.37}$$

$$\frac{d\sum_{x>0}P_{el}(x)}{RTdt} = \frac{i_{el}}{nFA_{el}} - k_2 \frac{\sum_{x>0}P_{el}(x)}{RT} + k_{-2} \frac{P_{Na}}{RT} \tag{4.38}$$

At equilibrium, $i=0$ and $\dfrac{dP_{in}}{dt} = \dfrac{dP_{el}(x)}{dt} = 0$,

$$P_{in} = P_{el}(x) = \frac{P_{Na}}{K_2} \tag{4.39}$$

By introducing the alternating component, and substitution, it yields

$$j\omega + k_2 = \frac{RT}{nFA_{in}} \frac{\tilde{i}_{in}}{\tilde{P}_{in}} \tag{4.40}$$

$$j\omega + k_2 = \frac{RT}{nFA_{el}} \frac{\tilde{i}_{el}}{\sum\limits_{x>0} \tilde{P}_{el}(x)} \tag{4.41}$$

using the ratio rules on equation (4.40) and (4.41) produces

$$j\omega + k_2 = \frac{RT}{nF} \frac{\tilde{i}_{in} + \tilde{i}_{el}}{A_{in}\tilde{P}_{in} + A_{el}\sum\limits_{x>0} \tilde{P}_{el}(x)} = \frac{RT}{nF} \frac{\tilde{i}}{A_{in}\tilde{P}_{in} + A_{el}\sum\limits_{x>0} \tilde{P}_{el}(x)} \tag{4.42}$$

Substituting equation (4.42) into (4.35),

$$Z_d = \frac{1}{j\omega C_d + \dfrac{1}{R_d}} \tag{4.43}$$

where

$$
\begin{aligned}
C_d &= \frac{nF}{RTk_b}[\alpha(\vec{i}_{in} + \vec{i}_{el}) + (1-\alpha)(\bar{i}_{in} + \bar{i}_{el})] \\
&= \frac{n^2 F^2}{R^2 T^2}\left[\alpha RTK_1[A_{in}C_{Na^+}(0) + A_{el}\sum\limits_{x>0} C_{Na^+}(x)] + (1-\alpha)[A_{in}P_{in} + A_{el}\sum\limits_{x>0} P_{el}(x)] \right]
\end{aligned}
\tag{4.44}
$$

$$
\begin{aligned}
R_d &= \frac{1}{\dfrac{nF}{RTk_b}[\alpha(\vec{i}_{in} + \vec{i}_{el}) + (1-\alpha)(\bar{i}_{in} + \bar{i}_{el})]k_2} \\
&= \frac{R^2 T^2}{n^2 F^2 k_2\left[\alpha RTK_1[A_{in}C_{Na^+}(0) + A_{el}\sum\limits_{x>0} C_{Na^+}(x)] + (1-\alpha)[A_{in}P_{in} + A_{el}\sum\limits_{x>0} P_{el}(x)] \right]}
\end{aligned}
\tag{4.45}
$$

It is seen that C_d and R_d are not just related to sodium transport process, but also to the properties of charge transfer reaction, such as A_{in}, A_{el} and $C_{Na^+}(x)$.

Therefore, the mixed electrode impedance has the same form as a pure metal electrode, shown in equation (4.25), but every parameter has a different meaning. The equivalent circuit, Figure 4.8 is also useful for the mixed electrode spectrum. In the above deduction, $C_{Na^+}(x)$ is considered as a constant. In fact, for a real mixed electrode, $C_{Na^+}(x)$ generally changes with the location x and with time. Therefore, the impedance should be equal to equation (4.46).

$$Z = R_{ct} + \cfrac{1}{j\omega C_d + \cfrac{1}{R_d}} + \frac{RTk_f A_{el}}{\alpha(\vec{i}_{in} + \vec{i}_{el}) + (1-\alpha)(\overleftarrow{i}_{in} + \overleftarrow{i}_{el})} \frac{\sum_{x>0} \tilde{C}_{Na^+}(x)}{\tilde{i}} \qquad (4.46)$$

The third item in this equation corresponds to Na^+ ion transfer in the ionic conductor. It could be a line with a slope of 1, which corresponds to the semi-infinite line Warburg diffusion, or it also could be a semicircle in the Nyquist plot. In this case, the impedance spectrum includes three semicircles. Sometimes, the third semicircle is overlapped by the sodium vapor transport semicircle, i.e. they have very similar time constants. In this case, it is difficult to distinguish them and R_d extracted from this spectrum has errors.

Comparing R_{ct} for these two systems, equations (4.13) and (4.34), it seems that mixed electrode can have smaller R_{ct} values, since equation (4.34) has more items in the denominator. For a mixed electrode system, both metal and ceramic particles contact with BASE, and the ceramic contact area can not provide reaction sites, therefore, A_{in} should be smaller than that of the pure metal electrode, and thus i_{in} as well. Only when the i_{in} is similar for these two systems, or the i_{el} can compensate for this difference, will the mixed electrode system have a smaller charge transfer resistance than a pure metal

electrode system, which provides the theoretical interpretation for the experimental results of larger charge transfer resistance for a MIEE comparing to a pure metal electrode.

In order to obtain a small R_{ct} for the mixed electrode, keep A_{in} and A_{el} as large as possible. How to obtain a large A_{el} is related to the particle sizes and composition for both components, discussed in Chapter III, in which the particles of the same type (electronic conductor or ionic conductor) have to touch each other so that a network is formed through the electrode, and adequate contact between the particles of different types ensures that a large active reaction area is formed. A large A_{in} requires that the interface area should be occupied by metal particles as much as possible. Combining those two requirements, it is found that the ionic particles should form a tree type structure from the interface to surface, in which the root is on the interface, and branches are all through the whole electrode. If the interface areas are all occupied by the ionic particles, the two types of particles form more C clusters, this electrode will have a very large R_{ct}. Therefore, it can be concluded that the mixed electrode is more dependent on the microstructure.

For the mixed electrode system, equations (4.26) and (4.29) still work. However, if k_2 is needed to be evaluated from equation (4.29), it would be not as accurate as for the pure electrode system, because Na^+ ion transfer in the ionic conductor is not considered in the mixed electrode kinetics.

In this study, we also calculated another kinetic parameter, the charge transfer coefficient α, for the Ni/sodium titanate MIEE. It is calculated based on the Tafel

behavior of the electrode, described in equation (4.47), and we obtained α is equal to 0.34 at 1123K, shown in Figure 4.13.

$$\ln i = \ln i_0 - \alpha n f \eta \qquad (4.47)$$

α is an important parameter and related to a large number of equations and conclusions for AMTEC studies, but it has never been measured in the literature and is usually assumed to be equal to 0.5 in all AMTEC theory. Therefore, our experimental result of 0.34, not 0.5, would cause the correction of the equations and conclusions involving α. How α affects these equations and conclusions will be discussed in Chapter V.
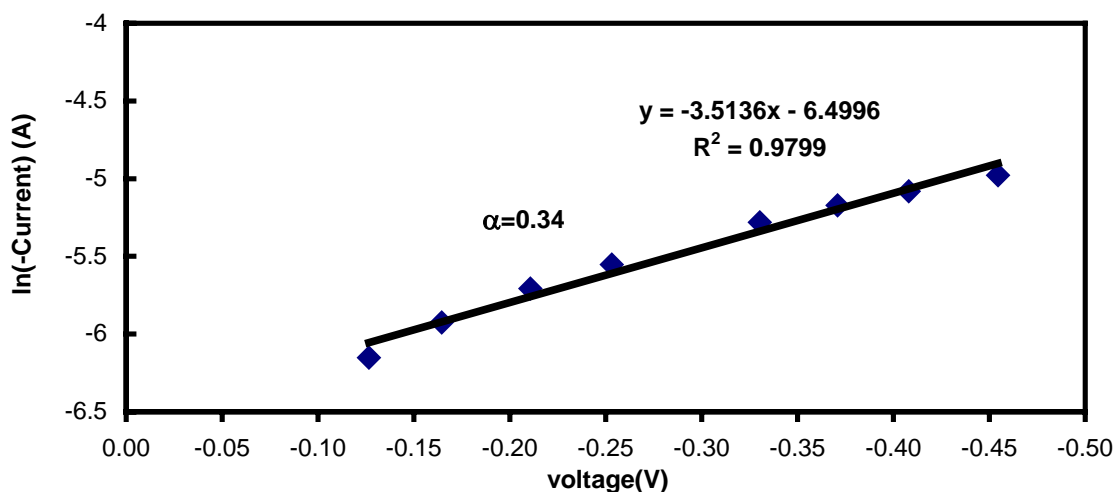
Figure 4.13. Cathode Tafel plot for Ni/sodium titanate electrode with 4/1mass ratios.

4.4 Summary and Conclusions

The conductivity has been measured for a sodium titanate mixture of $Na_2Ti_3O_7$ and $Na_2Ti_6O_{13}$ with a mass ratio of 1:2 at the AMTEC operating conditions. The average activation energy for the bulk and total conductivities are 0.87ev and 0.96ev, respectively. At AMTEC working temperatures (~1120K), the conductivity of the grain boundary is much higher than that of the bulk. Only about 10% of the total resistance is contributed by the grain boundary.

Theoretical expressions for the interface impedance of the electrode process have been derived to interpret the experimental results for both pure metal electrode and mixed electrode. For a pure metal electrode, the interface impedance consists of charge transfer resistance and sodium transport impedance, which is the transport resistance in parallel with the transport capacitance. For a mixed electrode, the electrode impedance consists of charge transfer resistance, sodium transport impedance and the impedance of sodium ion transfer in the ionic conductor of the electrode. The transport resistance and the capacitance are not only related to the transport process, i.e. the sodium vapor pressure at the interface or within the electrode, but also related to the charge transfer properties. For most of tested electrodes, the rate constant of sodium transport is smaller than that of sodium oxidation, based on the experimental results that the radius of semicircle at low frequency is generally larger than that at high frequency. For a pure metal electrode, a method is provided to estimate the sodium vapor pressure at the electrode/electrolyte interface by measuring electrode impedance and extracting the diffusion capacitance. The rate constant of sodium transport can also be calculated from

the impedance, which is equal to the frequency of the semicircle maximum point at low frequency range. Although sodium transport in the electrode includes several steps of adsorption, desorption and vapor transport in the pores, the entire process is controlled by a single activation energy of 99.4kJ/mol for a Ni electrode.

Although the mixed electrode extends the reaction area from the interface to the thickness of the electrode, it might have a larger charge transfer resistance, which depends on the microstructure of the electrode. A tree type structure for ionic particles could result in a small charge transfer resistance. Therefore, the mixed electrode is more dependent on the microstructure than the pure metal electrode.

CHAPTER V

PERFORMANCE STUDIES OF MIXED IONIC AND ELECTRONIC ELECTRODES

5.1 Introduction

As described in Chapter I, mixed electrodes are able to increase the reaction area and reduce electrode degradation by limiting the sintering behavior of the metal component. But the mixed electrode system is more complicated than the traditional single-phase metal electrode, since it has more components. The electrode performance is not only dependent on electrical resistance and sodium conduction, but also on the physical morphology of the electrode, such as the porosity, thickness, grain size, and quality of contact at the electrode-electrolyte interface, all which can affect the conduction of both electrons and sodium to and from the reaction sites.

Two parameters are generally used to evaluate the performance of an electrode, R_s and R_{act}. R_s is the series resistance, including all contact resistances. R_{act} is a combination of the charge transfer resistance and the sodium diffusion resistance. We used R_s and R_{act} to evaluate the performance of pure metal electrodes and MIEEs in Chapter III. But the evaluation is only valid when all these electrodes are measured at the same temperature including both electrode and sodium pool temperatures, because R_s and R_{act} vary with temperature. Therefore, researchers in JPL developed another parameter, B, to evaluate electrode performance independent of the electrode and sodium pool temperature.[36] B is the normalized exchange current density, which is normalized

to the sodium collision rate and reaction rate at unit activity of sodium. The units of B are $AK^{1/2}/(m^2 Pa)$ or $AK^{1/2}/N$ and it is calculated using equation (5.1).

$$B = \frac{J_o^o T_{el}^{1/2}}{P_{el}} \qquad (5.1)$$

In this equation, T_{el} and P_{el} are the temperature and sodium pressure at the electrode, j_o^o is the exchange current at an equilibrium potential obtained with saturated sodium vapor in contact with the electrode, defined by researchers in JPL. B is a sensitive measurement of the electrode performance. Large changes in B reflect relatively small changes in electrochemical cell performance until the exchange current drops significantly. The research at JPL indicated that the B value is approximately independent of electrode temperature, but our experimental results did not support this claim.

In the derivation of equation (5.1), the charge transfer coefficient α is assumed equal to 0.5, but some experimental results indicated that α has significant scatter from 0.3 to 0.7.[107] Our experimental results showed that $\alpha \approx 1/3$ at 1123K for the Ni/sodium titanate electrodes in Chapter IV. The value of α change will result in the change of B value. Since B is the main parameter used to evaluate AMTEC electrode performance, it is worth understanding its validity and the effect of α on B.

In this chapter, two kinds of MIEEs were tested and discussed. One is metal mixed with β″-alumina and the other is metal mixed with sodium titanate. For all tested electrodes, the impedance spectra were measured, B values were calculated, electrode performance was evaluated and the microstructures were observed before and after

electrodes testing in SETCs. Finally, the effect of the charge transfer coefficient α on B was discussed.

5.2 Experimental

The following chemicals were used as purchased:

Nickel powder 2.2~3.0μm(99.9%, Alfa Aesar)

Nickel powder 3~7μm(99.9%, Alfa Aesar)

Nickel powder 5~15μm(99.8%, Alfa Aesar)

Aluminum powder 3.0~4.5μm (97.5%, Alfa Aesar)

Cobalt powder ~1.6μm (99.8%, Alfa Aesar)

Cupper powder 1~1.5μm (99%, Alfa Aesar)

Sodium titanate powder(99.7%, Strem chemicals Inc)

For metal/β″-alumina electrodes, W/β″-alumina, Cu/β″-alumina, Ni/β″-alumina, Cu/Ni/β″-alumina and Cu/Co/β″-alumina were tested. Some of them were fabricated by electrophoresis in Ionotec, England and others were deposited by flame spraying in Hitemco, Houston.

For metal/sodium titanate electrodes, Ni/sodium titanate, Cu/sodium titanate, Ni//Cu/sodium titanate, and Co/Cu/sodium titanate were tested. All metal/sodium titanate electrodes were deposited by flame spraying deposition technique in Hitemco or Alamo Supply, Houston. The detailed electrode compositions and experiment durations are listed in appendix B.

5.3 Results and Discussion

5.3.1 TiN Electrode

TiN electrodes were examined in this research as a reference for evaluating the performance of other electrodes, since it is the current standard AMTEC electrode. The impedance spectra of these electrodes exhibit the R_{act} increased with experiment time rapidly, shown in Figure 5.1(a). This trend is clearer in the plot of B value vs. time, shown in Figure 5.1(b), which includes results for several TiN electrodes. It is found that TiN electrodes performed very well initially, and then degraded rapidly with time. The final B value is around 10 after 20 days of testing. This rapid significant degradation is the reason why we need to discover new electrode materials to improve the AMTEC electrode performance and lifetime.

5.3.2 Metal/β″-alumina MIEEs

W/β″-alumina MIEEs. — Metal W and its alloys were studied as AMTEC electrodes, and displayed notable performance. Thus, we selected it to fabricate a mixed electrode with β″-alumina. These electrodes have been tested with mass ratios of W to β″-alumina of 1/1, 3/2, 3/1, and 4/1. They were fabricated by electrophoresis at Ionotec, England. Unfortunately, the adhesion of the electrode film to BASE was very low, which resulted in poor performance for most tests of these electrodes. The sample with 3/1 ratios performed better. Figure 5.2(a) shows its impedance spectra measured at 304°C pool temperature and 904°C electrode temperature.
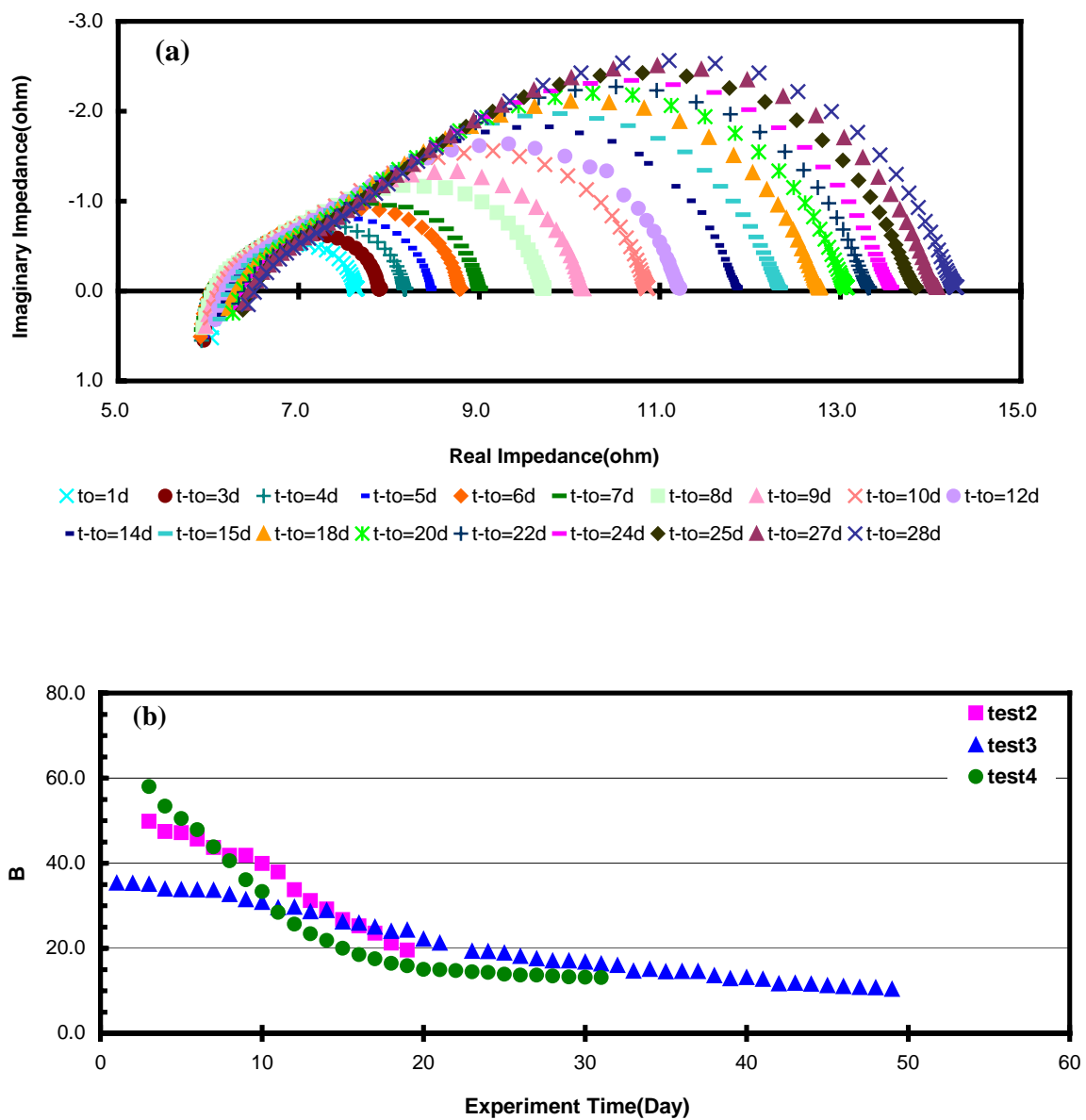
Figure 5.1. a) The impedance spectra of TiN electrodes. b) *B* value versus experiment time.

These spectra can be deconvoluted into two depressed semi-circles, one related to the charge transfer process at high frequency range, and the other related to sodium diffusion in the electrode at low frequency range. It is found that the high frequency circle (the charge transfer circle) is very depressed, compared to the normal impedance spectra of a MIEE. This phenomenon could result from surface roughness or varying thickness or composition of the electrode film. The depressed semicircle is indeed the arc of a circle with the center some distance below the x-axis. For a very smooth surface, the circle is an exact semicircle, i.e., the center of the circle is on the x-axis. When the surface roughness increases, the center of the circle moves below the x-axis.[86,105] A highly depressed circle corresponds to a very rough, fractal surface. Therefore, our W/β″-alumina spectra reflect a rough electrode surface, which is consistent with the SEM observations.

The spectra also illustrate that R_{act} increases with experiment time, which indicates that this electrode degrades rapidly. B values of this electrode are as low as 5, shown in Figure 5.2(b), which is much lower than that of the standard TiN electrode.

Figure 5.3 includes the SEM images of this sample before testing in the SETC. The raw mixed materials have 75% W by mass, but these images reveal an inadequate amount of W deposited into the electrode, which suggests that the electrophoresis deposition technique did not work well for W/β″-alumina mixture deposition. This lack of W probably played a major role in the poor performance of the electrodes.
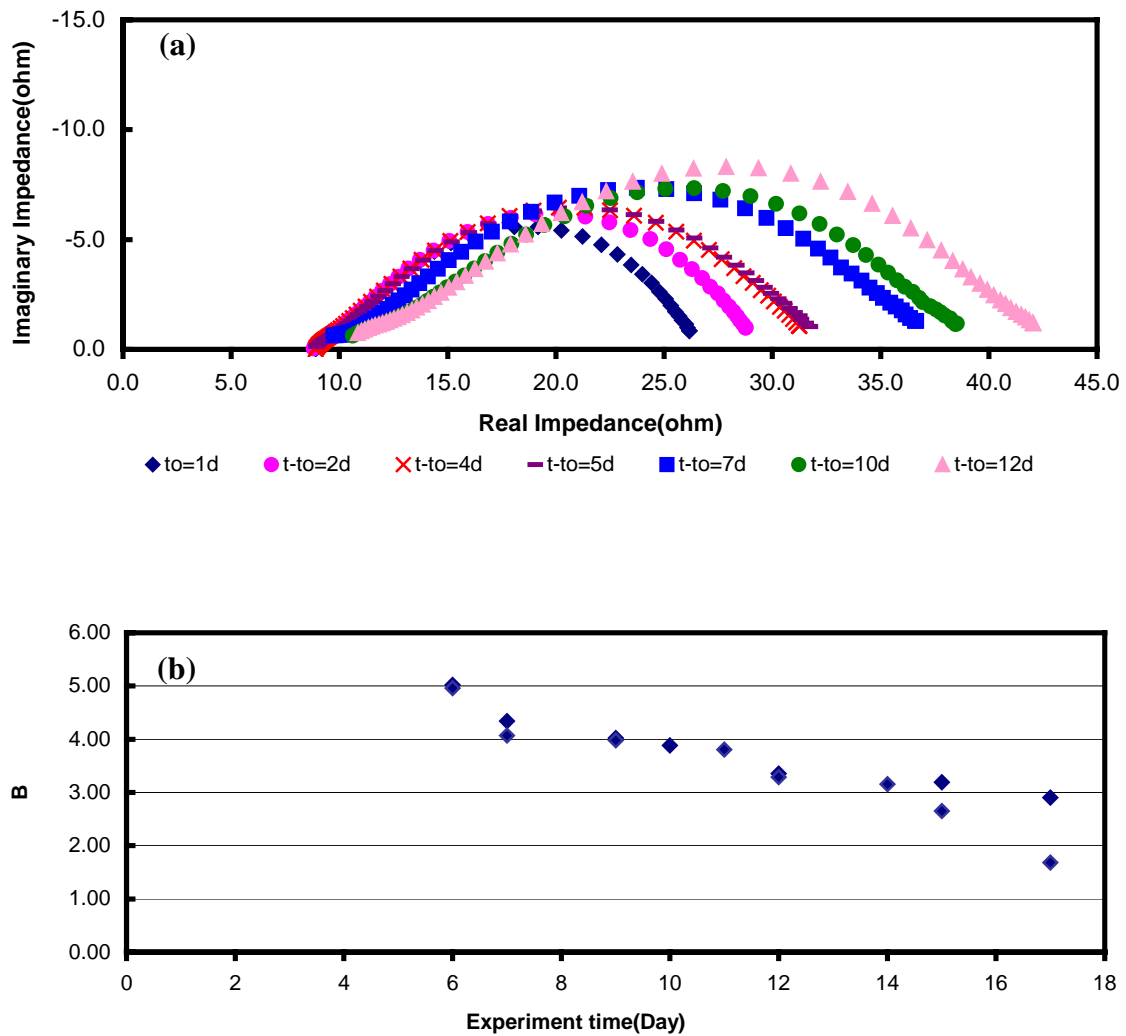
Figure 5.2. a) The impedance spectra of W/β″-alumina electrode with W/β″ ratios of 3/1. b) *B* value versus experiment time.

Pre-test sample ×2000 SE image   ×2000 Ni x-ray map

×2000 Al x-ray map   ×2000 W x-ray map
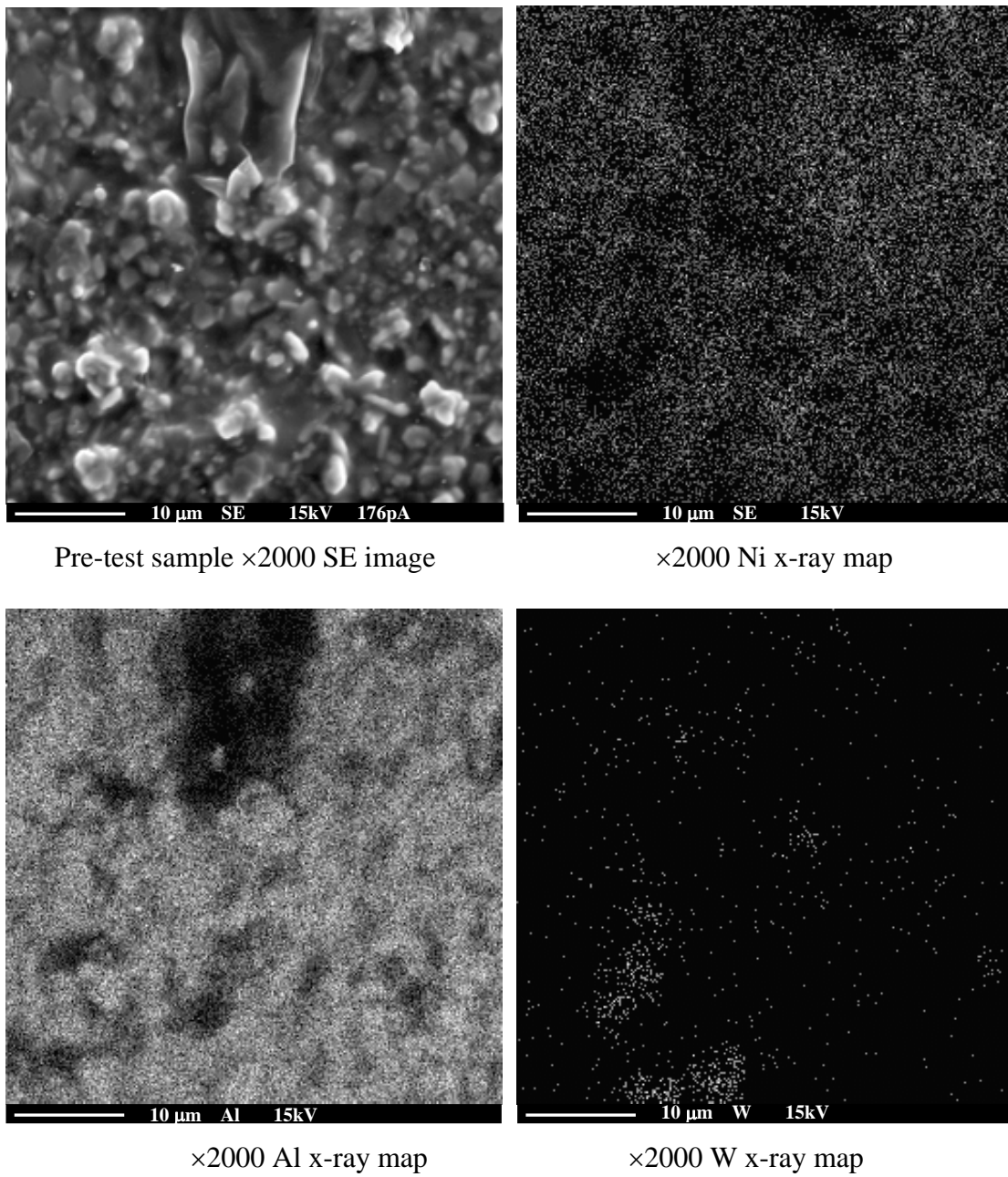
Figure 5.3. SEM images of W/β″-alumina sample with W/β″ ratios of 3/1 before testing in the SETC.

Cu/β″-alumina MIEEs. — Due to the high electrical conductivity and thermodynamical stability at AMTEC conditions, metal copper is an alternative to Ni as the metal component of a MIEE. Cu/β″-alumina electrodes were tested in this research with the ratio of Cu to β″-alumina of 1/1 and fabricated by flame spraying deposition technique. The impedance spectra, shown in Figure 5.4(a), were measured at 855^oC electrode temperature and $294\text{-}300^oC$ pool temperature. Due to vacuum pump problems, this test was run only a few days.

The spectrum consists of two depressed semi-circles, the high frequency charge transfer circle and the low frequency diffusion circle, which is in agreement with impedance spectra of normal mixed electrodes as discussed in Chapter IV. Thus the deduced electrode kinetics is also useful for this electrode.

The spectra show the R_{act} decreases with time, meaning the electrode matures with time. Deconvoluting these spectra, the charge transfer resistance and diffusion resistance are obtained, shown in Figure 5.4(b). It is found that the value of R_{ct} is very close to R_d value for this electrode. Such large R_{ct} could due to insufficient amounts of Cu in this electrode, thus increasing the mass percentage of Cu may reduce it. The kinetics equation (4.26) proposed in Chapter IV displays the reaction rate constant of sodium oxidation k_b is close to rate constant of sodium vapor diffusion k_2, if R_{ct} is similar to R_d.

The B value, shown in Figure 5.4(c) is around 8, which is lower compared to the standard TiN electrode. Therefore, the performance of Cu/β″-alumina electrode is not satisfied with AMTEC requirements. But compared to the W/β″-alumina electrode, Cu/β″-alumina performs slightly better.
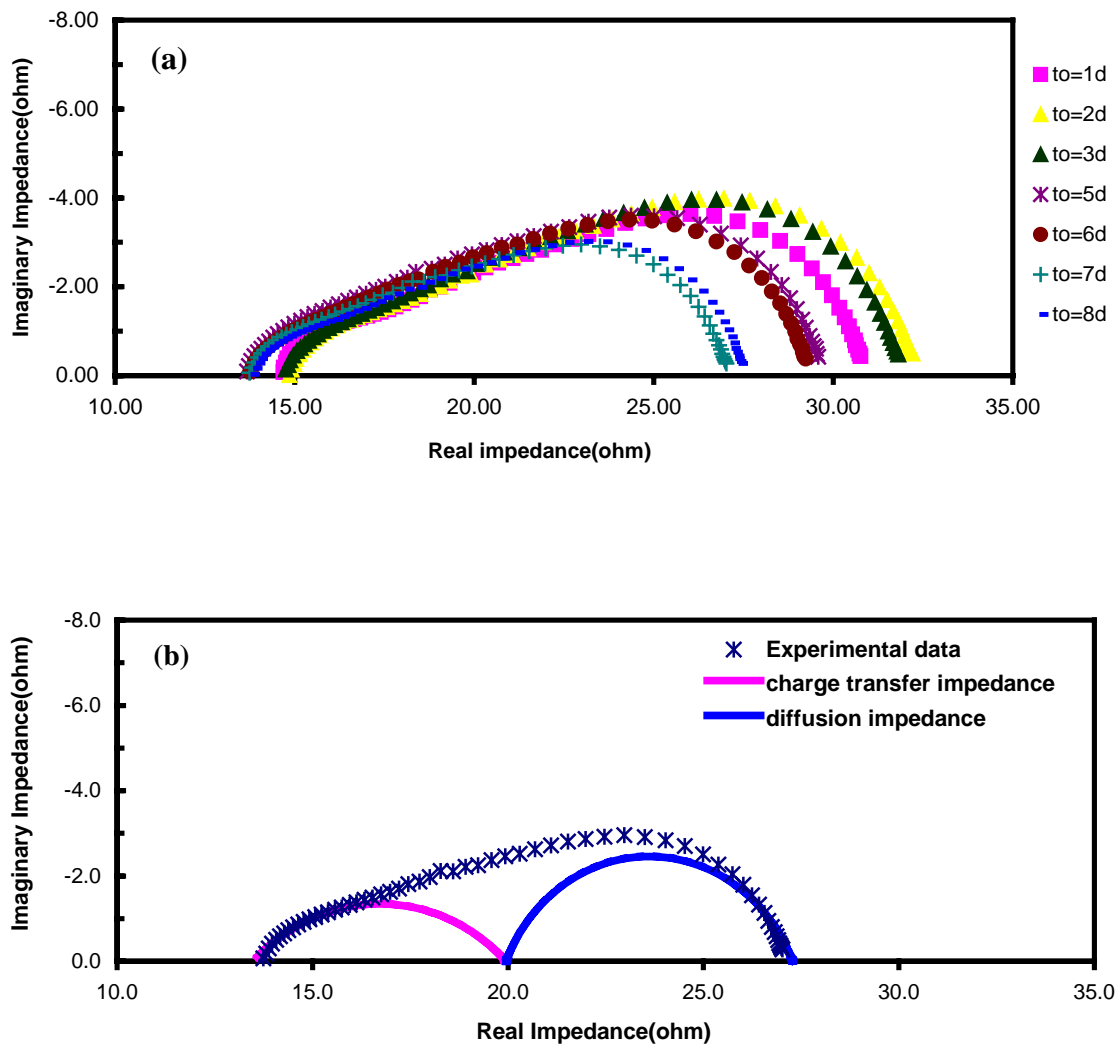
Figure 5.4. a) The impedance spectra of Cu/β″-alumina electrode with Cu/β″ ratio of 1/1. b) The impedance spectrum measured on t-to=7d, and its deconvoluted spectra for charge transfer and sodium transport processes c) *B* value versus experiment time.
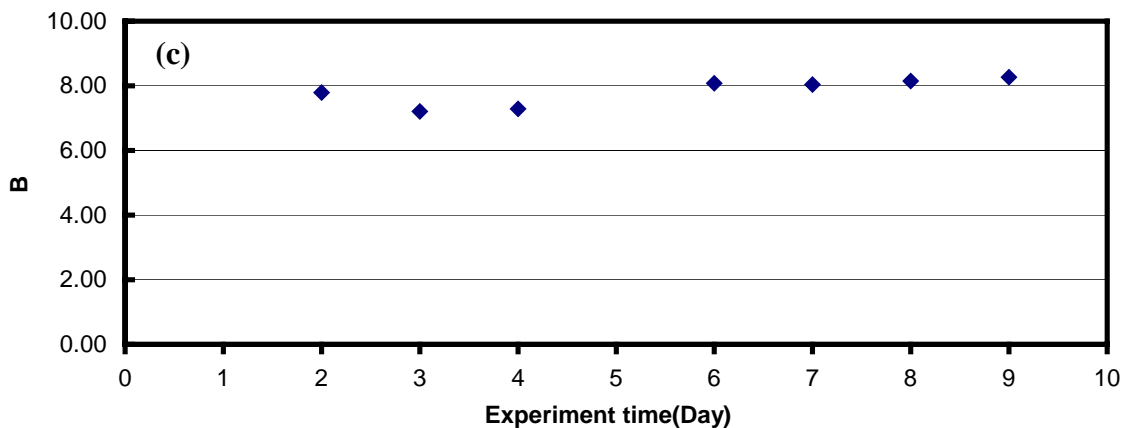
Figure 5.4. (Continued)

The SEM images in Figure 5.5 show the physical morphology of this electrode before and after testing in the SETC. For the original pre-test sample, its microstructure is basically satisfactory, with Cu distributed uniformly and close to the desired amount. The porosity in the electrode is also appropriate. This means the flame spray deposition technique works for the Cu/β″-alumina mixture deposition. The SEM images of the post-test sample reveal that the particle size of Cu is significantly increased compared to the microstructure of the original sample. Since this sample was only tested 10 days in the SETC, such large change of Cu particles indicates its grain growth rate is very significant, which could lead to very rapid degradation. Therefore, we believe the Cu/β″-alumina electrode is not a good electrode for AMTEC operation.

Pre-test sample ×500 BSE image   ×2000 BSE image

×2000 Cu x-ray map   ×2000 Al x-ray map

(a)

Figure 5.5. SEM images of Cu/β″-alumina sample with Cu/β″ ratio of 1/1, a) before and b) after testing in the SETC.

Post-test sample ×500 BSE image

×2000 BSE image

×2000 Cu x-ray map

×2000 Al x-ray map

(b)

Figure 5.5. (Continued)

Ni/β″-alumina MIEEs. — These electrodes have been fabricated by both electrophoresis and flame spraying deposition techniques, but the electrophoretically deposited electrode films were very thin and adhered poorly to the BASE, which resulted in poor performance. Flame spraying deposited electrode displayed better adhesion and higher performance. Therefore, the behaviors of the electrodes deposited by flame spraying are analyzed here. We tested these electrodes with Ni to β″-alumina ratios of 1/1, 3/2, and 3/1. Based on the experimental data, the best performance belongs to the electrode with the Ni/β″ ratios of 3/1. Its impedance spectra are shown in Figure 5.6(a), measured at 302°C pool temperature and 850°C electrode temperature.

For this electrode, the charge transfer resistance is much smaller than the diffusion resistance, which means sodium diffusion in this electrode is the rate limiting step. Additionally, the impedance measured on Jan 5th suddenly increased, which is mainly due to an increase of the diffusion impedance, shown in Figure 5.6(b). This could result from a reduction of electrode porosity during the test.

The initial B is around 15 for Ni/β″ electrode, shown in Figure 5.6(c). Compared to the Cu/β″ electrode, the Ni/β″ electrode displayed a much smaller R_{ct}, but a larger R_d. Thus, the rate constant k_2 of the sodium vapor transport reaction (4.5) is smaller than that of Cu/β″ electrode, which means sodium transport is more difficult in the Ni/β″ electrode than the Cu/β″ electrode. However, the apparent charge transfer resistance R_{act} is similar for both electrodes, which are around to 14Ω. The B values for Ni/β″ electrode are slightly larger than that of Cu/β″ electrode, which indicates that these two electrodes have the similar performance.
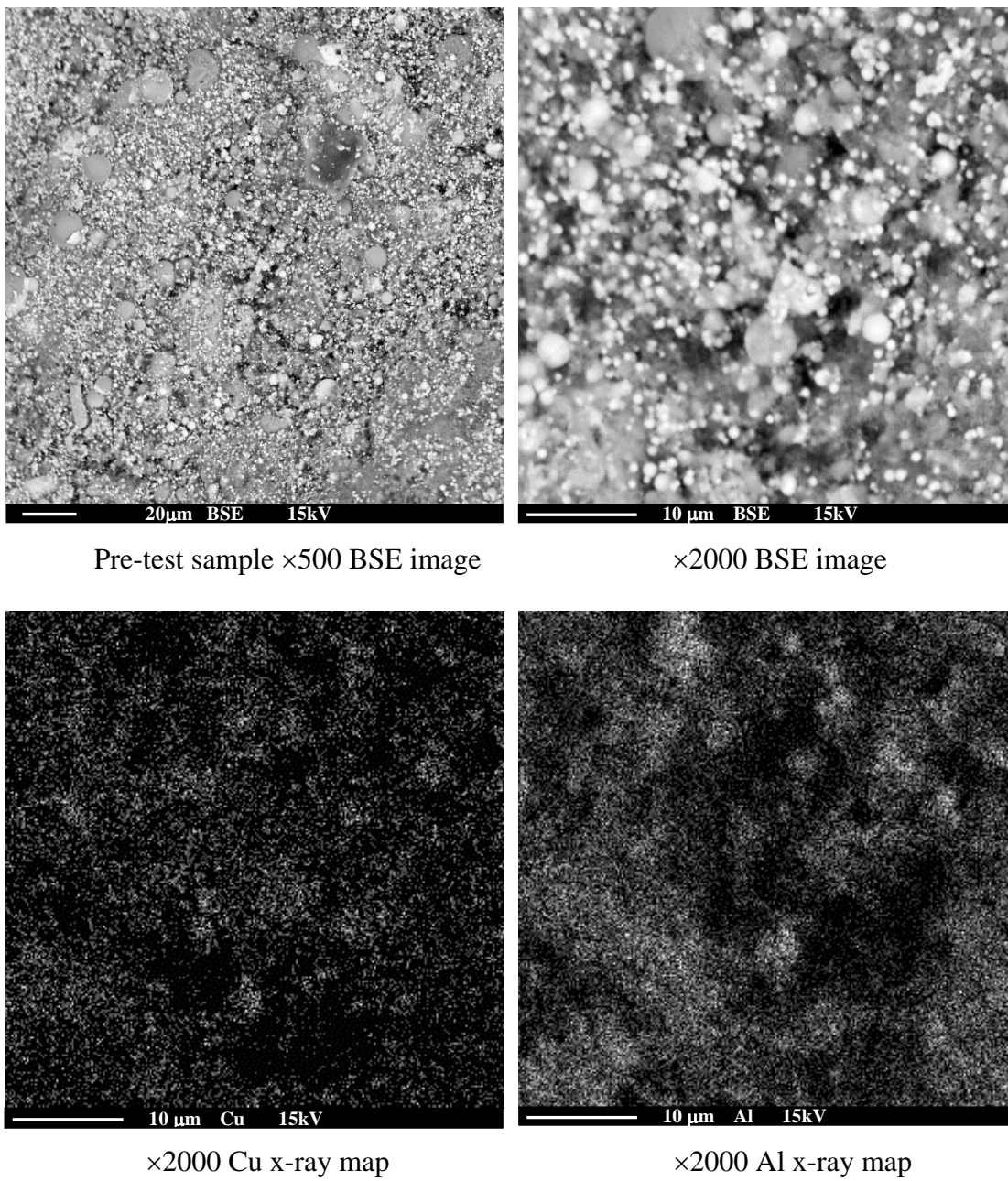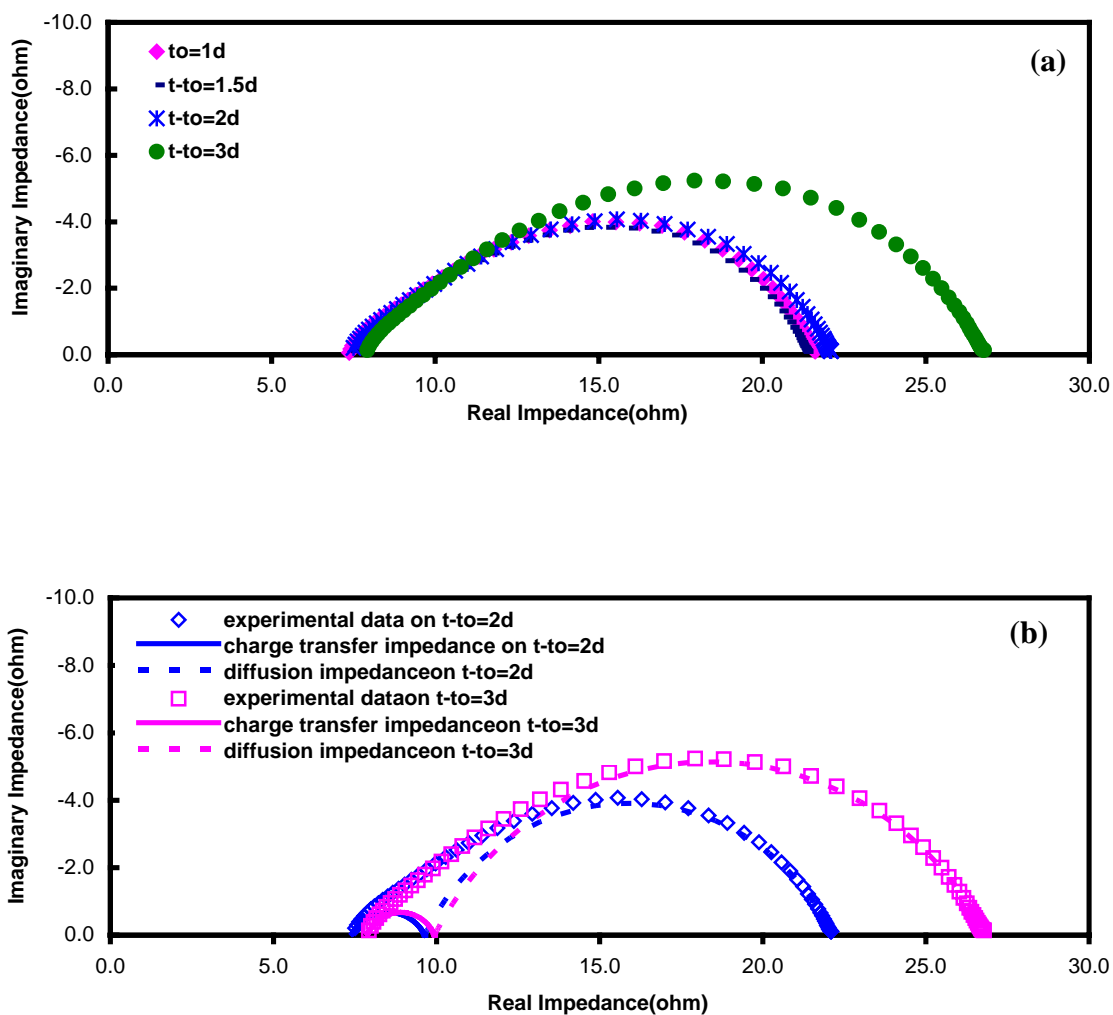
Figure 5.6. a) The impedance spectra of Ni/β″-alumina electrode with Ni/β″ ratios of 3/1. b) The impedance spectra measured on t-to=2d and 3d, and their deconvoluted spectra for charge transfer and sodium transport processes. c) B value versus experiment time.
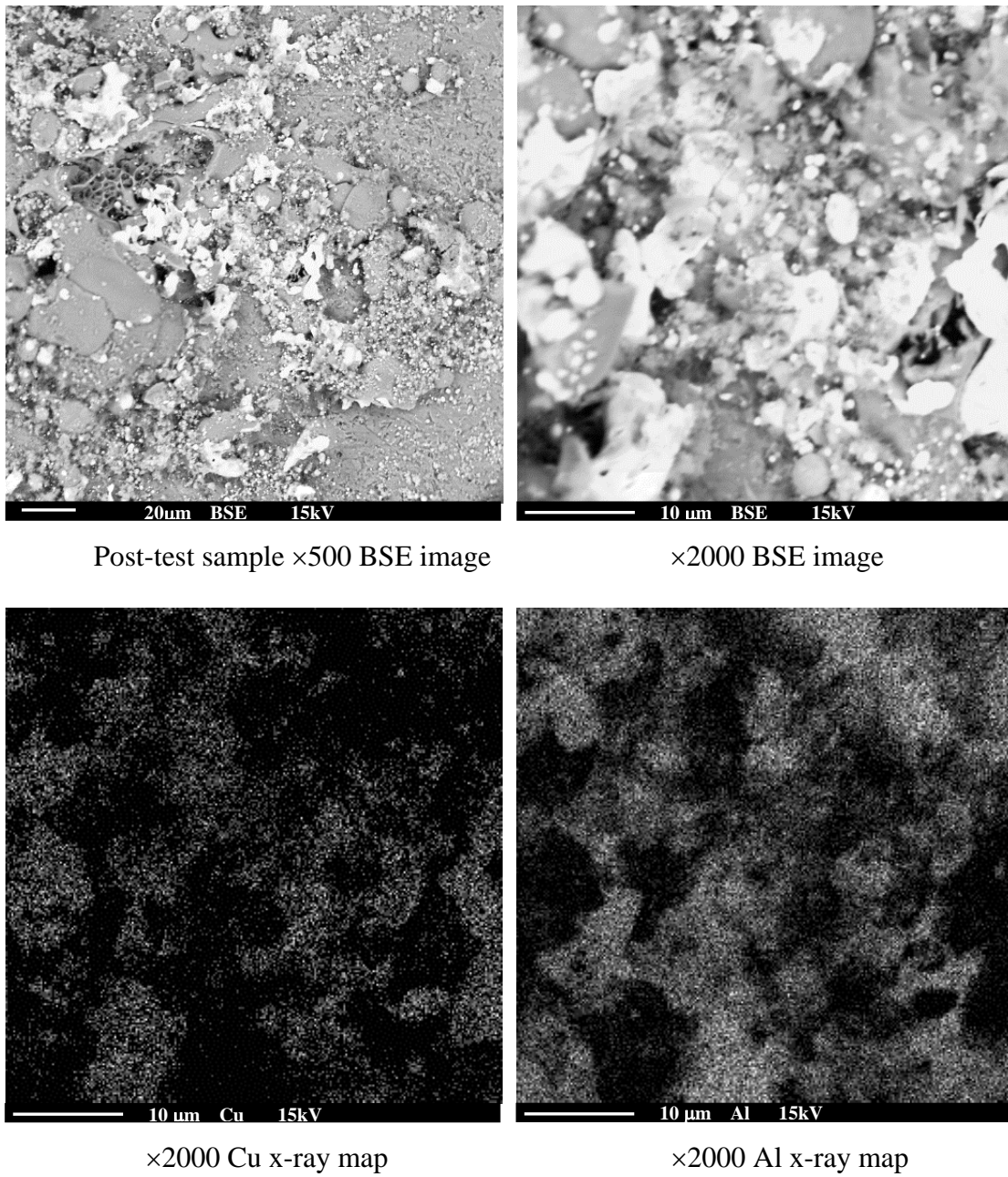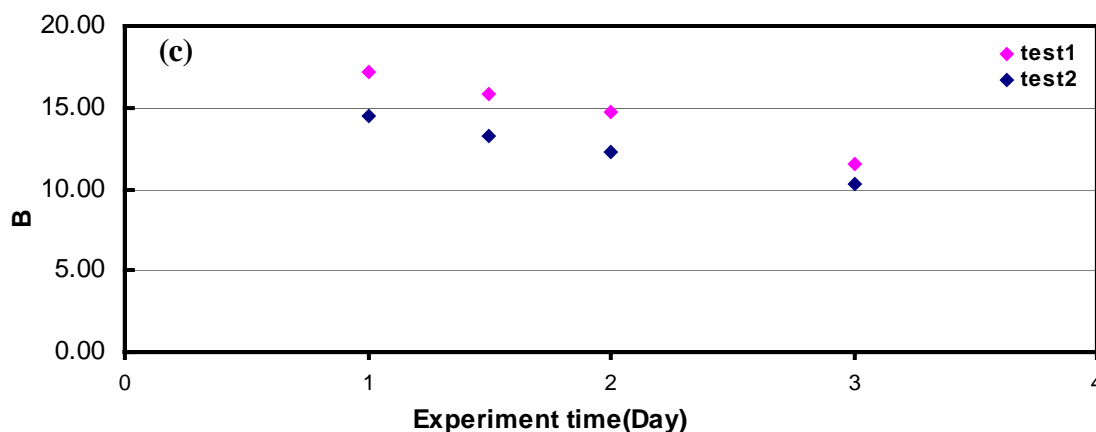
Figure 5.6. (Continued)

Figure 5.7 displays the microstructure of a tested Ni/β″-alumina electrode. It illustrates that grain coalescence for both Ni and β″-alumina particles. With the sample testing in the high temperature SETC, grain coalescence occurred, which reduced the electrode porosity and then made the sodium transport more difficult. At the beginning of this process, it would not significantly affect the number of reaction sites, thus the charge transfer resistance change slightly, which could explain the significant increase of the diffusion resistance on Jan 5th.

Ni particles coalesced and formed a network from the current collector to the interface of BASE. This interaction improves the electrode conductivities for both ionic and electronic. Also, the networks of Ni and β″-alumina were interwoven, which enlarges the reaction area. This behavior could interpret the small charge transfer resistance for Ni/β″-alumina electrode.
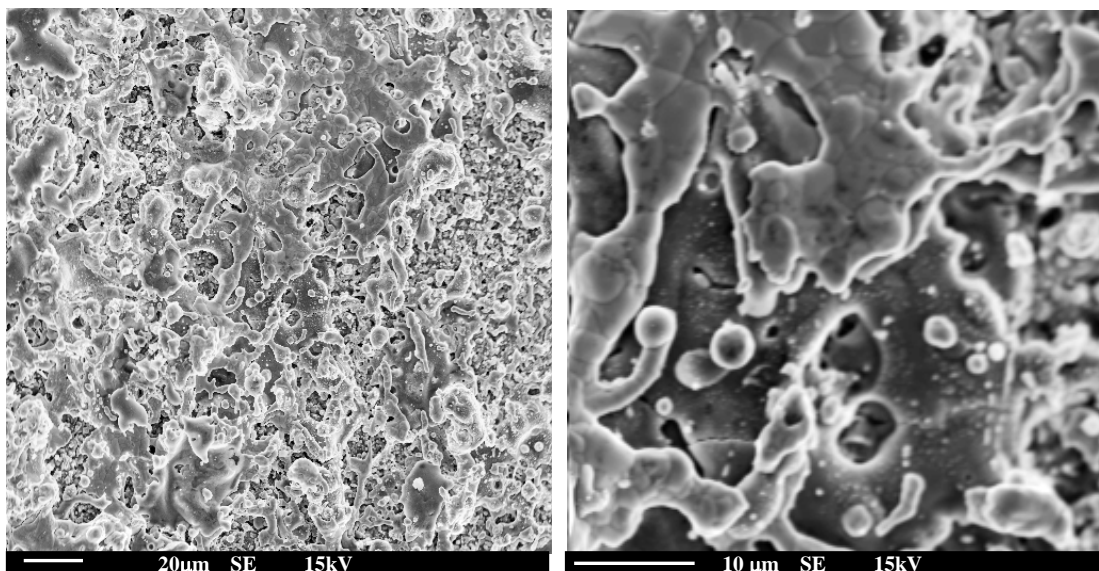
Post-test sample ×500 SE image   ×2000 SE image
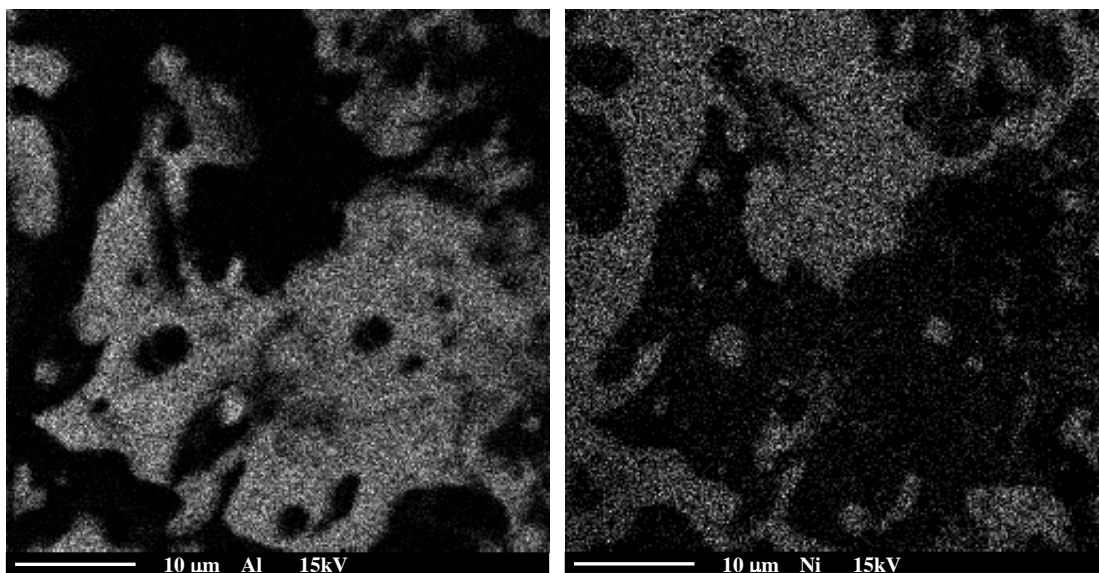
×2000 Al x-ray map   ×2000 Ni x-ray map

Figure 5.7. SEM images for Ni/β″-alumina sample with Ni/β″ ratios of 3/1 after testing in the SETC.

Ni/Cu/β″-alumina MIEEs. — In these electrodes, Cu is added as the second metal in order to improve the adhesion of the electrode film, because Cu/β″-alumina electrode displayed a good adhesion. For the Ni/β″-alumina electrode with the Ni/β″ ratios of 3/1 discussed previously, if half of its Ni is replaced by Cu, it forms Ni/Cu/β″-alumina electrodes with 3/3/2 ratios of Ni to Cu to β″. These electrodes were tested at 855°C electrode temperature and 295°C sodium pool temperature.

The impedance spectra and deconvoluted spectra of this Ni/Cu/β″ electrode are shown in Figure 5.8 (a) and (b), respectively. Compared Figure 5.8(b) to the Cu/β″ electrode spectrum, Figure 5.4(b), we found that the charge transfer resistance R_{ct} of Ni/Cu/β″ electrode is reduced, but their diffusion resistance R_d is similar. Compared to Ni/β″-alumina electrode, Figure 5.6(b), the R_{ct} of Ni/Cu/β″ electrode is increased, while R_d is decreased.

Combining these results, we found that the electrode containing Cu had a small diffusion resistance, while the electrode containing Ni had a small charge transfer resistance and with the amount of Ni component increase, R_{ct} decreases; with the Cu amount increase, R_d roughly decreases. It seems that Cu particles are more involved in sodium transport process, while Ni particles contribute more to the charge transfer reaction. k_2 is larger in the electrode having Cu particles, which may suggest that the sodium vapor diffusion or desorption on Cu particles is easier than on Ni particles.

The *B* values for this electrode are similar to that of Cu/β″ and Ni/β″ electrodes. Therefore, it is concluded that Ni/Cu/β″ electrode did not make progress with performance compared to Cu/β″ or Ni/β″ electrodes.

The SEM images of Ni/Cu/β″ electrode before and after the test are shown in Figure 5.9(a) and (b). The SEM images of pre-test sample show that the Ni, Cu and β″ were all deposited on the BASE with the desired mass ratio and they basically distributed uniformly over the whole electrode, which means that flame spraying is suitable for depositing a mixture with multiple components. The images of the post-test sample demonstrated that metal and ceramic particles both grew during the SETC test. Each type of particles connected and formed networks, which limited the further growth of grains. The grain boundaries still can be seen in this sample. Therefore, the extent of the grain growth is smaller than that of the pure metal electrode. It is also found that Ni and Cu particles coexistence in all images. For example, Ni and Cu are both present in the "key" shaped particles at the center of the SE image in Figure 5.9(b). This behavior is not observed for other electrodes with two metals. The most possible reason is the metal Ni and Cu alloyed during the test.
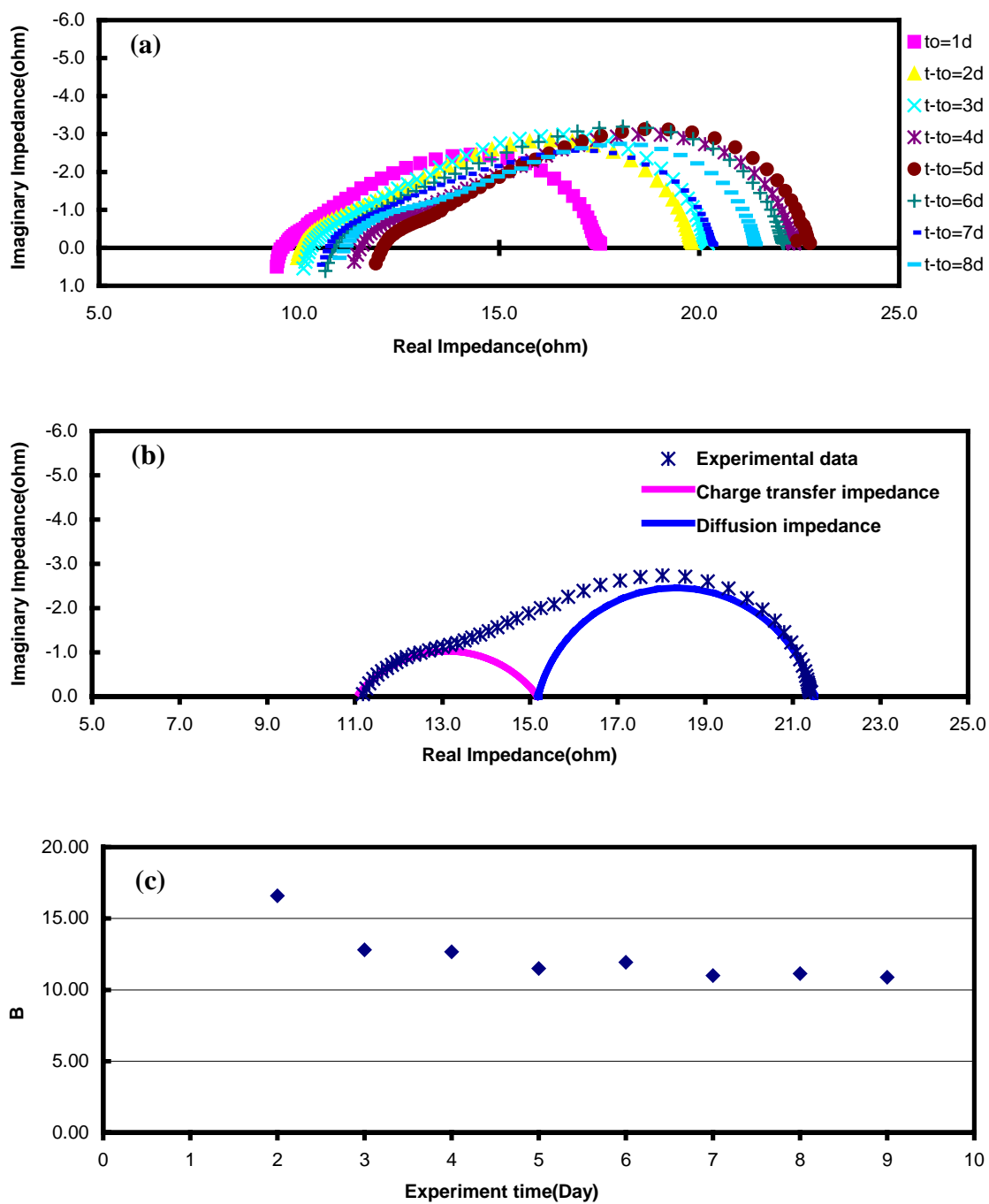
Figure 5.8. a) The impedance spectra of Ni/Cu/β′′-alumina electrode with Ni/Cu/β′′ ratios of 3/3/2. b) The impedance spectrum measured on t-to=8d, and its deconvoluted spectra for charge transfer and sodium transport processes. c) *B* value versus experiment time.

Pre-test sample ×2000 BSE image

×2000 Al x-ray map

×2000 Ni x-ray map

×2000 Cu x-ray map
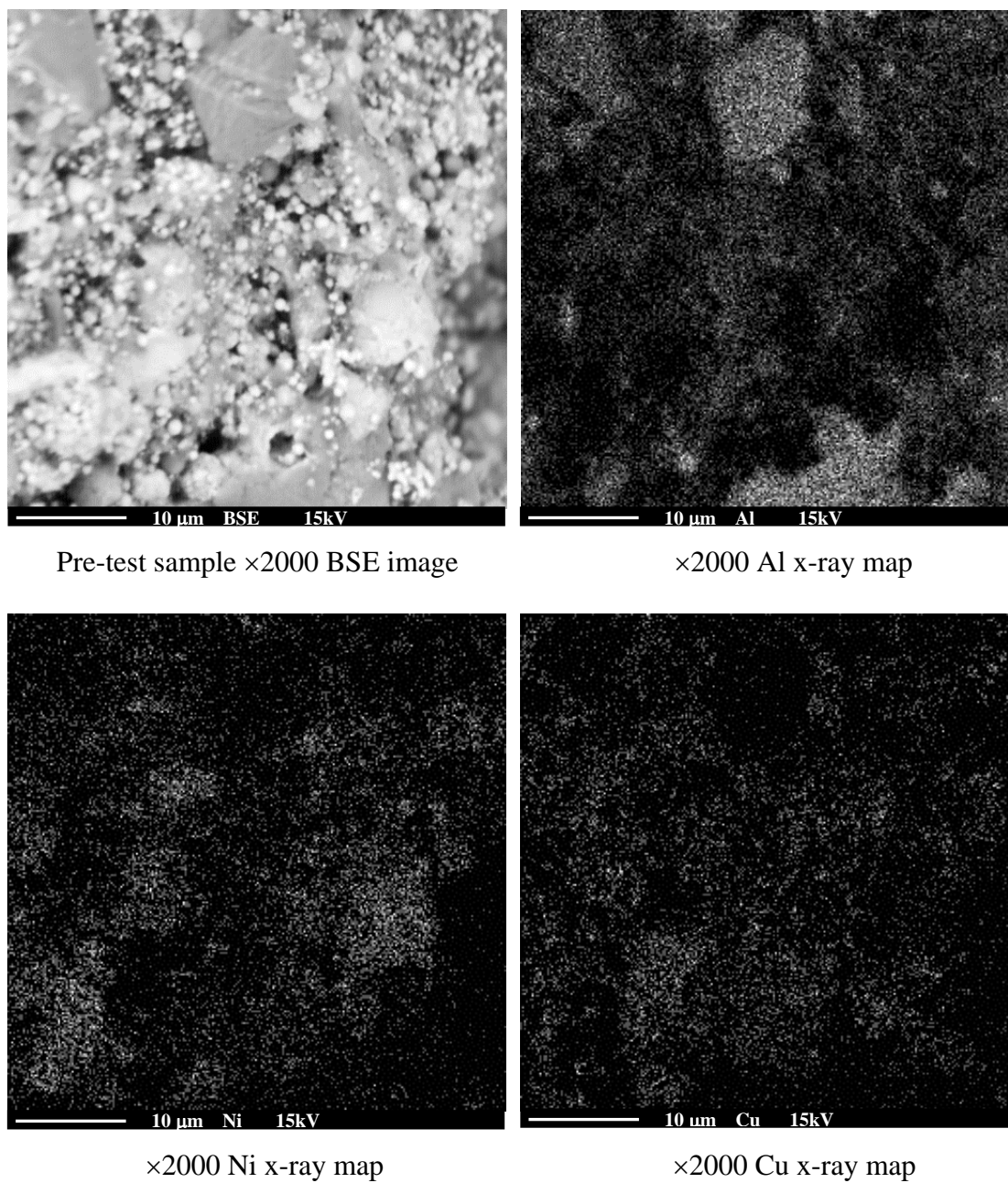
(a)

Figure 5.9. SEM images for Ni/Cu/β″-alumina sample with Ni/Cu/β″ ratios of 3/3/2 a) before and b) after testing in the SETC.

Post-test sample ×2000 BSE image

×2000x Al x-ray map

×2000 Cu x-ray map

×2000 Ni x-ray map
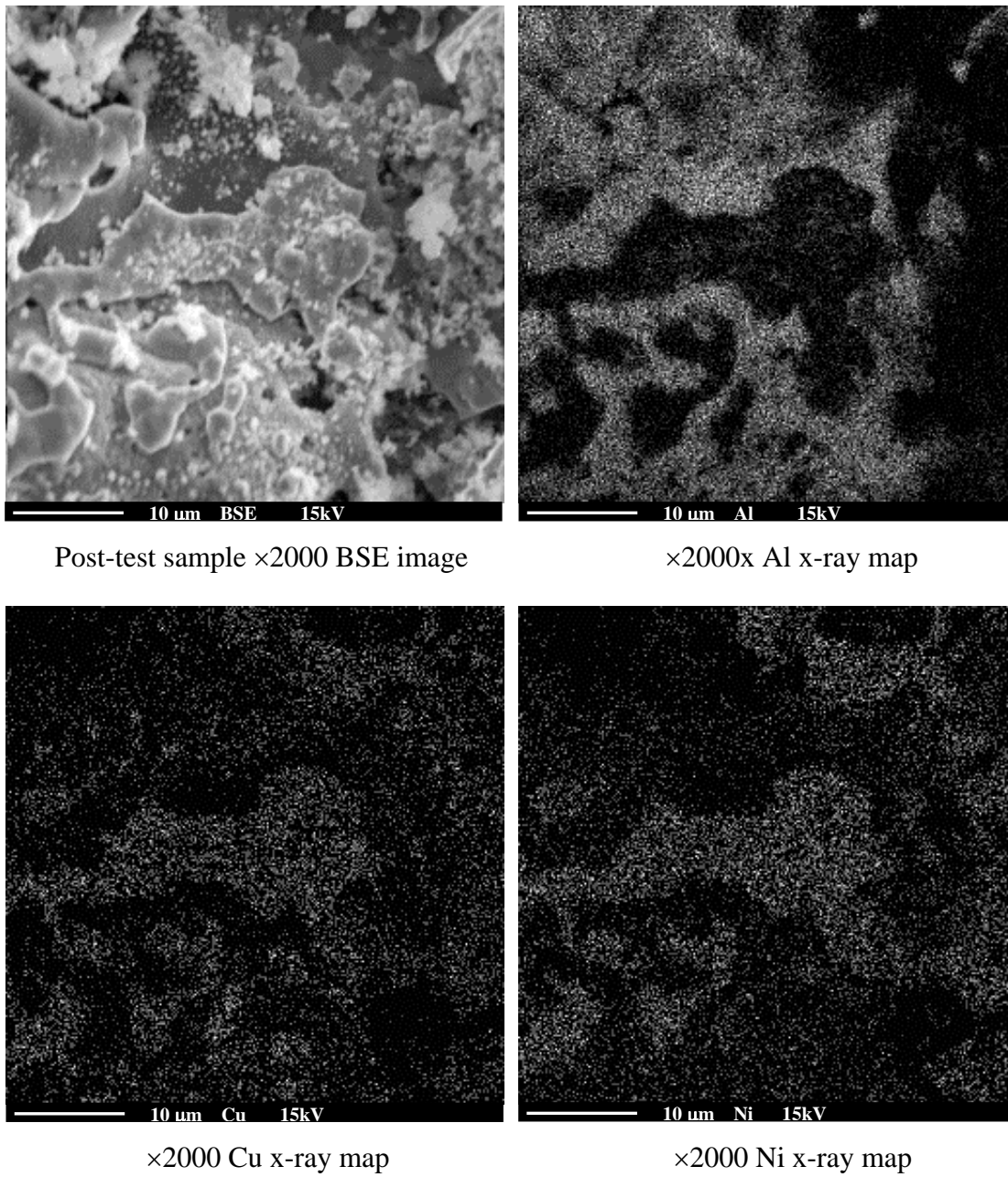
(b)

Figure 5.9. (Continued)

Co/Cu/β″-alumina MIEEs. — Metal Co is the first using in an AMTEC electrode in this research. The electrodes were tested having ratios of Co to Cu to β″-alumina of 3/3/2, the same ratio used with Ni/Cu/β″-alumina electrode discussed previously. Co/Cu/β″ electrode was tested over 70 days at 867°C electrode temperature of and 300°C pool temperature.

The impedance spectra are shown in Figure 5.10(a). By deconvoluting the spectra, the series resistance R_s, charge transfer resistance R_{ct} and diffusion resistance R_d were obtained and were all plotted verse experiment time in Figure 5.10(b), as well as R_{act}. It is found that R_s and R_d are basically stable for the entire experiment period, while the other two resistances increased gradually with experiment time for the first 35 days and then stabilized. Comparing this electrode's initial performance to that of Cu/β″ and Ni/Cu/β″ electrodes, we found that Co/Cu/β″ electrode has similar R_d to Cu/β″ or Ni/Cu/β″ electrodes, while its R_{ct} is much smaller than that of the Cu/β″ electrode, and slightly lower than the Ni/Cu/β″ electrode. This indicates that the role of Co might be similar to Ni in those mixed electrodes, which is more related to charge transfer process. Unfortunately, we did not test Co/β″-alumina electrode to prove this conjecture.

Additionally, the values of *B* are also close to those of Ni/Cu/β″ electrodes, but this electrode had a longer lifetime. The *B* values decreased for the first 30 days and then stabilized, shown in Figure 5.10(c). To summarize, Co/Cu/β″-alumina electrode's performance is similar to Ni/Cu/β″-alumina electrodes, but it degrades slowly.

The microstructure of this electrode before and after testing was shown in Figures 5.11(a) and (b). The SEM images for the pre-test sample are very similar to Ni/Cu/β″electrode. Metal particles are small and spherical, while β″-alumina particles have the varying size and shape. The microstructure of the electrode after testing shows β″-alumina particles grew and congregated to form a frame with Cu and Co particles inserted in it, while Cu and Co particles remained the small size, which indicated that β″-alumina limited the growth of metal particles. The small size of the metal particles most likely contributed to the slow degradation of this electrode.

Figure 5.10. a) The impedance spectra of Co/Cu/β″-alumina sample with Co/Cu/β″ ratios of 3/3/2. b) The changes of extracted R_{act}, R_s, R_{ct}, R_d versus experiment time. c) B value versus experiment time.

Figure 5.10. (Continued)

Pre-test sample ×2000 BSE image   ×2000 Al x-ray map

×2000 Cu x-ray map   ×2000 Co x-ray map
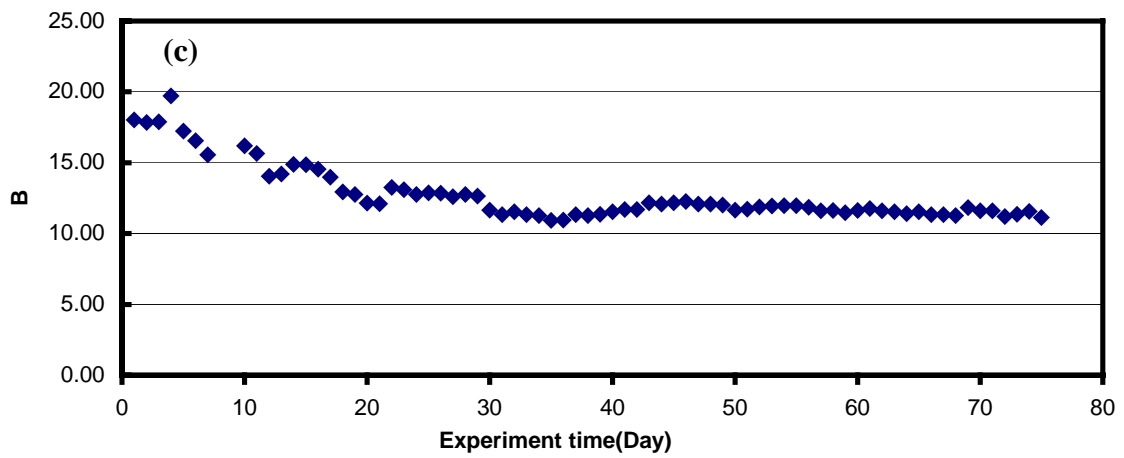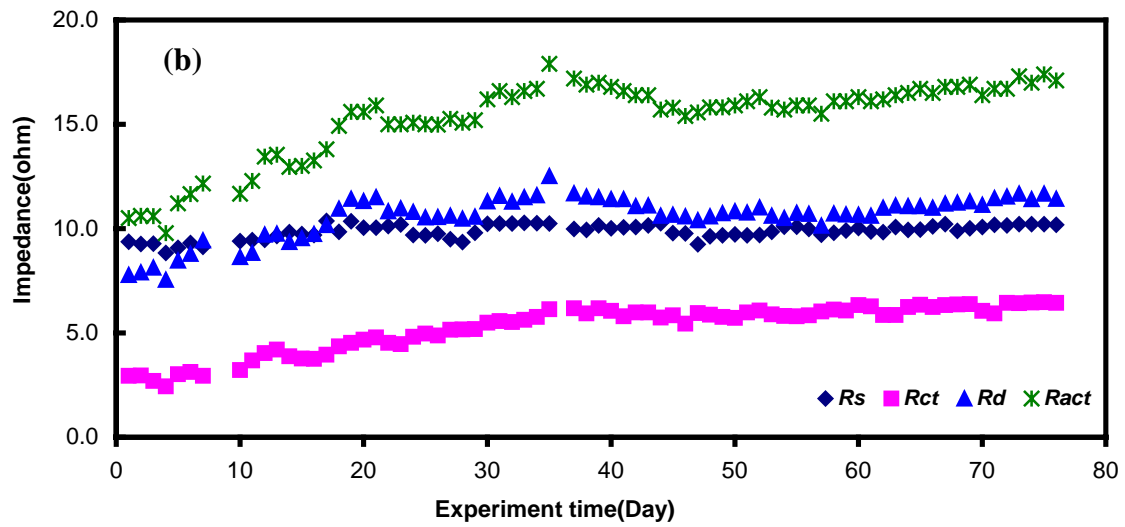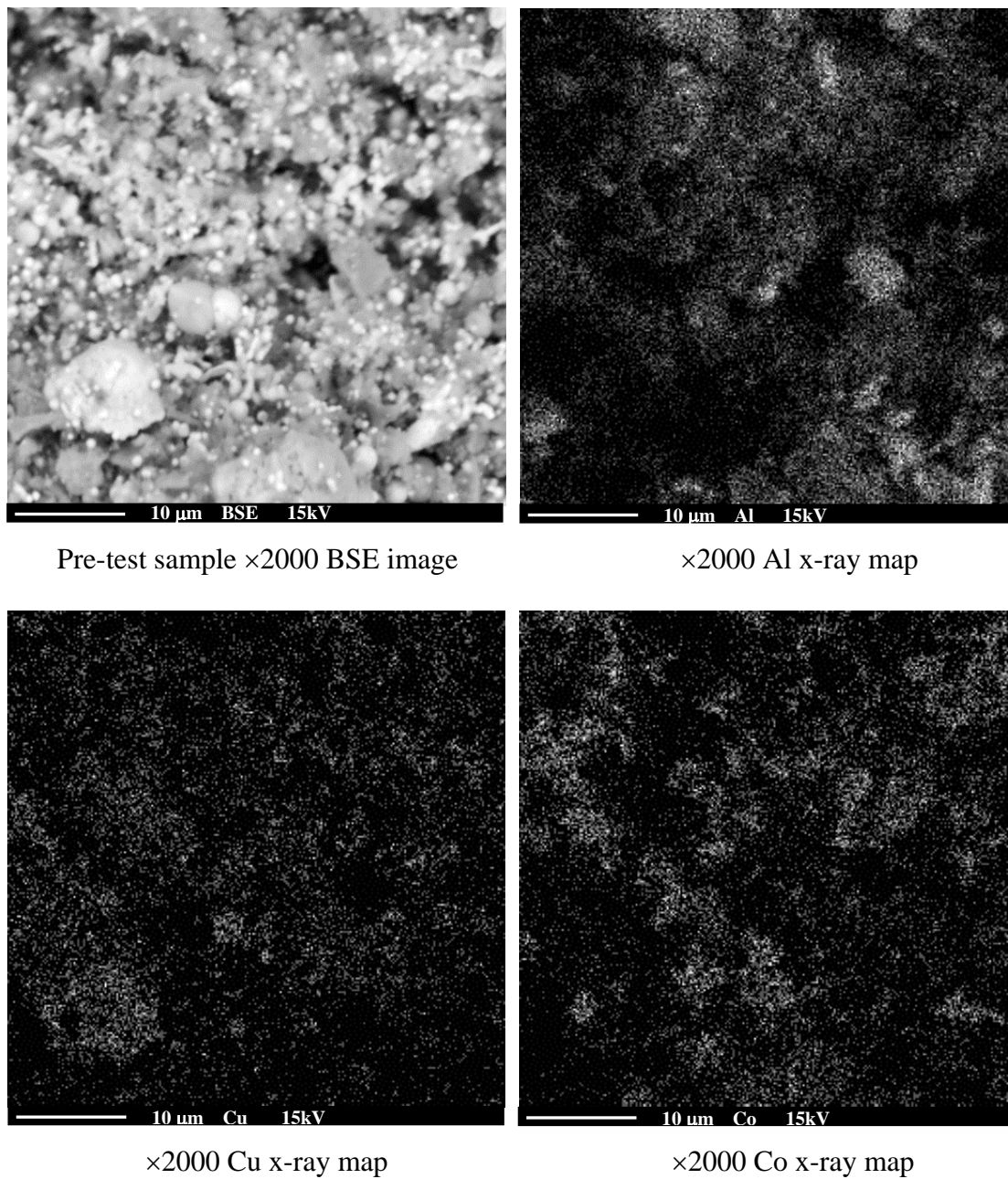
(a)

Figure 5.11. SEM images for Co/Cu/β″-alumina sample with Co/Cu/β″ ratios of 3/3/2 a) before and b) after testing in the SETC.
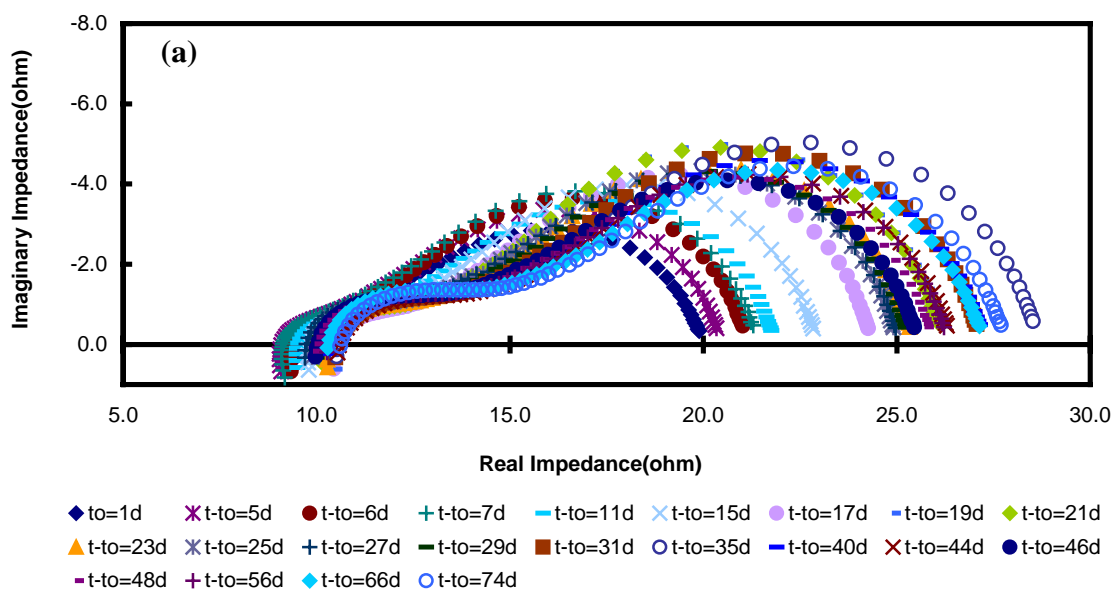
Post-test sample ×2000 SE image

×2000 Al x-ray map

×2000 Cu x-ray map

×2000 Co x-ray map
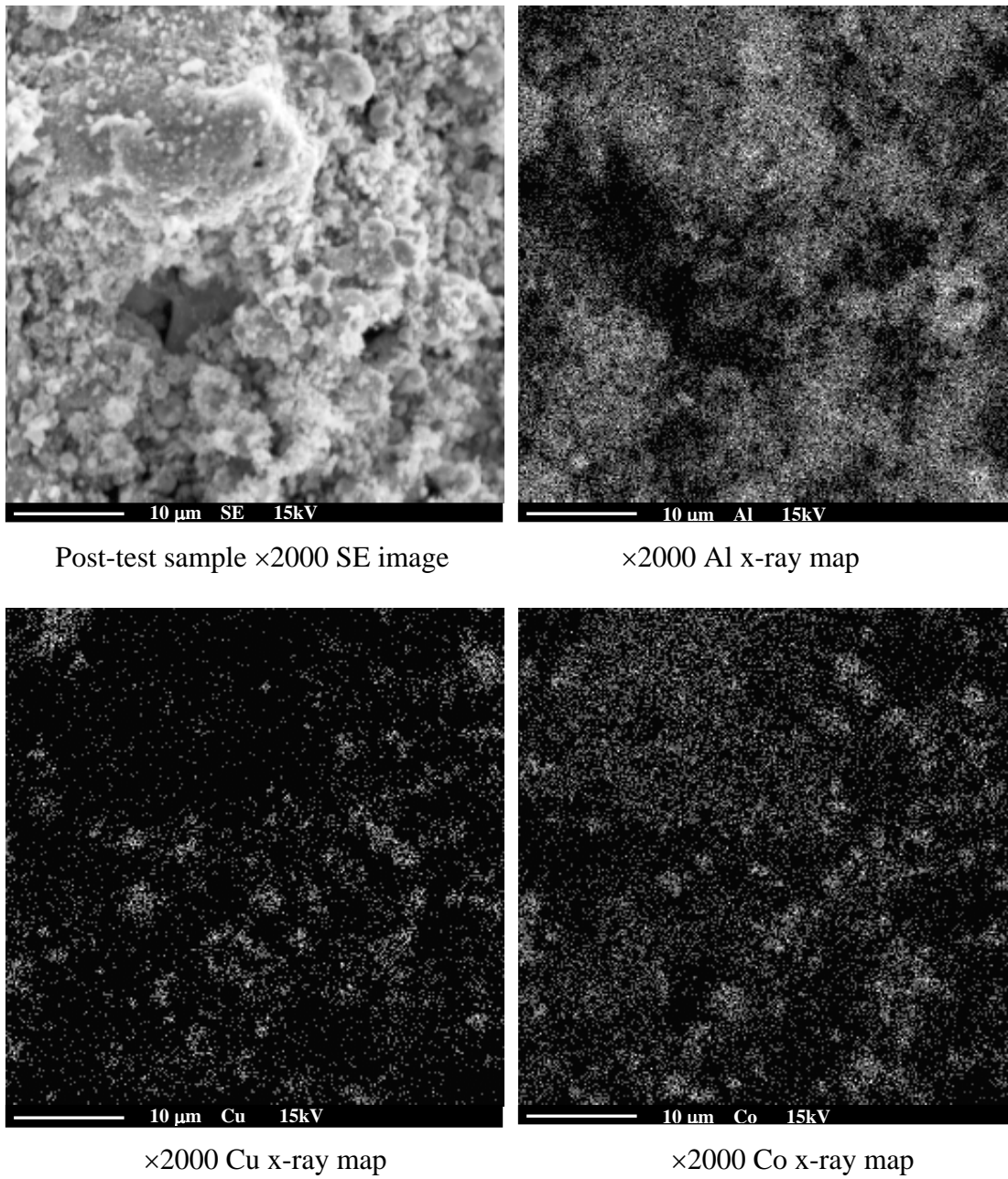
(b)

Figure 5.11. (Continued)

5.3.3 Metal/Sodium Titanate MIEEs

Cu/Sodium Titanate MIEEs. — This electrode was investigated with a Cu to sodium titanate (ST) ratio of 1/1 and its spectra are shown in Figure 5.12(a). It was found that the spectra did not intercept the real impedance axis at the right side. This failure to intercept is resulted from the low frequency limitation used in this measurement, 0.1Hz, not being low enough. Simulating experimental spectrum from 10^{-3} to 10^6Hz using the proposed equivalent circuit in Chapter IV generated a spectrum that adequately matched the experimental data and intercepted the real impedance axis, shown in Figure 5.12(b). R_{act} for this electrode was calculated from the extended low frequency intercept.

The deconvoluted spectra exhibit the charge transfer resistance is smaller than the transport resistance, the latter being more than twice of the former. Compared to the Cu/β″-alumina electrode, Cu/ST electrode has a larger R_d but their R_{ct} values are very close. According to the MIEE kinetic equation (4.26) described in Chapter IV, a large R_d should correspond to a small k_2. Based on equation (4.29), k_2 can be evaluated from the frequency at the maximum of the sodium transport semicircle. The experimental results show the ratio of these specific frequencies is 1/4 for those two electrodes, thus the sodium transport rate constant k_2 for the Cu/ST electrode is only 1/4 of that for the Cu/β″-alumina electrode.
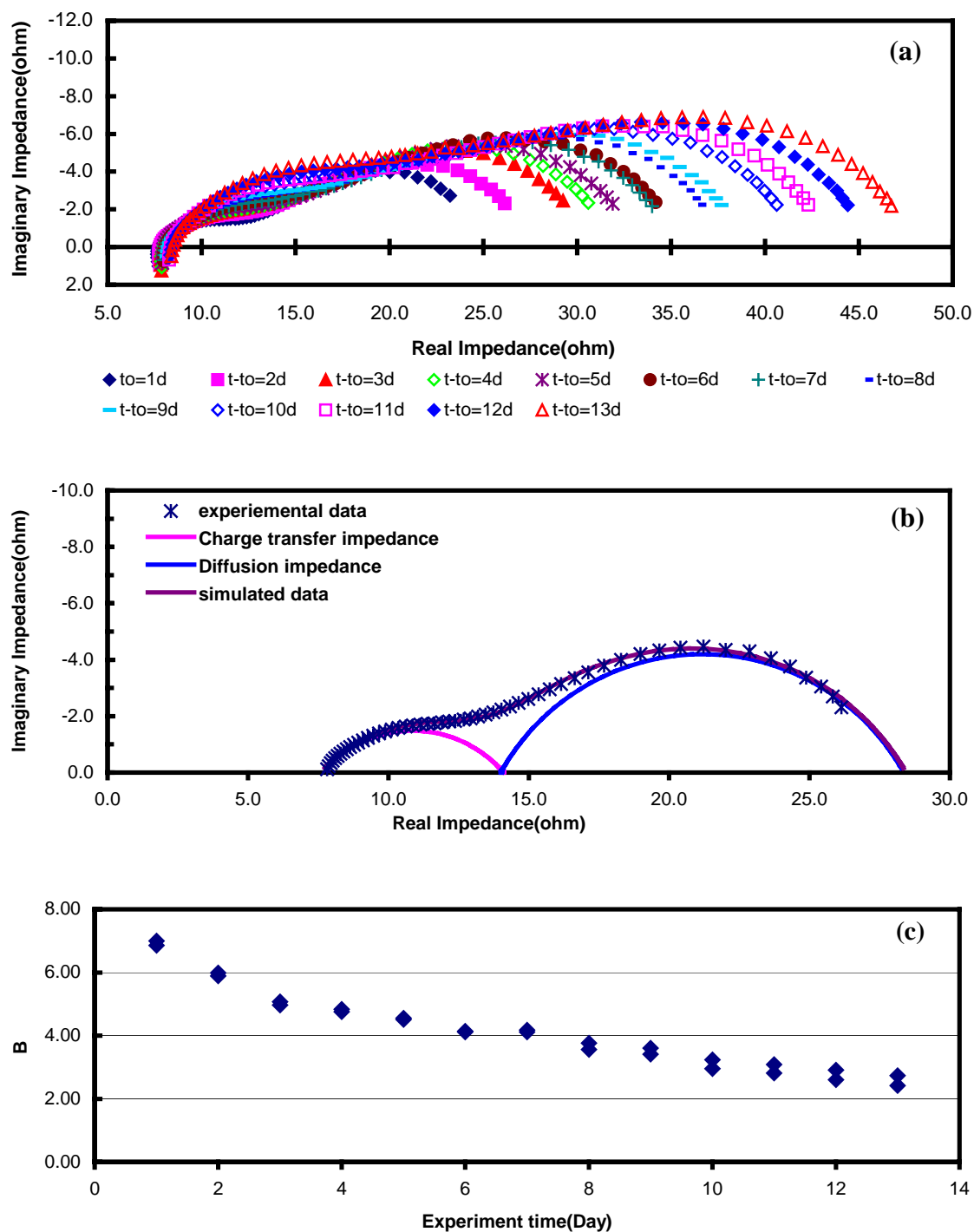
Figure 5.12. a) The impedance spectra of Cu/sodium titanate sample with Cu/ST ratio of 1/1. b) The impedance spectrum measured on t-to=6d, and its deconvoluted spectra for charge transfer and sodium transport processes. c) *B* value versus experiment time.

The large R_d can be explained from the electrode's morphological characteristics, shown in Figure 5.13. The pre-test SEM images show the electrode film is dense. Sodium titanate is present as very large particles, which are connected together to form a frame and the Cu particles are embedded in the frame or on the top of it. Thus the porosity in this electrode is very low. Such a microstructure could result in a small reaction area and difficult sodium transport within the electrode, but the adhesion of this electrode to the BASE is good.

The SEM images for the post-test sample show that some area of the BASE is bald, without the coverage of the electrode film. This loss occurred because the electrode film stuck to the current collector and was separated from BASE during SETC disassembly or during the process of making SEM samples. Figure 5.13(b) show that the Cu particles aggregated together around the sodium titanate, shown in

The B value sharply decreased with experiment time as shown in Figure 5.12(c). Compared to the Cu/β″-alumina electrode, the Cu/ST electrode did not show any improvement. The large particle size of sodium titanate could be the main reason for this result.

Pre-test sample ×500 SE image   ×2000 BSE image

×2000 Cu x-ray map   ×2000 Ti x-ray map
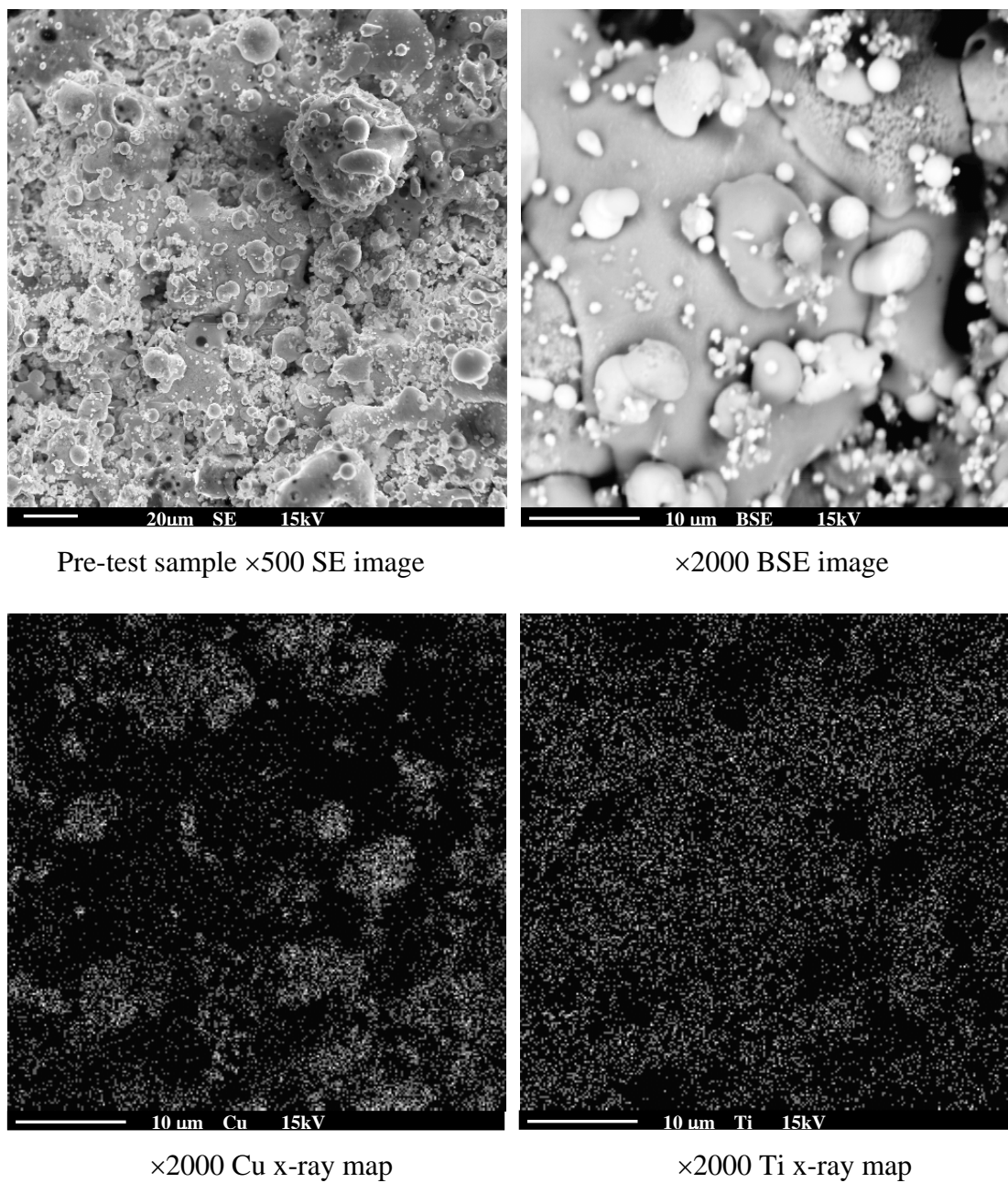
(a)

Figure 5.13. SEM images for Cu/sodium titanate sample a) before and b) after testing in the SETC.

Post-test sample ×500 BSE image

×2000 BSE image

×2000 Cu x-ray map

×2000 Ti x-ray map
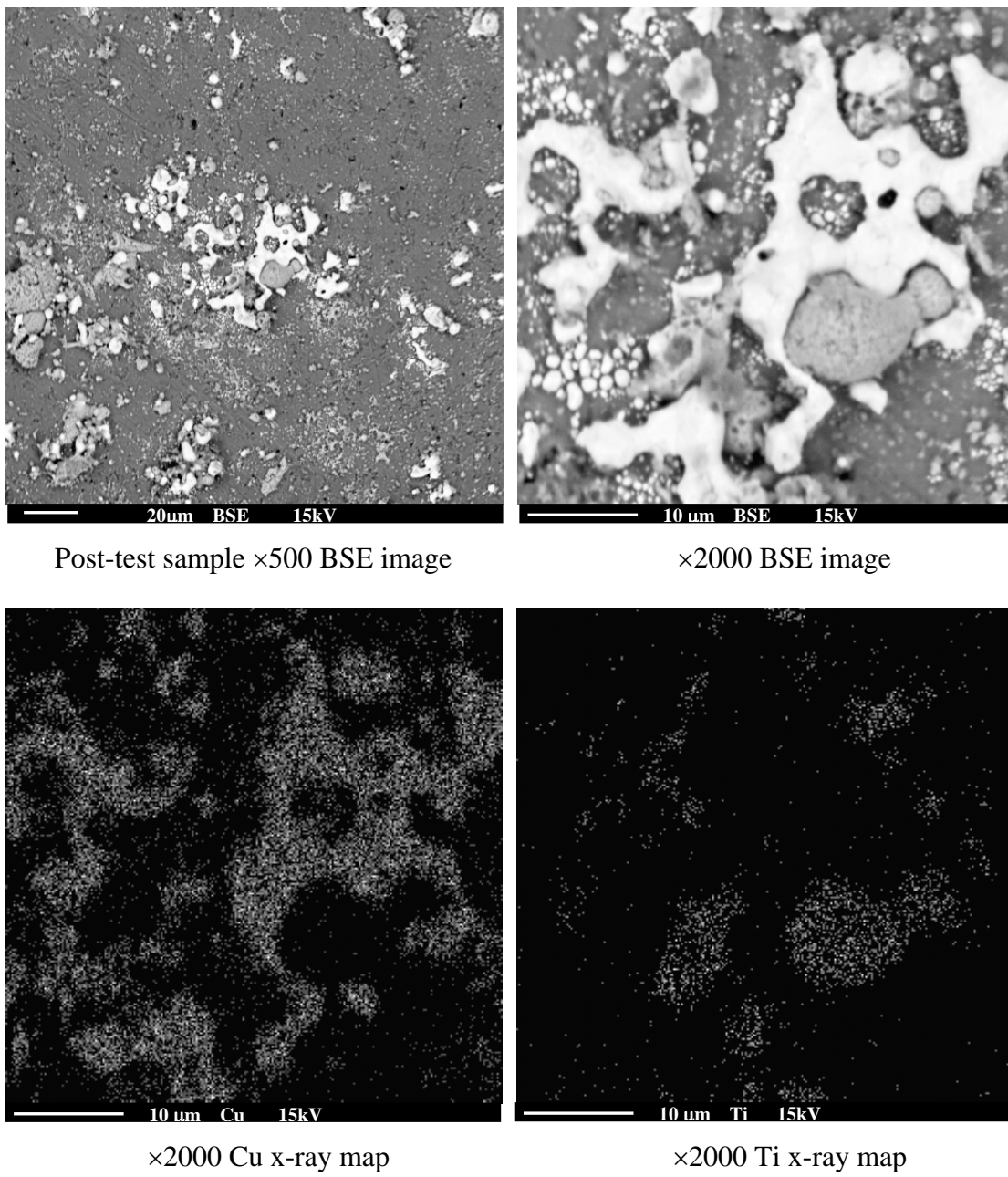
(b)

Figure 5.13. (Continued)

Figure 5.14 is the spectra of the electrode with a 4/1 ratio measured at 845°C electrode temperature and 309°C pool temperature. It is found that the value of R_{ct} is about 0.1Ω, and R_d increases with experiment time from 1.5Ω to 2.5Ω. Such small R_{ct} and R_d had never been obtained in our tested electrodes previously. Its B values were as high as 70 at initial, then decreased and finally stabilized around 50, which is much higher than that of TiN electrode after 10-40 days testing at this temperature.

Carefully observing its spectra, it is found that the spectra are different from traditional spectra of mixed electrodes in shape. The semicircle curves are hardly depressed. We discussed the relationship of the depressed extent of the semicircle with the surface roughness in Chapter IV, and concluded that a real semicircle without any depression indicates the interface is smooth. Therefore, this electrode has a smooth interface between electrode and electrolyte.

Figure 5.15 shows the electrode's microstructure after testing. It is found that Ni formed a complete network within the whole electrode, as did sodium titanate and they were interwoven, which matches the designed ideal morphology for a high performance electrode described in Chapter III.
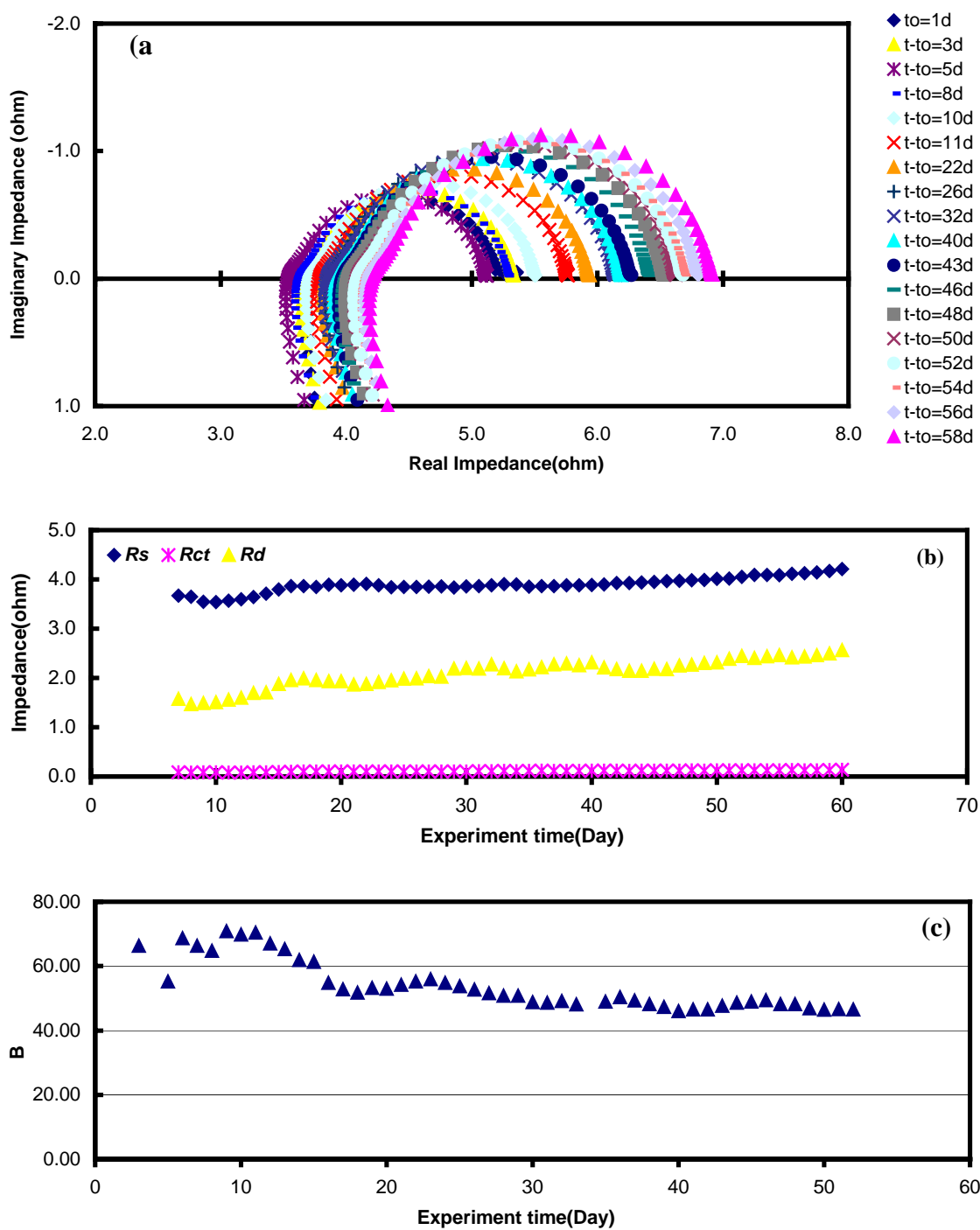
Figure 5.14. a) The impedance spectra of Ni/sodium titanate electrode with Ni/ST ratios of 4/1 b) The changes of extracted R_s, R_{ct}, and R_d, versus experiment time and c) B value versus experiment time.
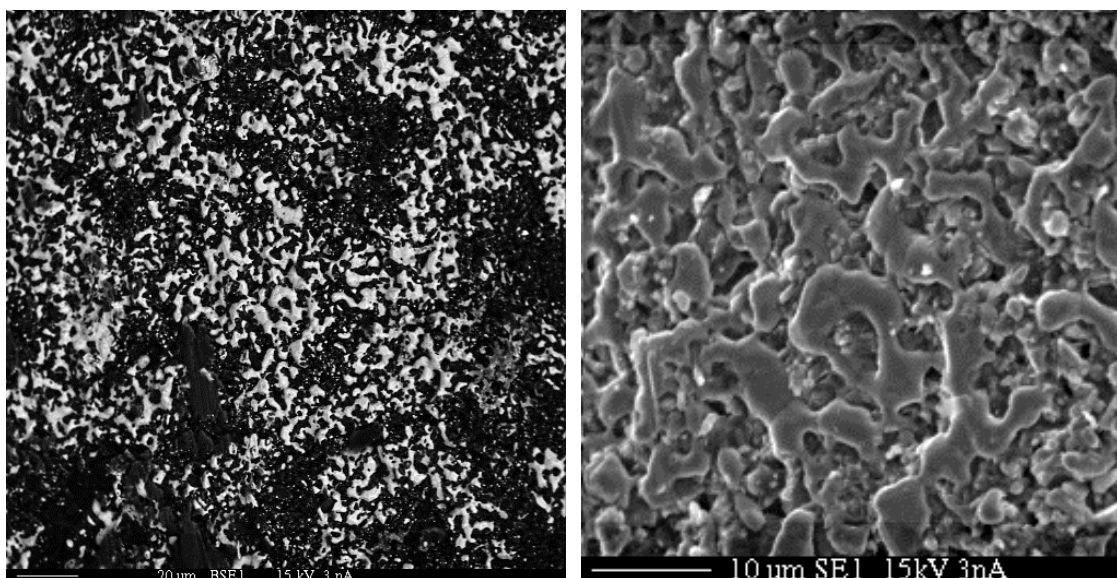
Post-test sample ×500 BSE image   ×2000 SE image
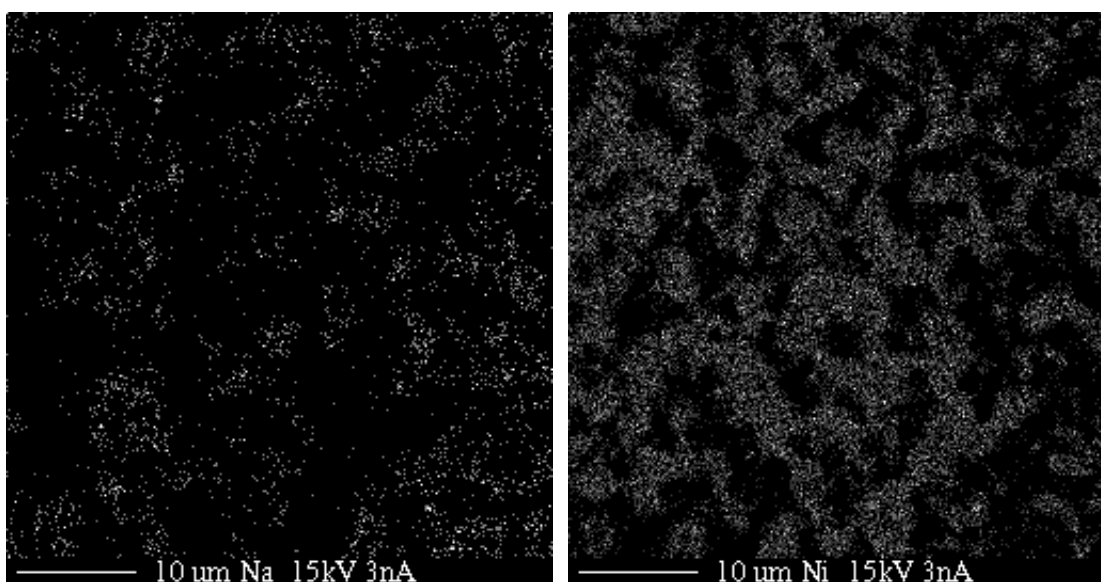
×2000 Na x-ray map   ×2000 Ni x-ray map

Figure 5.15. SEM images of the Ni/sodium titanate sample with Ni/ST ratios of 4/1 after testing in the SETC.

Ni/Cu/sodium titanate MIEEs. — The tested electrodes had Ni/Cu/Sodium titanate ratios of 3/3/2 and 3/3/3. Cu was added to improve the adhesion of the electrode film to the BASE. In all tested electrodes, the mass of Cu is same as that of Ni. The impedance spectra of Ni/Cu/ST electrode with mass ratios of 3/3/2 were measured at 844^oC electrode temperature and 290^oC pool temperature, shown in Figure 5.16.

The R_{act} value first decreased with time, then stabilized for 30 days and finally slowly increased with experiment time. Since these two types of electrodes have the same metal components and β″-alumina even has a higher Na^+ ion conductivity than sodium titanate, it seems that the better performance should belong to Cu/Ni/β″ electrode, but the experiment data show that Ni/Cu/ST electrode has the smaller R_s, R_{ct} and R_d. The electrode performance is not only dependent on the physical properties of the electrode components, but also on the microstructure formed by these components connection. Thus, the better performance of Ni/Cu/ST electrode suggests that metal Ni and Cu combining with sodium titanate should display the sort of microstructure favorable to charge transfer and sodium transport that was discussed in the theoretical analysis of mixed electrode composition and kinetics in Chapter III.

The SEM images of this electrode are shown in Figure 5.17(a) and (b). The images of the pre-test sample show that Ni, Cu and sodium titanate are all deposited on the BASE with the desired ratio and all three particles are present as small spheres. Compared to the particles in the Cu/sodium titanate electrode, the particle size of the sodium titanate significantly decreased, although some big grains still are present. The raw sodium titanate used in this electrode was ball-milled in the alcohol medium.
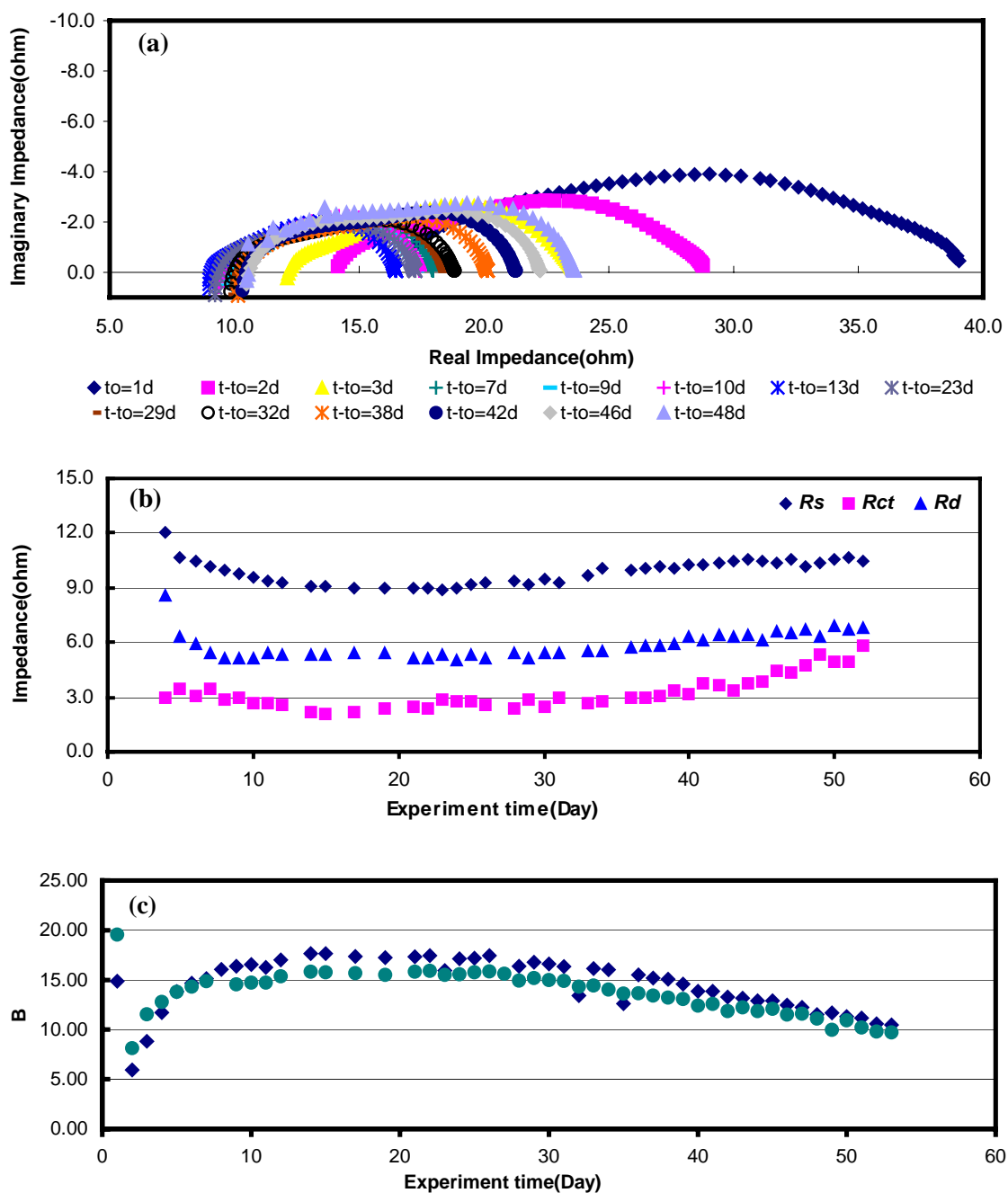
Figure 5.16. a) The impedance spectra of Ni/Cu/sodium titanate electrode with Ni/Cu/ST ratios of 3/3/2. b) The changes of extracted R_s, R_{ct}, and R_d versus experiment time. c) B value versus experiment time.

Ni and sodium titanate particles grew during the test, shown in Figure 5.17(b). The amount of Cu in the post-test sample is much less than the pre-test sample, which could be caused by Cu evaporation during the test. Cupper has a fairly high vapor pressure at elevated temperature, three orders of magnitude larger than that of nickel. Insufficient amount of the Cu in the electrode could result in R_{ct} increase, but Ni was still present in the electrode and played the role of electronic conductor. Additionally, previous discussion indicated that the metal Ni is more related to the charge transfer process than Cu. Therefore, this could be the reason of the R_{ct} slowly increased near the end of test.

Another tested Ni/Cu/sodium titanate electrode has Ni/Cu//Sodium titanate ratios of 3/3/3. To reduce the sodium transport resistance, the amount of sodium titanate was increased, compared to Ni/Cu/ST electrode with 3/3/2 ratios previously discussed. But experiment data show that the addition of sodium titanate did not improve the electrode performance. The spectra of Ni/Cu/ST electrode with 3/3/3 ratios and extracted R_s, R_{ct} and R_d changes with time are shown in Figure 5.18(a) and (b). It is found that R_s, R_{ct}, R_d and B are all very similar to those of Ni/Cu/ST with 3/3/2ratios, but after 30 days, these resistances increased or B decreased with time more rapidly than the 3/3/2 electrode.

The SEM images of the pre-test sample are shown in Figure 5.19 (a). Compared to the 3/3/2 electrode, it is found that the amount of sodium titanate seems not to be increased, i.e., the extra amount of sodium titanate did not appear to deposit on the BASE. The amount of Cu seems to be less than 3/3/2 electrode. The microstructure of the post-test sample is similar with that of 3/3/2 electrode, shown in Figure 5.19 (b). Cu evaporation and Ni particles coalescence also occurred in this electrode during the test.

Pre-test sample ×2000 BSE image　　　　×2000 Ti x-ray map

×2000 Cu x-ray map　　　　×2000 Ni x-ray map

(a)

Figure 5.17. SEM images for Ni/Cu/sodium titanate sample with Ni/Cu/ST ratios of 3/3/2 a) before and b) after testing in the SETC.
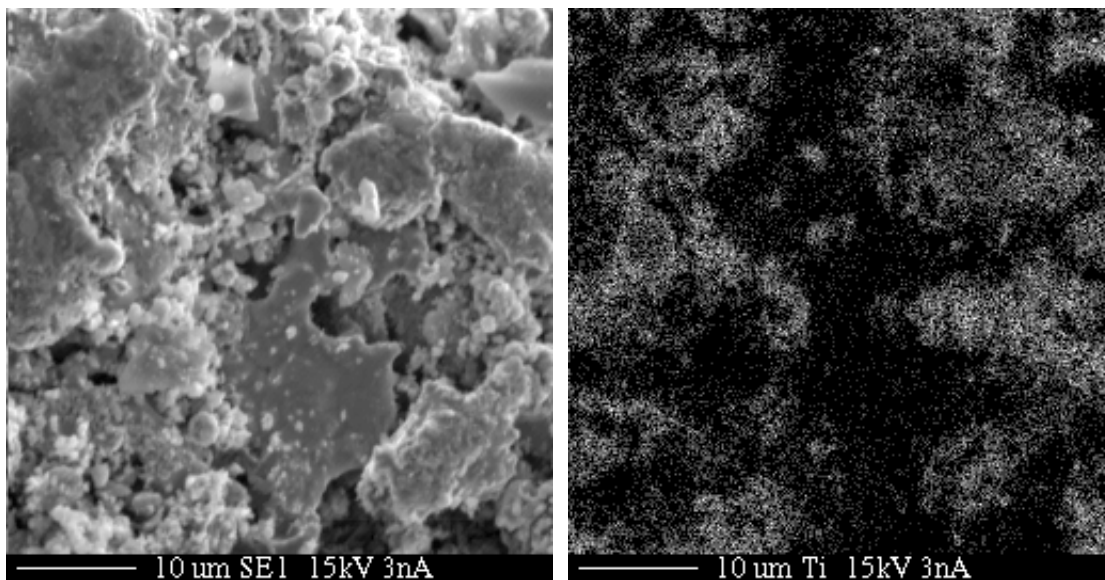
Post-test sample×2000 SE image

×2000 Ti x-ray map
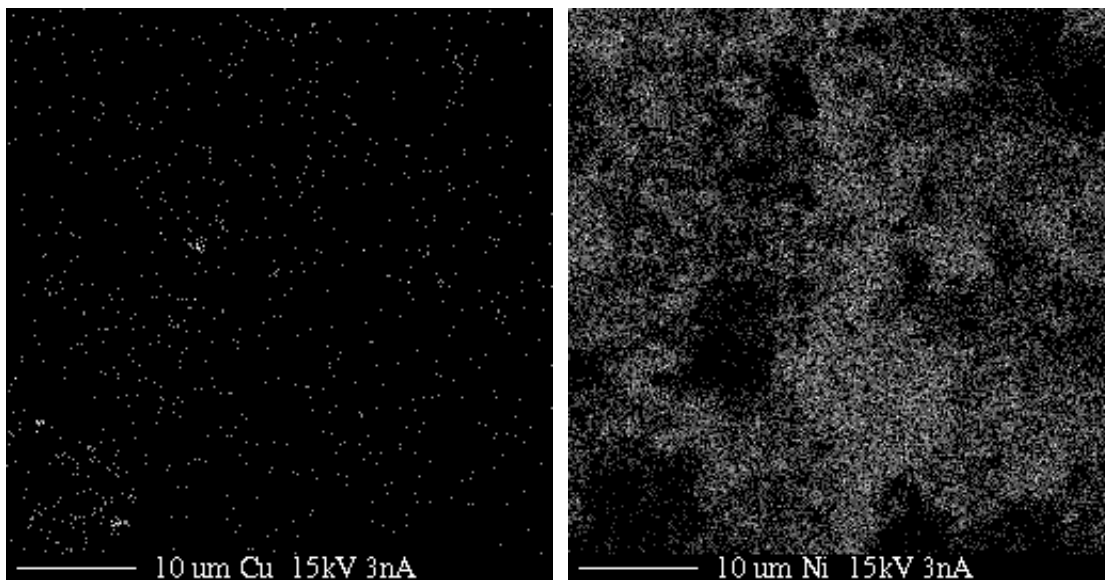
×2000 Copper x-ray map
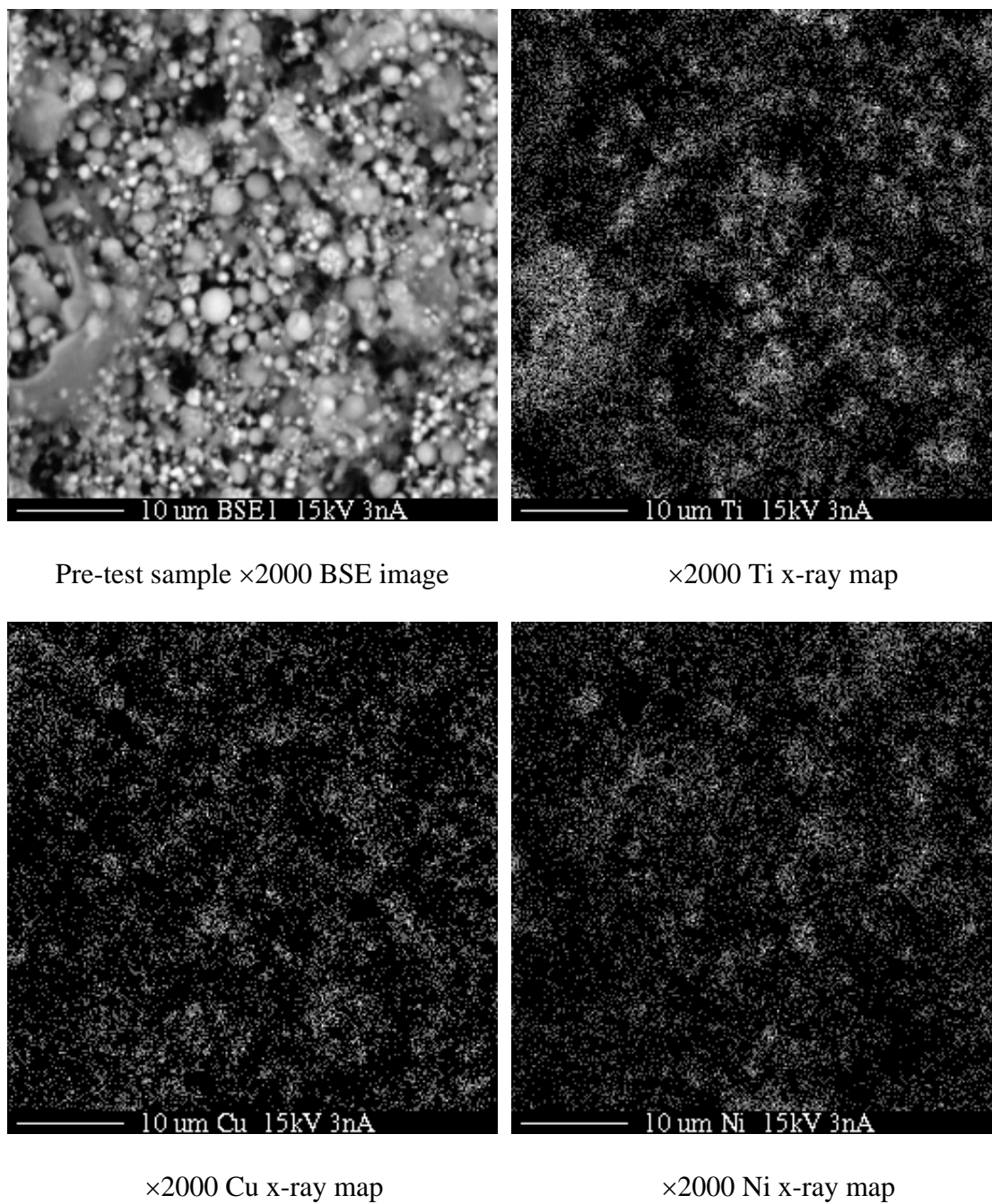
×2000 Nickel x-ray map

(b)

Figure 5.17. (Continued)
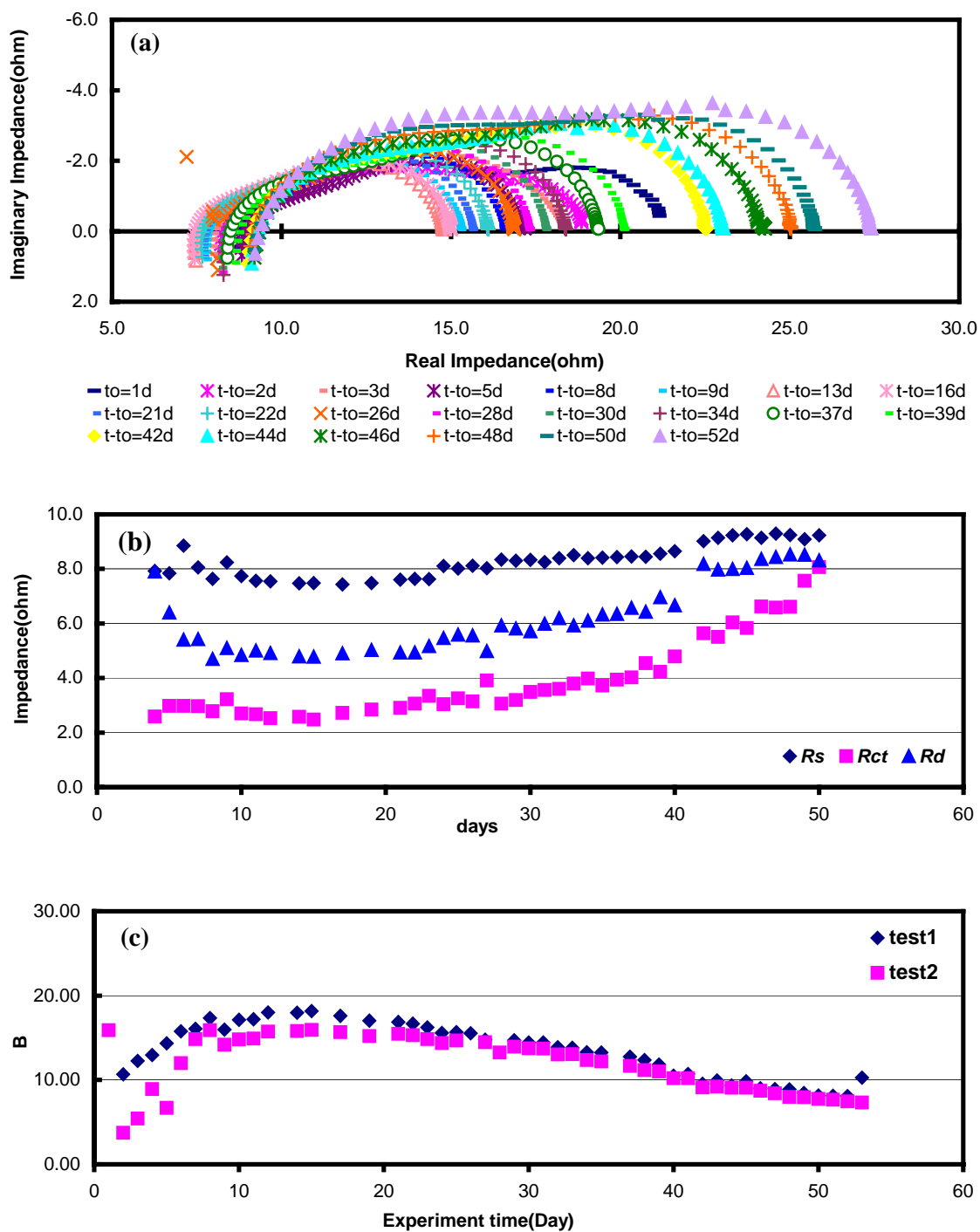
Figure 5.18. a) The impedance spectra of Ni/Cu/sodium titanate electrode with Ni/Cu/ST ratios of 3/3/3. b) The changes of extracted R_s, R_{ct} and R_d versus experiment time. c) B value versus experiment time.

Pre-test sample ×2000 BSE image   ×2000 Ti x-ray map

×2000 Cu x-ray map   ×2000 Ni x-ray map
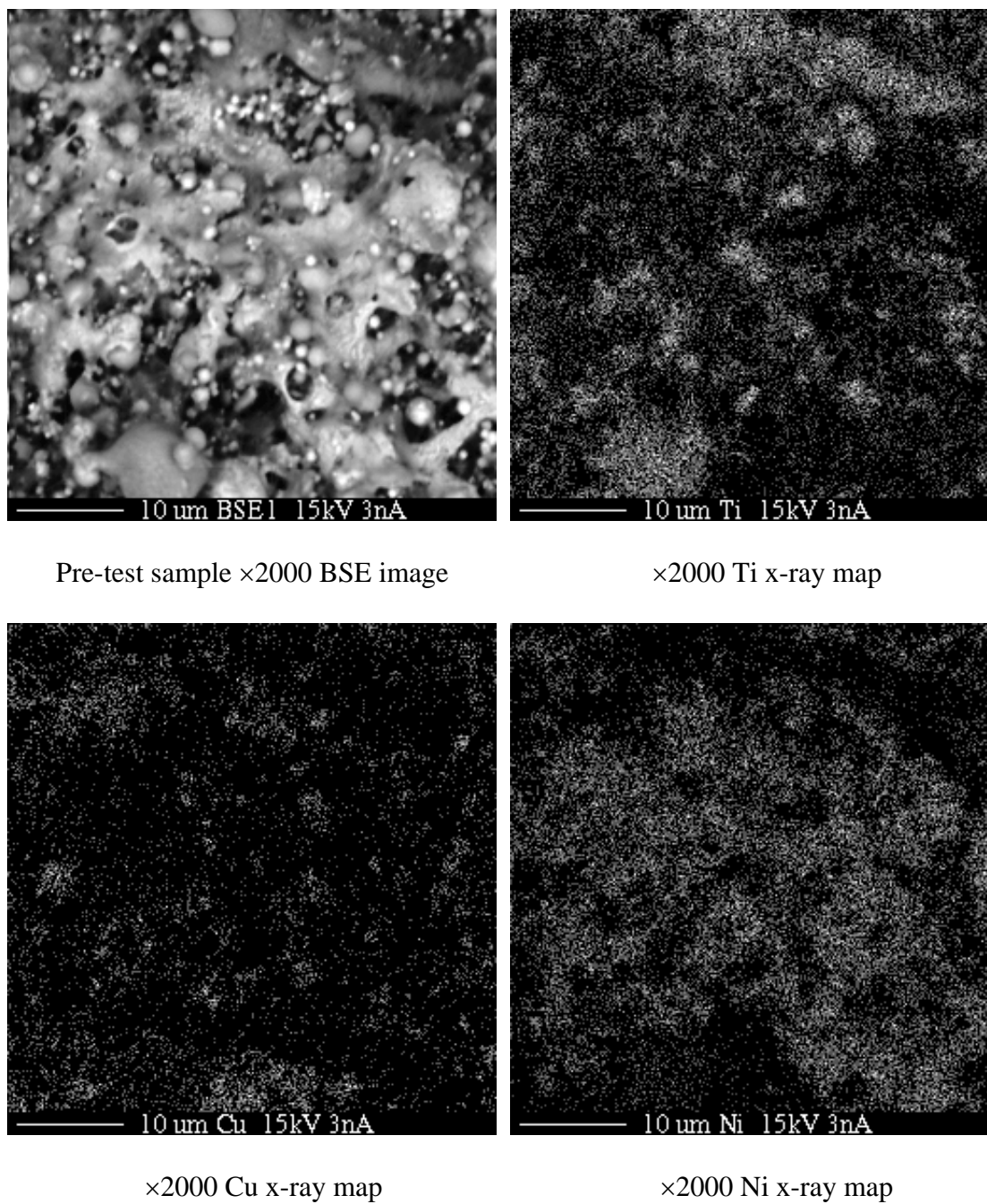
(a)

Figure 5.19. SEM images for Ni/Cu/sodium titanate sample with Ni/Cu/ST ratios of 3/3/3 a) before and b) after testing in the SETC.
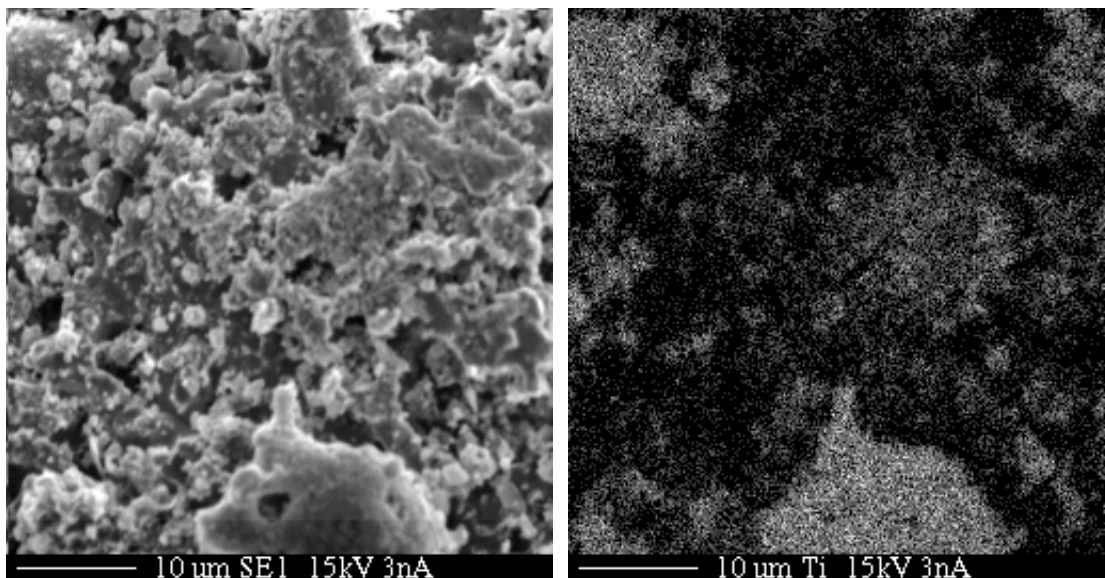
Post-test sample ×2000 SE image
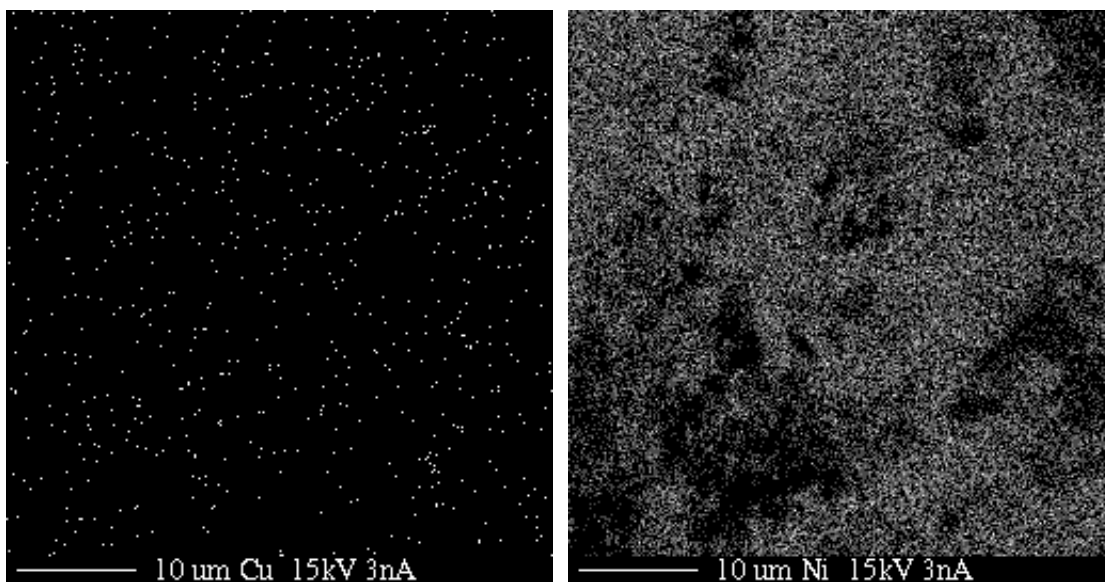
×2000 Ti x-ray map

×2000 Cu x-ray map

×2000 Ni x-ray map

(b)

Figure 5.19. (Continued)

Co/Cu/sodium titanate. — The electrodes tested in this research have two different compositions, with the mass ratios of Co/Cu/ST of 3/2/1 and 3/4/1. The impedance spectra of the electrode with 3/2/1 ratios are shown in Figure 5.20(a) and (b). For this electrode, its R_{ct} is larger than R_d, which is possibly caused by the insufficient amount of electronic conductor, metals. Therefore, we increased the mass of metals in the electrode, which generated the electrode with 3/4/1ratios.

The electrode with 3/4/1ratios displayed the good performance initially, but then degraded rapidly, shown by its spectra in Figure 5.21(a). It did not make any progress towards reducing R_{ct}, i.e., increasing conductivity, compared to the electrode with 3/2/1 ratios. Figure 5.21(b) shows R_s, R_{ct} and R_d change with time. R_{ct} and R_d increase rapidly and linearly with time after running 30 days. Such raid increase in R_{ct} and R_d would result this electrode complete failure.
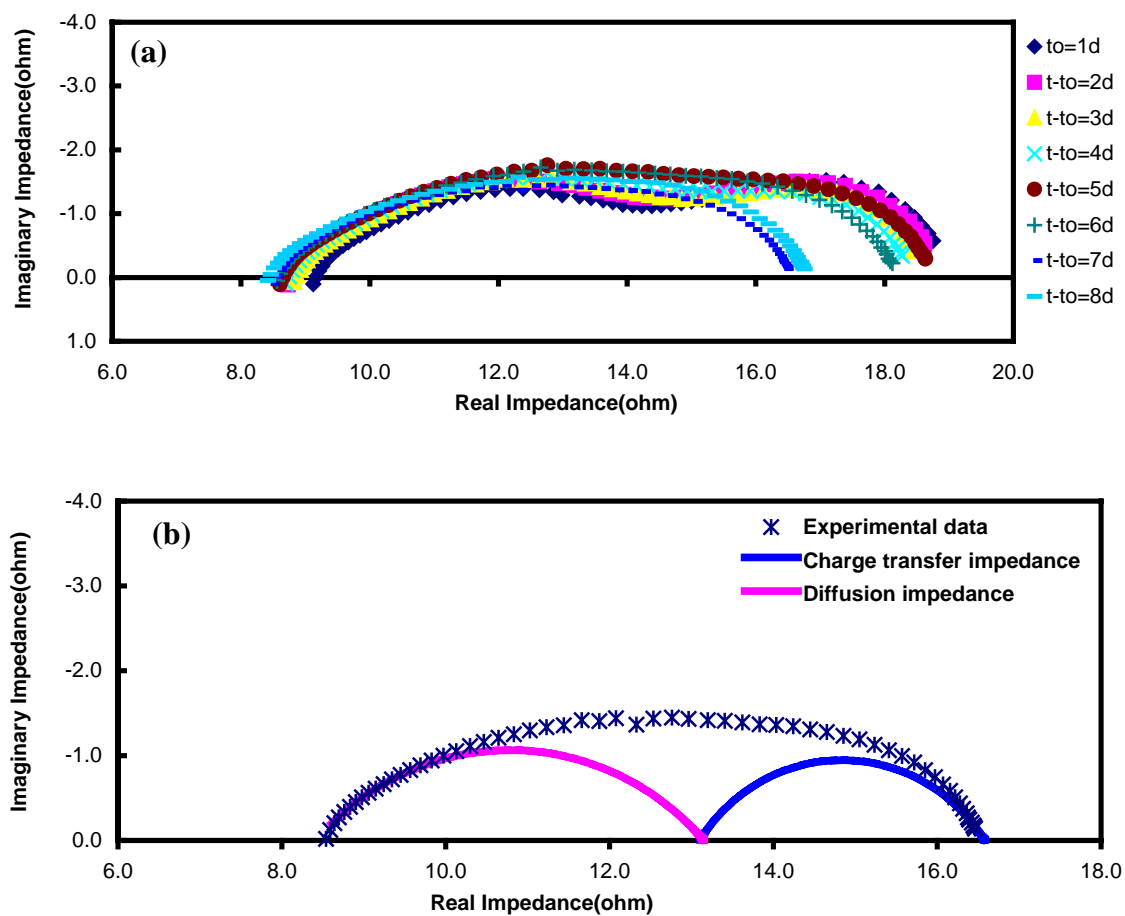
Figure 5.20. a) The impedance spectra of Co/Cu/sodium titanate electrode with Co/Cu/ST ratios of 3/2/1. b) The impedance spectrum measured on t-to=7d, and its deconvoluted spectra for charge transfer and sodium transport processes.
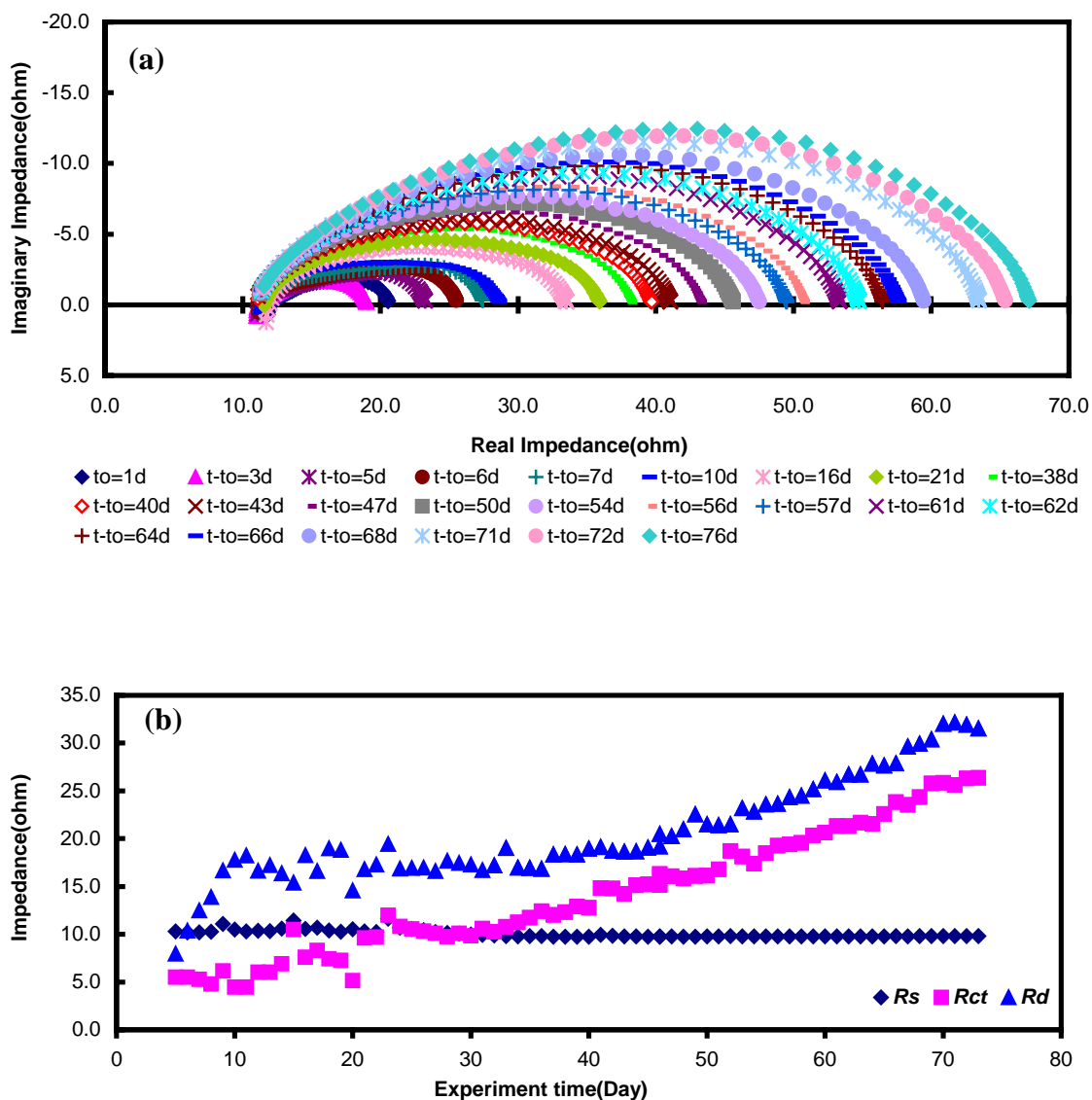
Figure 5.21 .a) The impedance spectra of Co/Cu/sodium titanate electrode with Co/Cu/ST ratios of 3/4/1. b) The changes of extracted R_s, R_{ct} and R_d with experiment time.

5.3.4 The Effect of Charge Transfer Coefficient α on B

B, the normalized exchange current density, is the only temperature independent index available for evaluating AMTEC electrode performance, therefore, it is important and necessary to clarify the validity of B. The transfer coefficient α, is a measure of the symmetry of the energy barrier for a charge transfer reaction. In most electrochemical systems, α turns out to lie between 0.3 and 0.7. For AMTEC, JPL assumed α is 1/2, while this research measured α to be approximately 1/3. α is one of the factors that affect B. If α is changed, B's equation needs to be corrected.

B is defined in equation (5.1)

$$B = \frac{J_o^o T_{el}^{1/2}}{P_{el}} \tag{5.1}$$

Researchers in JPL defined J_o^o as the exchange current at the equilibrium potential obtained with saturated sodium vapor in contact with the electrode and it is defined in equation (5.2),

$$J_o^o = J_o \left(\frac{P_{el}}{P_{Na}} \right)^{\alpha} \tag{5.2}$$

J_o is the exchange current at actual equilibrium potential of the cell, defined in equation (5.3)

$$J_o = \frac{RT_{el}}{FR_{act}} \tag{5.3}$$

Substituting equation (5.2) and (5.3) into Eq.(5.1), the following equation is obtained,

$$B = \frac{J_o^o T_{el}^{1/2}}{P_{el}} = J_o \left(\frac{P_{el}}{P_{Na}}\right)^{\alpha} \frac{T_{el}^{1/2}}{P_{el}} = \left[\frac{T_{el}^{1/2}}{P_{el}^{1-\alpha} P_{Na}^{\alpha}}\right] \frac{RT_{el}}{FR_{act}} \tag{5.4}$$

In a SETC, based on vapor kinetics theory, the sodium vapor pressure at the electrode is

$P_{el} = P_{Na} \sqrt{\dfrac{T_{el}}{T_{Na}}}$. Therefore, equation (5.4) becomes

$$B = \frac{T_{el}^{1/2}}{\left(P_{Na}\sqrt{\dfrac{T_{el}}{T_{Na}}}\right)^{1-\alpha} P_{Na}^{\alpha}} \frac{RT_{el}}{FR_{act}} = T_{el}^{\frac{2+\alpha}{2}} T_{Na}^{\frac{1-\alpha}{2}} \frac{R}{P_{Na} FR_{act}} \tag{5.5}$$

This equation shows that B is a function of α. Therefore, B will change with α.

If $\alpha = \alpha_1$,
$$B_1 = T_{el}^{\frac{2+\alpha_1}{2}} T_{Na}^{\frac{1-\alpha_1}{2}} \frac{R}{P_{Na} FR_{act}} \tag{5.6}$$

If $\alpha = \alpha_2$,
$$B_2 = T_{el}^{\frac{2+\alpha_2}{2}} T_{Na}^{\frac{1-\alpha_2}{2}} \frac{R}{P_{Na} FR_{act}} \tag{5.7}$$

Divided (5.6) by (5.7), produces

$$\frac{B_1}{B_2} = \left(T_{el}^{\frac{2+\alpha_1}{2}} T_{Na}^{\frac{1-\alpha_1}{2}} \frac{R}{P_{Na} FR_{act}}\right) \Big/ \left(T_{el}^{\frac{2+\alpha_2}{2}} T_{Na}^{\frac{1-\alpha_2}{2}} \frac{R}{P_{Na} FR_{act}}\right) = \left(\frac{T_{el}}{T_{Na}}\right)^{\frac{\alpha_1-\alpha_2}{2}} \tag{5.8}$$

This equation shows B monotonously increases with increasing α. Therefore, the greater α, the greater B. In our SETCs, the pool temperature (T_{Na}) is 285~305°C, and electrode temperature (T_{el}) is 840~865°C. If α ranges between 0.3 and 0.7, the ratio in equation (5.8) varies from 1 to 1.14, which means the values of B calculated at different transfer coefficients are slightly different.

Taking the derivative of B with respect to α, yields

$$\frac{dB}{d\alpha} = \frac{1}{2} B \ln\left(\frac{T_{el}}{T_{Na}}\right) \tag{5.9}$$

thus,

$$\frac{\Delta B}{B} = \frac{\Delta\alpha}{2}\ln\left(\frac{T_{el}}{T_{Na}}\right) = \ln\left(\frac{T_{el}}{T_{Na}}\right)^{\frac{\Delta\alpha}{2}} \tag{5.10}$$

In the temperature range described above, if α ranges from 0.3 to 0.7, the value of

$\frac{\Delta B}{B}$ is in the range from 0 to 0.14, which means that the maximum change in B is 14%

due to changing α. For the most common temperature, $T_{el} = 850^{\circ}C$ and $T_{Na} = 300^{\circ}C$, the

B value at $\alpha = 1/2$ is 1.06 times the B value at $\alpha = 1/3$.

B is a sensitive measure of the electrode performance. Large changes in B reflect

relatively small changes in electrochemical cell performance. Therefore, a 14% error in

B does not affect the evaluation of electrode performance. Additionally, other

measurement errors could affect the value of B, such as temperature and apparent charge

transfer resistance. Compared to the errors from these factors, it is believed that the

transfer coefficient α does not contribute significant errors to B. Therefore, equation

(5.11) is valid to calculate B.

$$B == \left[\frac{T_{el}}{P_{el}P_{Na}}\right]^{1/2}\left[\frac{RT_{el}}{FR_{act}}\right] \tag{5.11}$$

5.4 Summary and Conclusions

We have investigated two types of MIEEs, metal/β''-alumina electrodes and metal/sodium titanate electrodes. For each type of electrode, different metals and compositions are used to prepare a series of electrodes and their performance were measured. The metals used were W, Ni, Cu and Co.

For metal/β''-alumina electrodes, the performance was similar each other no matter which metal or composition used and lower than the performance of standard TiN electrode, or even a pure Ni electrode. The flame spraying deposition technique worked for the fabrication of mixed electrodes with multiple components. The experiment results indicated that Cu is capable of improving the electrode adhesion.

For metal/sodium titanate electrodes, Ni/sodium titanate preformed best. The Ni/sodium titanate electrode with 4/1 mass ratio displayed a very good performance with the initial B as large as over 60 and final B stable around 50, and a long lifetime, which satisfy the requirement of AMTEC electrodes. It was found that the particle size and the composition changed the performance of these electrodes significantly. Cu was added in the electrode as the second metal to improve electrode adhesion, but it evaporated during testing, which made the electrode performance degrade more rapidly. Additionally, the electrodes with Cu had a lower sodium transport resistance. The kinetics suggested that these Cu electrodes have a large rate constant for sodium transport. The electrodes with Ni generally provide a small charge transfer resistance, which implies that Ni particles are more related to the charge transfer reaction. The possible reason could be the Ni particles form a network microstructure that is close to the theoretical morphology of the

ideal electrode. The experimental results proved that the performance of MIEEs is strongly dependent on microstructure, as discussed in Chapter III. It is also found that grain agglomeration occurred in all electrodes, and the ceramic components limited the growth of metal grains, which results in a longer lifetime than the pure metal electrode.

Different values of the transfer coefficient α can cause variations in B values. For standard SETC conditions, it will cause 6% change, while for normal SETC conditions, it can produce a maximum change of 14%. Based on the error analysis, it is believed that variations in α do not generate a significant effect on B.

CHAPTER VI

FINDINGS AND CONCLUSIONS

This research investigated pure metal electrodes, metal/sodium titanate, and metal/β''-alumina mixed conductor electrodes for AMTEC operation, measured their performance, proposed kinetic mechanisms for electrode processes and calculated optimum composition characteristics. The findings and conclusions are listed below:

i. Using thermodynamic theory, chemical potential diagrams were created for the Na-Al-O, Na-Ti-O, and Na-Al-Ti-O systems at 1100K. Those diagrams illustrate that β''-alumina is stable over limited range of AMTEC operating conditoins. Ni and $Na_2Ti_3O_7$ are thermodynamically stable at AMTEC operating conditions and also compatible with BASE.

ii. Based on the chemical and physical properties, metal Ta, Ni, Nb, Ir, W and MoRe were studies as the electronic component-cadidates for MIEEs and tested in SETCs. The experimental results showed that metal Ni is the best choice to be the electronic conductor in a MIEE.

iii. Based on the percolation theory, a theoretical model was constructed. It interpreted the performance differences of mixed conductor electrodes and predicted the optimum particle size and composition range. The reaction area was evaluated for electrodes with different compositions and particle sizes. The model shows that the reaction area decreases with increasing particle size and particle size ratio. It also predicts the electrode with two components has the best performance when these two

components have the same volume fraction and same particle size, and this particle size should be as small as possible.

iv. For a mixture of $Na_2Ti_3O_7$ and $Na_2Ti_6O_{13}$ with mass ratio of 1/2, the average activation energy for the bulk conductivity is 0.87ev. At AMTEC working temperatures (~1120K), the conductivity of the grain boundaries is much higher than that of the bulk.

v. The pure metal electrodes and mixed conductor electrodes had similar impedance spectra, which consist of two depressed semicircles. The semicircle at high frequency is related to sodium charge transfer reaction, while the semicircle at low frequency is related to sodium vapor transport through the electrode. The theoretical expression for the impedance of the electrode processes has been derived.

vi. The pure metal electrodes and mixed conductor electrodes have similar electrode kinetics mechanisms. The transport resistance is determined by not only electrode transport characteristics but also charge transfer properties. For most of the tested electrodes, the rate constant of sodium transport is smaller than that for sodium oxidation reaction and can be calculated from the impedance spectra, which is equal to the frequency of the maximum point on the semicircle at low frequency range. For a pure metal electrode, the sodium vapor pressure at the electrode/electrolyte interface could be estimated by measuring electrode impedance and extracting the diffusion capacitance.

vii. Sodium transport in the electrode is controlled by single activation energy of 99.4kJ/mol for a Ni electrode, although it might include several steps.

viii.   All tested metal/β″-alumina electrodes had similar and low performance. The flame spraying deposition technique worked for the fabrication of mixed conductor electrodes with multiple components.

ix.   Ni/sodium titanate with the Ni/sodium titanate ratios of 4/1 displayed the best performance and longest lifetime among all tested MIEEs, the pure metal electrodes and standard TiN electrode. Ni particles are able to form a network microstructure that is close to the theoretical morphology of the ideal electrode.

x.   Grain agglomeration occurred in SETC testing for all electrodes, and sodium titanate particles limited the growth of metal grains in mixed conductor electrode. The performance of the mixed conductor electrode is strongly dependent on microstructure.

xi.   Variations in transfer coefficient α do not generate a significant effect on B. At traditional SETC conditions, variations of α causes 6% change in B, for the normal SETC conditions, it produces a maximum change of 14%.

REFERENCES

1. R. K. Sievers, J. F. III Ivanenok, and T. K. Hunt, *Mechanical Engineering Magazine*, **117**(10), 70, (1995).

2. R. K. Sievers, R. J. Rasmussen, and C. J. Giglio, in *Proceedings of the 33rd Intersociety Energy Conversion Engineering Conference*, 359, Colorado Springs, CO, (1998).

3. C. P. Bankston, T. Cole, S. K. Khanna, and A. P. Thakoor, in *Proceedings of the 1st Symposium on Space Nuclear Power Systems*, 393, Albuquerque, NM, (1984).

4. J. W. Suitor, M. Shirbacheh, R. M. Williams, and C. P. Bankston, *AMTEC Technology Development Plan,* Jet Propulsion Laboratory, Pasadena, CA, (1990).

5. R. D. Cockfield, and E. W. Tobery, in *Proceedings of the Space Technology and Applications International Forum*, 1482, Albuquerque, NM (2000).

6. J. Tournier and M. S. El-Genk, in *Proceedings of the 33rd Intersociety Energy Conversion Engineering Conference*, 057, Colorado Springs, CO, (1998).

7. C. S. Mayberrt, J. Merrill, D. Radzykewycz, and K. Reinhardt, *Renewable Energy*, **23**, 451, (2001).

8. K. Hyder, R. L. Wiley, G. Halpert, D.J. Flood, and S. Sabripour, *Spacecraft Power Technologies*, Imperial College Press, London (2000).

9. N. Weber, *Energy Conv.*, **14**, 1, (1974).

10. T. Cole, *Science*, **221**, 915, (1983).

11. C. P. Bankston, T. Cole, R. Jones, and R. Ewell, *J. Energy*, **7**, 442, (1983).

12. C. B. Vining, R. M. Williams, M. L. Underwood, M. A. Ray, and J. W. Suitor, *J. Electrochem. Soc.*, **140**, 2760, (1993).

13. J. M. Tournier and M. S. El-Genk, *Energy Conversion & Management*, **40**, 139, (1999).

14. J. M. Tournier and M. S. El-Genk, in *Proceedings of the Space Technology and Applications International Forum*, 1552, New York (1998).

15. *Solid Electrolytes*, S. Geller, Editor, Springer-Verlag Press, Berlin, Germany (1977).

16. T. Cole, N. Weber, and T. K. Hunt, in *Fast Ion Transport in Solids*, *Electrodes and Electrolytes*, P. Vashishta, J. N. Mundy, and G. K. Shenoy, Editors, p277, Elsevier North Holland, Amsterdam (1979).

17. J. T. Kummer, in *Progress in Solid State Chemistry*, H. Reiss and J. O. McCaldin, Editors, **7**, p141, Pergamon Press Inc., New York, (1972).

18. T. Kudo and K.Fueki, *Solid State Ionics,* Kodansha, Tokyo (1990).

19. J. L. Sudworth, and A. R. Tilley, *The Sodium Sulfur Battery*, Chapman and Hall, New York (1985).

20. C. Subbarao, *Solid Electrolytes and Their Applications*, Plenum Press, New York, (1980).

21. T. Hattori and M. Ishigame, *Solid State Ionics*, **109**, 197, (1998).

22. J. P. Boilot, A. Kahn, J. Thery, R. Collongues, J. Antoine, D. Vivien, C. Chevrette and D. Gourier, *Electrochimica Acta*, **22**, 741, (1977).

23. J. D. Hodge, *J. Am. Ceram. Soc.,* **66**(3), 166, (1983).

24. G. Yamaguchi, and K. Suzuki, *Bull. Chem. Soc, Japan*, **41**, 93, (1968).

25. J. T. Kummer, and N. Weber, *U.S. Patent 3413150*, (1968).

26. R. M. Willams, M. A. Ryan, M. L. Homer, L. Lara, K. Manatt, V. Shields, R. H. Cortez, and J. Kulleck, in *Proceedings of the 33rd Intersociety Energy Conversion Engineering Conference*, 333, Colorado Springs, CO (1998).

27. M. A. K. Lodhi, P. Vijayaraghavan and A. Dalogu, *Journal of Power Sources,* **93**, 41, (2001).

28. R. M. Willams, M. L. Homer, J. Kulleck, L. Lara, A. K. Kisor, R. H. Cortez, V. B. Shields, and M. A. Ryan, in *Proceedings of the Space Technology and Applications International Forum*, 1408, Albuquerque, NM (2000).

29. M. A. K. Lodhi and A. Dalogu, *Journal of Power Sources*, **85**, 203, (2000).

30. M. A. K. Lodhi and A. Dalogu, *Journal of Power Sources*, **91**, 99, (2000).

31. P. E. Hausgen and J. G. Hartley, in *Proceedings of the 36th Intersociety Energy Conversion Engineering Conference*, 513, Savannah, GA (2001).

32. M. A. Ryan, V. B. Shields, R. H. Cortez, L. Lara, M. L. Homer, and R. M. Williams, in *Proceedings of the Space Technology and Applications International Forum*, 1377, Albuquerque, NM (2000).

33. M. A, Ryan, A. Kisor, R. M. Williams, B. Jeffries-Nakamura, and D. O′Connor, in *Proceedings of the 29th Intersociety Energy Conversion Engineering Conference*, **2**, 877, Monterey, CA (1994).

34. V. B. Shields, M. A. Ryan, R. M. Williams, and M. L. Homer, in *Proceedings of the 34th Intersociety Energy Conversion Engineering Conference*, 1999-01-2703, Vancouver, British Columbia (1999).

35. M. A. Ryan, V. B. Shields, R. H. Cortez, L. Lara, M. L. Homer, and R. M. Williams, in *Proceedings of the 34th Intersociety Energy Conversion Engineering Conference*, 1999-01-2704, Vancouver, British Columbia (1999).

36. R. M. Williams, B. Jeffries-Nakamura, M. L. Underwood, C. P. Bankston, H. LeDuc, and J. T. Kummer, *J. Electrochem. Soc.*, **137**, 1716, (1990).

37. M. A, Ryan, B. Jeffries-Nakamura, R. M. Williams, M. L. Underwood, D. O′Connor and S. Kittert, *J. Electrochem. Soc.*, **142**, 4252, (1995).

38. R. M. Williams, B. L. Wheeler, B. Jeffries-Nakamura, M. E. Loveland, C. P. Bankston, and T. Cole, *J. Electrochem. Soc.*, **135**, 2736, (1988).

39. B. Firbig, M. Schuller, M. A, Ryan, R. M. Williams, and P. Hudson, in *Proceedings of the Space Technology and Applications International Forum*, 99-105, Woodbury, NY (1999).

40. *Space Nuclear Power System, Orbit Book,* C. P. Bankston, M. S. El-Genk, and M. D. Hoover, Editors, Ch18., Malabar, FL (1987).

41. M. A, Ryan, B. Jeffries-Nakamura, R. M. Williams, M. L. Underwood, D. O'Connor and S. Kikkert, in *Proceedings of the 27th Intersociety Energy Conversion Engineering Conference*, **3**, 3.7, San Diego, CA (1992).

42. B. L. Wheeler, R. M. Williams, B. Jeffries-Nakamura, J. L. Lamb, M. E. Loveland, C. P. Bankston, and T. Cole, *J. Appl. Electrochem.*, **18**, 410, (1988).

43. R. M. Williams, B. Jeffries-Nakamura, M. L. Underwood, B. L. Wheeler, M. E. Loveland, S. J. Kikkert, J. L. Lamb, T. Cole, J. T. Kummer, and C. P. Bankston, *J. Electrochem. Soc.*, **136**(3), 893, (1989).

44. R. M. Williams, G. Nagasugramanian, S. K. Kahanna, C. P. Bankston, A. P. Thakoor, and T. Cole, *J. Electrochem. Soc.*, **133**, 1587, (1986).

45. J. R. Mcbride, R. F. Novak, D. J. Schnatz, W. B. Copple, J. T. Brockway, N. Arnon and G. A. Grab, in *Proceedings of the 24th Intersociety Energy Conversion Engineering Conference*, 683, Washington, DC (1989).

46. O. Asakami, K. Tsuchida, T. Togawa, and A. Kato, *J. Mater. Sci. Lett.*, **8**, 1141, (1989).

47. O. Asakami, K. Tsuchida, and A. Kato, *J. Mater. Sci. Lett.*, **9**, 892, (1990).

48. H. Nakata, T. Nagata, K. Tsuchida, and A. Kato, *J. Appl. Electrochem.*, **23**, 1251, (1993).

49. K. Tsuchida, T. Nagata, and A. Kato, *J. Mater. Sci.*, **33**, 755, (1998).

50. T. K. Hunt, *Research on Materials Related to the Sodium Heat Engine: Final Report*, LBL-21232, Lawrence Berkeley National Laboratory, Berkeley, CA (1986).

51. H. Izawa, S. Kikkawa, and M. Kolzuml, *J. Phys. Chem.*, **86**, 5023, (1982).

52. S. Anderson, and A. D. Wadsley, *Acta Crystallogr.*, **14**, 1245, (1961).

53. R. D. Adams, R. Layland, M. Danot and C. Payen, *Polyhedron*, **15**, 2567, (1996).

54. J. P. Shim, J. S. Lee, H. K. Kee, and S.G. Park, *Synthetic Metals*, **71**, 2261, (1995).

55. J. Majer, M. Holzinger, and W. Sitte, *Solid State Ionics*, **74**, 5, (1994).

56. J. Ramirez, and P. Fabry, *Sensors and Actuators B*, **77**, 339, (2001).

57. S. Kikkawa, F. Yasuda, and M. Koizumi, *Mater.Res. Bull.*, **20**,1221, (1985).

58. S. Pal, S. D. Pandey, and P. Chand, *Solid State Communications*, **69**(12), 1203, (1989).

59. K. Byrappa, B. S. Ravi Raj, W. Rajeev, A B Kulkarni, R.R. Clemente, and S. Gali, *Indian J. Phys.*, **71**A(2), 131, (1997).

60. M. A. Ryan, R. M. Williams, L. Lara, R. H. Cortez, M. L. Homer, V. Shields, J. Miller, and K. S. Manatt, in *Proceedings of the 33rd Intersociety Energy Conversion Engineering Conference*, 335, Colorado Springs, CO (1998).

61. B. Rodgers, www.consultrsr.com/resources/eis, [Accessed August 2006].

62. Gamry Instruments, www.gamry.com/App_Notes/Index.htm, [Accessed August 2006].

63. *Impedance Spectroscopy: Theory, Experiment, and Applications*, 2nd ed., E. Barsoukov and J. R. Macdonald, Editors, John Wiley & Sons Inc., Hoboken, NJ (2005).

64. *Physical Electrochemistry Principles, Methods and Applications,* I. Rubinistein, Editor, Marcel Dekker. Inc. New York (1995).

65. *Modern Aspects of Electrochemistry,* J.O'M. Bockris, B.E. Conway, and E. R. White, Editors, **32**, Kluwer Academic, New York (1999).

66. C. W. Wang, A. Rakotondrainibe, J. A. Appleby, and F. E. Little, *J. Electrochem. Soc.,* **147**(12), 4432, (2000).

67. S. J. Reed, *Electron Microprobe Analysis*, 2nd ed., Cambridge Press, New York (1993).

68. M. Ohring, *The Materials Science of Thin Films*, Academic Press, San Diego, CA (1992).

69. *Handbook of Deposition Technology for Films and Coatings: Science, Technology and Applications*, 2nd ed., R. F. Bunshah, Editor, Noyes Publications, Park Ridge, NJ (1994).

70. D. M. Mattox, *Handbook of Physical Vapor Deposition (PVD) Processing*, Noyes Publications, Park Ridge, NJ (1998).

71. Scienc Projects, www.science-projects.com/Coulter/Coulter.htm, [Accessed August 2006].

72. Beckman Coulter Inc., www.beckman.com/products/pr1.asp, [Accessed August 2006].

73. GMI Inc, www.gmi-inc.com/CliniLab/Coulter%20Multisizer%203%20Counter.html, [Accessed August 2006].

74. J. Nuyttens, http://openchemist.net/chemistry/coulter, (2004).

75. A. Lobeiras and J. Sabau, in *6th World Congress of Chemical Engineering* www.beckman.com/literature/Bioresearch/ta-104.pdf, Melbourne, Australia (2001).

76. *Smithells Metal Reference Book*, 7th ed., E. A., Brandes and G. B. Brook, Editors, Butterworth-Heinemann, Oxford (1997).

77. Wikipedia, en.wikipedia.org/wiki/Vapor_pressures_of_the_elements_(data_page), [Accessed August 2006].

78. G. Neumann, and G. M. Neumann, *Surface Self Diffusion of Metals*, Diffusion Information Center, Bay Village, OH (1972).

79. N. S. Choudhury, *J Electrochem. Soc.,* **133**, 425, (1986).

80. M. Itoh, K. Kimura and Z. Kozuka, *Trans. JIM*, **26**, 353, (1985).

81. G. M. Kale, *Metall. Trans. B,* **23B**, 833, (1992).

82. M. Barsoum, *J. Mater. Sci.,* **25**, 4393, (1990).

83. R. M. Williams, C. P. Bankston, S. K. Khanna and T. Cole, *J Electrochem. Soc.,* **133**, 2253, (1986)

84. G. Erisson, and A. D. Pelton, *Metall. Trans.*, **24B**, 795, (1993).

85. H. Yokokawa, T. Horita, N. Sakai T. Kawada, and M. Dokiya, *Solid State Ionics,* **78**, 203, (1995).

86. *Impedance Spectroscopy: Emphasizing Solid Materials and Systems,* J. R. Macdonald, Editor, John Wiley & Sons Inc., New York (1987).

87. R. M. Williams, M. E. Loveland, B. Jeffries-Nakamura, M. L. Underwood, C. P. Bankston, H. LeDuc, and J. T. Kummer, *J. Electrochem. Soc.*, **137**, 1709, (1990).

88. D. Stauffer and A. Aharony, *Introduction to Percolation Theory,* 2nd ed., CRC Press. LLC, Boca Raton, FL (1994).

89. G. Grimmett, *Percolation,* 2nd ed., Springer-Verlag Press, Berlin, Germany (1999).

90. P. Costamagna, M. Panizza, G. Cerisola, and A. Barbucci, *Electrochimica Acta*, **47**, 1079, (2002).

91. S. Sunde, *J. Elecrochem. Soc.,* **143**(3), 1123, (1996).

92. P. Costamagna, P. Costa and E. Arato, *Electrochimica Acta*, **43**, 967, (1998).

93. D. He and N. N. Ekere. *J. Phys. D: Appl. Phys.,* **37**, 1848, (2004).

94. D. Bouvard and F. F. Lange, *Acta Metall.Mater.,* **39**(12), 3083, (1991).

95. C. H. Kuo and P. K. Gupta, *Acta Metall.Mater*, **43**(1), 397, (1995).

96. M. Suzuki and T. Oshima, *Powder Technology*, **35**, 159, (1983).

97. C.S. Hsu and F. Mansfeld, *Corrosion*, **57,** 747, (2001).

98. P. Pasierb, S. Komornicki, R. Gajerski, and S. Kozinski, *J. Electroceram.*, **8**, 57, (2002).

99. J. R. Salgado, E. Djurado, and P. Fabry, *J. Eur. Ceram. Soc,* **24**, 2477, (2004).

100. G. H. Li, and J. M. Hong, *Mat. Res. Bull.* **34**, 2341, (1999).

101. C. E. Bamberger, G.M. Begun, *J. Am. Ceram. Soc.* **70,** C-48–C-51, (1987).

102. A-L. Sauvet, S. Baliteau, C. Lopez and P. Fabry, *J. Solid State Chemistry*, **177**, 4508, (2004).

103. C. H. Chen and K. Amine, *Solid State Ionics*, **144**, 51, (2001).

104. C-H. Kim, S-I. Pyun, and J-H. Kim, *Electrochimica Acta*, **48**(23), 3455, (2003).

105. W. H. Mulder, J. H. Sluyters, T. Pajkossy and I. Nyikos, *J. Electroanal. Chem.*, **285**, 103, (1990).

106. C. A. Schiller and W. Strunz, *Electrochimica Acta*, **46**(24-25), 3619, (2001).

107. A. J. Bard, and L. R. Faulkner, *Electrochemical Methods: Fundamentals and Applications*, 2nd ed., John Wiley & Sons Inc., New York (2001).

108. *NIST*, webbook.nist.gov/chemistry, [Accessed August 2006].

109. *NIST-JANAF Thermochemical Tables*, M. W. Jr. Chase, Editor, American Chemical Society, Woodbury, NY (1998).

110. R. D. Holmes, H. C. O'Neill, and R. J. Arculus, *Geochimica et Cosmochimica Acta*, **50**, 2439, (1986).

APPENDIX A

CALCULATION OF GIBBS FREE ENERGY

Table A.1. Thermodynamic properties of compound in the Na-Al-Ti-O system

Chemical Formular	$\Delta_f H^o$ (298.15) kJ/mole	S^o (298.15) J/mole/K	Heat Capacity $Cp=a+(b\times10^{-3})T+(c\times10^5)T^{-2}+d/T^{1/2}+(e\times10^8)T^{-3}$					$\Delta_f G^o$ (1100) kJ/mole	Ref
			a	b	c	d	e		
O_2		205.1	29.659	6.137	-2.196			0	108
Na(s) (298-370K)		51.46	72.637	-9.492	-12.594				108
Na(l) (370-1170.5K)			40.257	-28.238	-0.799				108
Na(g)	107.3	153.67						5.865	108
β-Ti(s)		30.72	23.057	5.541	-0.561				108
Al (298-933K)	0	28.27	28.089	5.415	-2.774			0	108
Al (933-2790.8K)			31.751	3.936×10^{-8}	5.480×10^{-8}				108
Na_2O	-417.98	75.04						-267.206	109
TiO_2(rutile)	-944.747	50.29						-744.803	109

Continued on next page

Chemical Formular	$\Delta_f H^o$ (298.15) kJ/mole	S^o (298.15) J/mole/K	Heat Capacity $Cp=a+(b\times10^{-3})T+(c\times10^5)T^{-2}+d/T^{1/2}+(e\times10^8)T^{-3}$ a	b	c	d	e	$\Delta_f G^o$ (1100) kJ/mole	Ref
γ-Al$_2$O$_3$(s)	-1656.9	52.3						-1313.99	109
NiO(s)								-140.6	110
Cu$_2$O(s)	-170.71	92.36						-88.331	109
CuO(s)	-156.06	42.59						-58.542	109
Na$_2$TiO$_3$(s)	-1586.8	123.5	198.9		-59.49	-644.3	8.505	-1223.7	84
Na$_2$Ti$_2$O$_5$(s)	-2539.7	173.6	272.6			-1282.7	-1.576	-1983.8	84
Na$_2$Ti$_3$O$_7$(s)	-3490.5	233.9	367.2			-1940.3	-1.371	-2748.2	84
Na$_2$Ti$_6$O$_{13}$(s)	-6322.9	398.6	483.0	55.45	-90.96			-4991.0	84
NaAlO$_2$(s)	-1133.19	70.4						-890.6	80
NaAl$_5$O$_8$(s)	-4523.73	148.56	351.9	24.65	-191.84			-3542.4	80
Na$_2$Al$_{22}$O$_{34}$(s)	-19145.5	583.14	1451.1	90.69	-826.34			-15029.4	82

Calculation of Gibbs Free Energy of Formation at 1100K.

According to the thermodynamic theory, the standard Gibbs free energy of compound formation is defined as

$$\Delta G_f^o(T) = \Delta H_f^o(T) + T\left[S^o(T)_{compound} - \sum coeff \times S^o(T)_{elements}\right] \tag{A.1}$$

where, $\Delta H_f^o(T)$ is the standard enthalpy of formation, and defined as

$$\Delta H_f^o(T) = \Delta H_f^o(298.15) + \left[H^o(T) - H^o(298.15)\right]_{compound}$$
$$- \sum coeff \times \left[H^o(T) - H^o(298.15)\right]_{elements} \tag{A.2}$$

$S^o(T)$ is the standard entropy and defined as

$$S^o(T) = S_{298}^o + \int_{298}^T \frac{C_p}{T} dT \tag{A.3}$$

For example, we use above three equations to calculate the standard Gibbs free energy of formation of $NaAl_5O_8$ compound, all data listed in Table A.1.

$$Na(l) + 5Al(l) + 4O_2(g) \rightarrow NaAl_5O_8(s)$$
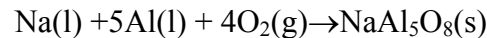
$$\Delta H_f^o(1100)_{NaAl_5O_8} = \Delta H_f^o(298.15)_{NaAl_5O_8} + \left[H^o(1100) - H^o(298.15)\right]_{NaAl_5O_8}$$
$$- \left[H^o(1100) - H^o(298.15)\right]_{Na} - 5\left[H^o(1100) - H^o(298.15)\right]_{Al}$$
$$- 4\left[H^o(1100) - H^o(298.15)\right]_{O_2}$$

$$\Delta H_f^o(1100)_{NaAl_5O_8} = \Delta H_f^o(298.15) + \int_{298.15}^{1100} C_p(T)dT_{NaAl_5O_8} - \int_{298.15}^{1100} C_p(T)_{Na} dT$$

$$- 5\int_{298.15}^{1100} C_p(T)_{Al} dT - 4\int_{298.15}^{1100} C_p(T)_{O_2} dT$$

$$= -4523730 + \int_{298.15}^{1100} C_p(T)dT_{NaAl_5O_8} - \int_{298.15}^{1100} C_p(T)_{Na} dT$$

$$- 5\int_{298.15}^{1100} C_p(T)_{Al} dT - 4\int_{298.15}^{1100} C_p(T)_{O_2} dT$$

$$= -4523730 + \int_{298.15}^{1100} \left(351.9 + 0.02465T - \frac{1.9174 \times 10^7 T^{-2}}{T} \right)_{NaAl_5O_8} dT$$

$$- 26335 - 5 \times 33981 - 4 \times 26$$

$$= -4575.62 \text{kJ/mol}$$

$$S^o(1100)_{NaAl_5O_8} = S^o(298.15)_{NaAl_5O_8} + \int_{298.15}^{1100} \frac{C_p(T)}{T} dT_{NaAl_5O_8}$$

$$= 148.56 + \int_{298.15}^{1100} \frac{(351.9 + 0.02465T - 1.9174 \times 10^7 T^{-2})}{T} dT_{NaAl_5O_8}$$

$$= 527.8 J/mole/K$$

$\Delta G_f^o(1100)_{NaAl_5O_8}$

$$= \Delta H_f^o(1100)_{NaAl_5O_8} + 1100 \times \left[S^o(T)_{NaAl_5O_8} - S^o(1100)_{Na} - 5S^o(1100)_{Al} - 4S^o(1100)_{O_2} \right]$$

$$= -4575.62 kJ/mole - 1100 \times (527.8 - 97.377 - 5*76.426 - 4*246.9) \times 10^{-3} kJ/mole$$

$$= -3542.4 kJ/mol$$

For some compounds, their thermodynamic data are not available. For example,

$$Na_2O(s) + Al_2O_3(s) + 6TiO_2(s) \rightarrow Na_2Al_2Ti_6O_{16}(s)$$

Assuming $Na_2Al_2Ti_6O_{16}$ could begin to form at 1100K, so

$$\Delta G_{rxn}(1100) = 0$$

$$\Delta G_{rxn}(1100) = \Delta G_{f,Na_2Al_2Ti_6O_{16}}^o - \Delta G_{f,Na_2O}^o - \Delta G_{f,Al_2O_3}^o - 6 \times \Delta G_{f,TiO_2}^o = 0$$

$$\Delta G_{f,Na_2Al_2Ti_6O_{16}}^o = \Delta G_{f,Na_2O}^o + \Delta G_{f,Al_2O_3}^o + 6 \times \Delta G_{f,TiO_2}^o$$

$$\Delta G_{f,Na\,Al_2Ti_6O_{16}}^o = -267.206 - 1313.99 + 6 \times (-744.803)$$

$$= -6050.01 kJ/mole$$

(A.4)

In fact, $Na_2Al_2Ti_6O_{16}$ formation requires a higher temperature, thus $\Delta G_{f,Na_2Al_2Ti_6O_{16}}$

calculated in equation (A.4) is the minimum Gibbs formation free energy of

$Na_2Al_2Ti_6O_{16}$.

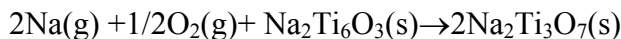**Calculation of Gibbs Free Energy of Reaction at 1100K.**

$$\Delta G_{rxn}^{o} = \sum coeff_p \times \Delta G_f^{o}(products) - \sum coeff_r \times \Delta G_f^{o}(reac\tan ts) \qquad \text{(A.5)}$$

$$\Delta G_{rxn} = \Delta G_{rxn}^{o} + RT \ln Q \qquad \text{(A.6)}$$

Where Q is the reaction quotient.

For example,

$$2Na(g) + 1/2O_2(g) + Na_2Ti_6O_3(s) \rightarrow 2Na_2Ti_3O_7(s)$$

$$\Delta G_{rxn}^{o} = 2 \times \Delta_f G_{Na_2Ti_3O_7}^{o}(1100) - \Delta_f G_{Na_2Ti_6O_{13}}^{o}(1100) - 2 \times \Delta_f G_{Na(g)}^{o}(1100)$$

$$= 2 \times (-2748.2) - (-4991.0) - 2 \times 5.865$$

$$= -537.13 kJ$$

$$\Delta G_{rxn} = \Delta G_{rxn}^{o} + RT \ln Q$$

$$= -537.13 kJ + 8.314 \times 1100 \times 10^{-3} \times \ln[\frac{1}{P_{O_2}^{1/2} P_{Na}^{2}}] kJ \qquad \text{(A.7)}$$

$$= -537.13 kJ - 8.314 \times 1100 \times 10^{-3} \times [\frac{1}{2} \ln P_{O_2} + 2 \ln P_{Na}] kJ$$

When this reaction is at equilibrium, $\Delta G_{rxn} = 0$. So above equation (A.7) becomes to

$$0 = -537.13 - 8.314 \times 1100 \times 10^{-3} \times [\frac{1}{2} \ln P_{O_2} + 2 \ln P_{Na}]$$

and then

$$\log P_{O_2} = -51.0 - 4\log P_{Na}$$

This equation shows the relationship between the oxygen partial pressure and sodium partial pressure at equilibrium. We calculated equilibrium oxygen partial pressure for reactions in the Na-Al-O, Na-Ti-O, and selected metal systems and listed the results in Table 3.2, 3.3 and 3.4 respectively.

When chemical potential diagrams of the Na-Al-O and Na-Ti-O systems are superimposed, the stability region of $NaAlO_2$ and Na_2TiO_3 are overlapped. The possible reaction between them is listed below

$$2NaAlO_2(s) + 6Na_2TiO_3(s) \rightarrow Na_2Al_2Ti_6O_{16}(s) + 12Na(g) + 3O_2(g)$$
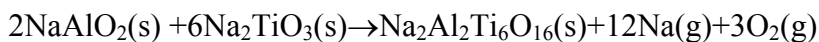
$$\Delta G_{rxn} = \Delta G_{rxn}^o + RT\ln Q$$

$$\Delta G_{rxn} = \Delta G_{rxn}(1100) = \Delta G_{f,Na_2Al_2Ti_6O_{16}}^o + 12\Delta G_{f,Na(g)}^o - 2\Delta G_{f,NaAlO_2}^o - 6\Delta G_{f,Na_2TiO_3}^o$$

$$+ RT\ln(P_{Na}^{12}P_{O_2}^3)$$

$$= 3145.51 + 8.314 \times 1100 \times 10^{-3}(12\ln P_{Na} + 3\ln P_{O_2})^{-3}$$

$$= 3145.51 + 8.314 \times 1100 \times 10^{-3} \times 3 \times 2.303(4\log P_{Na} + \log P_{O_2}) \qquad (A.8)$$

If $\Delta_{rxn}G(1100) < 0$, it means this reaction could spontaneously occur at the experimental conditions, otherwise, it can not. Therefore, we try to calculate the minimum $\Delta_{rxn}G$ in our experiment conditions. Observing equation (A.8), it is found that the minimum $\Delta_{rxn}G$ is obtained when sum of $4\log P_{Na} + \log P_{O_2}$ is minimum. For every value of P_{Na} and P_{O_2} in the overlapped region, the $\Delta_{rxn}G(1100)$ reaches the minimum, when the condition is on the equilibrium line between $NaAlO_2$ and $NaAl_5O_8$ (β''-alumina), the

right boundary of the overlap region. On this line, the pressure of oxygen and sodium obeys the following equation,

$$\log P_{O_2} = -44.34 - 4\log P_{Na} \qquad (A.9)$$

by substitution equation (A.9) into equation (A.8), we get $\Delta_{rxn}G(1100) = 343.86kJ > 0$, this is the minimum $\Delta_{rxn}G$ could be obtained at our experiment conditions and it is still greater than 0. Therefore, this reaction can not spontaneously occur in our experiment.

All the reactions listed in Table 3.4 were calculated and found that none of them would occur at our experiment conditions. So the compounds in this quaternary system are as stable as they are in tertiary systems.

APPENDIX B

Table B.1. Summary of Metal/β″-alumina Samples

SETC NO.	Components	Metal/β″-alumina mass ratio	Experiment durations
28	W/β″-alumina	3/1	9
30	W/β″-alumina	3/1	11
36	Ni/β″-alumina	3/1	10
37	Ni/β″-alumina	3/1	30
49	Cu/β″-alumina	1/1	11
52	Cu/β″-alumina	1/1	13
49	Ni/Cu/β″-alumina	3/3/2	11
50	Ni/Cu/β″-alumina	3/3/2	90
49	Co/Cu/β″-alumina	3/4/1	11
49	Co/Cu/β″-alumina	3/3/2	11
50	Co/Cu/β″-alumina	3/3/2	90
52	Co/Cu/β″-alumina	3/3/2	13

Table B.2. Summary of Metal/Sodium Titanate Samples

SETC NO.	Components	Metal/ Sodium Titanate mass ratio	Pass	Experiment durations
29	Cu/Sodium Titanate	1/1		20
49	Cu/Sodium Titanate	1/1	3	10
52	Cu/Sodium Titanate	1/1	4	15
49	Co/Cu/Sodium Titanate	3/3/2	3	10
51	Co/Cu/Sodium Titanate	3/3/2	4	15
52	Co/Cu/Sodium Titanate	3/3/2	5	15
49	Co/Cu/Sodium Titanate	3/4/1	3	10
50	Co/Cu/Sodium Titanate	3/4/1	3	90
49	Co/Cu/ Sodium Titanate	3/2/1	3	10
50	Co/Cu/Sodium Titanate	3/2/1	3	90
51	Co/Cu/Sodium Titanate	3/2/1	4	15
54	Ni/Cu/Sodium Titanate	3/3/2	4	30
55	Ni/Cu/Sodium Titanate	3/3/2	4	60
55	Ni/Cu/Sodium Titanate	3/3/3	3	60
55	Ni/Cu/ Sodium Titanate	3/3/3	4	60

Table B.3. Summary of Ni/Sodium Titanate Samples

SETC NO.	Name	Ni/Sodium Titanate mass ratio	Pass	Particle Size	Experiment durations
36	N4	4/1			5
37	N4	4/1			30
57	S3NT	4/1	3	3-7 μmNi	65
58	NT12	4/1	6	5-15μmNi	55
58	NT15	4/1	9	5-15μmNi	55
69	R55	4/1	3	July 23 mixture	12
69	R56	4/1	3	July 23 mixture	12
71	R65	4/1	3	2-3μmNi	18
71	R63	4/1	10	2-3μmNi	18
71	R69	4/1	10	3-7μmNi	18
72	R64	4/1	3	5-15μmNi	52
72	R68	4/1	3	3-7μmNi	52
72	R60	4/1	4	2-3μmNi	55
72	R66	4/1	10	2-3μmNi	55
73	R79	4/1	3	2-3μmNi	97
73	R74	4/1	5	July 23 mixture	97
73	R78	4/1	8	5-15μmNi	97
74	R76	4/1	2	2-3μmNi	97
74	R75A	4/1	8	July 23 mixture	97
74	R75B	4/1	10	July 23 mixture	97
75	R81	4/1	3	2-3μmNi	49
75	R83	4/1	3	2-3μmNi	49
75	R87	4/1	3	July 23 mixture	49
75	R84	4/1	5	2-3μmNi	49
76	R82	4/1	3	2-3μmNi	50
76	R88	4/1	3	July 23 mixture	50
76	R90	4/1	4	July 23 mixture	50

SETC NO.	Name	Ni/Sodium titanate Ratio(mass%)	Pass	Particle Size	Experiment durations
34	N3	3/1	2		60
36	N3	3/1			5
37	N3	3/1			30
39	N3	3/1	3		6
39	N4	3/1	4		6
58	L3NT	3/1	3	5–15umNi	3
58	L5NT	3/1	5	5–15umNi	5
31	N2	2/1			5
32	N4	2/1	4		12
32	N6	2/1	6		12
33	N	2/1			13
34	N22	2/1	2		45

July 23 mixture: 135g Ni (<1μm)+265g Ni(2-3μm)+100g sodium titanate (milled over 6 days).

VITA

Yuyan Guo was born in Taiyuan, ShanXi province of P.R. China on August 15, 1976. She received her B.S. in metallurgical engineering with honors in 1997 and an M.S. in materials science & engineering in 2000 from the University of Science & Technology, Beijing (Beijing, China). Her Ph.D. work was performed under the guidance of Dr. Michael Schuller and Dr. Timothy R. Hughbanks in the chemistry department at Texas A&M University (College Station, Texas, USA) and was completed in December of 2006. Her permanent address is the following:

Beijing Tongzhou District Xinhualian Jinyuan, #20 Building, Apt #151

Beijing, 101101

P. R. China.